Towards analog quantum simulation with superconducting 3D transmons

Thesis submitted to the

Faculty of Mathematics, Computer Science and Physics

of the Leopold-Franzens University of Innsbruck in partial

fulfillment for the

degree of Doctor of Philosophy

by

Oscar Gargiulo

Under the supervision of Univ-Prof. Dr. Gerhard Kirchmair,

Department of experimental Physics, Technikerstaße 21A,

Innsbruck-6020, Austria

March 3, 2021

Ai miei genitori, con amore.

Abstract

The aim of this project is the realization of a novel quantum simulator that can mimic a limited variety of quantum systems [1, 2, 3]. The limitation makes this quantum simulator (QSIM) less powerful and ambitious than a quantum computer and thus easier to realize. There are classes of problems that can be partially solved by classical computers [4, 5] and as a start we would like the QSIM to simulate one of these problems in order to compare results and benchmark the performance. In particular we will focus on simulation of a 1D spin chain [6, 7, 8] or 2D spin ladder [5, 9], referring particularly to the experimental realization proposed in ref. [5]. Our chosen platform for the QSIM realization is based on superconducting qubits [10], specifically 3D transmons [11, 12]. The motivation for this choice is mainly the requirement for qubit frequency and coupling uniformity [5]. 3D transmon are indeed isolated between each other and their coupling doesn't require interconnections, allowing to perform a pre-selection of the qubits used for the simulator. Another important aspect of the QSIM is the qubits state readout[1]. This can be done via coupling to a resonator with the possibility to interrupt this coupling "on command". A way to do it is to use frequency tunable qubits and decouple through frequency detuning. Such qubits can change their frequency in presence of a magnetic flux, however, the use of metal boxes such as cavities unfortunately brings up a problem: the injection of a magnetic flux inside them. Moreover, the qubit frequency must change on time scales that are shorter compared to the interaction strength between qubits and resonator and qubit lifetimes. Ideally The frequency change should occurr in less than hundreds nanoseconds for superconducting qubits based architectures.

Having internal flux lines is a problem since the qubit can strongly couple to them and decohere. External flux lines can be used, but this will face two problems. Firstly, for normal conducting materials, like copper, the injection will be slowed down by Eddy currents [13]. Then, for superconducting materials, like aluminium, the injection can be inhibited by the Meissner effect [14].

The main aim of this PhD thesis is specifically to address and solve this flux problem with a 3D cavity. The solution proposed is through the use of a magnetic hose, proposed in [15] and adapted to AC magnetic fields.

[1] under some conditions, to read the simulator state doesn't require to know the state of all the qubits at a given time.

ACKNOWLEDGEMENTS

First of all I want to thank Univ,-Prof. Gerhard Kirchmair for giving me the opportunity to do my PhD in his research group. It was a really good experience to build a working experimental setup from zero. I really what to thank him and Seyed Iman Mirzaie for everything they taught me. Then I want to thank Phani R. Muppalla for all the help and friendship he gave me and for all the good time spent together. Then I want to thank all the people that are or have been in the group, they made my life here really enjoyable, I really appreciated the time spent with everybody. I want to thank Cosimo for all the good discussions about physics... and food. Finally I want to thank my family and my girlfriend (soon my wife) for all the support and for all the good food!

Contents

Chapter 1

Introduction - Analog quantum simulator

1.1 Quantum simulation

The reason why science needs a quantum simulator is to overcome the limits of classical computation. The idea of building a well controllable system capable of mimicking other systems, was first proposed by Feynman [16]. In particular he emphasized the limitation of classical computation, where computational resources grow exponentially when we want to simulate quantum systems. So a quantum simulator is necessary to overcome those limitations. It will help in solving or understanding difficult problems in various fields like: condensed-matter physics (especially quantum phase transitions), quantum magnetism, high critical temperature superconductivity and also in high-energy physic and chemistry [1].

Quantum simulators are divided in two categories: analog and digital. A digital quantum simulator is characterised by having a set of quantum operations, so called "gates", used to control the system state and the interaction between its elements (qubits). Thanks to its programmable characteristic, a digital quantum simulator is, theoretically, universal [1]. An analog quantum simulator (AQS) is instead an engineered system where the Hamiltonian is identical to the one of the simulated system. Once the simulator is prepared in a given state, it will evolve with the same dynamics as the target and, in principle it is possible to extract information from the simulator at any given time. Analog quantum simulators are limited to a few systems (non universal) but, because of that, they are also less complicated to build.

1.2 System of interest part 1: spin systems

Materials differ from each others because of the nature of their elements and their interactions. Studying these interactions is hard and for this purpose simplified theoretical models are used. These models can capture the essential features of some material properties, like magnetism, while neglecting many of the complexities of the real material. This is one reason why spin models are used in condensed matter physics. Spin models are used to study physical phenomena like: magnetism, phase transitions, frustration and much more [17].

The goal of this thesis is to realize the fundamental building block of an analog quantum simulator with the aim of simulating spin systems with a few spins.

In quantum mechanics a spin operator is defined as:

$$\boldsymbol{S} = (S_x, S_y, S_z) = \frac{\hbar}{2}(\sigma_x, \sigma_y, \sigma_z) \tag{1.1}$$

with:

$$\sigma_x = \begin{pmatrix} 0 & 1 \\ 1 & 0 \end{pmatrix}; \sigma_y = \begin{pmatrix} 0 & -i \\ i & 0 \end{pmatrix}; \sigma_z = \begin{pmatrix} 1 & 0 \\ 0 & -1 \end{pmatrix} \tag{1.2}$$

known as Pauli matrices. And a spin-state, known as spinor, is represented as:

$$\Psi_{spin} = \begin{pmatrix} \alpha \\ \beta \end{pmatrix} = \alpha|\uparrow\rangle + \beta|\downarrow\rangle. \tag{1.3}$$

The exchange energy between two spins can be written as $2J\boldsymbol{S_1} \cdot \boldsymbol{S_2}$ [17][1] and, under the assumption that the exchange interaction applies to all neighbouring atoms, it can be extended for many-body systems, leading to:

$$H_{int} = 2\sum_{i>j}^{N} (J_{i,j}\boldsymbol{S}_i \cdot \boldsymbol{S}_j) \tag{1.4}$$

known as Heisenberg model Hamiltonian [17]. Here N is the total number of spins, and the $J_{i,j}$ terms are the interaction strengths between the i-th and j-th spin. The spins can also be constricted to point in one direction (usually the z-axis), in this case they are named Ising spins. Or they can be bound to a plane, in this case they are called XY spins.

Theoretical study of such spin-spin systems make use of simplifications,

[1] I am following the opposite sign convention of the quoted book and the same convention of refs. [18, 5]

among those there are two special cases worth to mention: the nearest-neighbour (NN) and the next nearest-neighbour (NNN). These models are valid when the interactions are mainly dipolar and so more local.

The NN model is usually used to describe a system of spins arranged on a line or a lattice. The Hamiltonian is a simplification of the one in equation 1.4 when one substitutes the J_{ij} term with J for $j = i + 1$ and 0 otherwise [19]. If J is negative, the interaction is ferromagnetic, otherwise anti-ferromagnetic.

If one now considers also the next near-neighbour interaction, then two values of J can be used: J_1 for $j = i+1$ and J_2 for $j = i+2$ (and 0 elsewhere). The NNN Hamiltonian can be written as [18]:

$$H_{NNN} = 2J_1 \sum_{i=1}^{N} \boldsymbol{S}_i \boldsymbol{S}_{i+1} + 2J_2 \sum_{i=1}^{N} \boldsymbol{S}_i \boldsymbol{S}_{i+2} \tag{1.5}$$

with the periodic assumption that $N + 1 = 1$. The interaction strengths play a fundamental role in the macroscopic behavior of the chain, for example, if J_1 and J_2 are both negative, the chain is characterized by a ferromagnetic order. So this model is particularly studied [18, 20, 21] as a function of the ratio J_2/J_1. A NNN spin chain shows a phase transition when the ratio J_2/J_1 is around 1/4 and 3/4. By increasing the ratio J_2/J_1, the system goes from a superfluid phase to a dimer phase, and finally to a chiral phase. The dimer phase is characterized by the formation of triplets, known as dimers.

Even though it is in theory possible to analytically solve a NNN chain model, more and more computational power is required because of the exponential scaling with the number of spins considered. In general, only ground states are evaluated by modern algorithms. Quantum simulators will overcome the computational power limit and allow scientists to solve these models or even more complicated ones. In a quantum simulator, indeed, the scaling is linear with the number of elements[2].

Some topics related to spin models, that are currently under studies and worth to mention, are: long-range interaction (far beyond the J_1-J_2 model), where the maximum speed with which information can propagate, affects how quickly parts of the system can correlate [22]. Entanglement and excitation propagation in the system, since the models used and the classical computation can only predict ground states, it is also something that needs to be investigated with a quantum simulation [6]. System frustration, the distribution of entanglement along the chain can create undetermined system order (with a degeneracy of the ground state, look at fig.1.1 for a simple example) that leads the system to behave in an "exotic" manner, like in the case of spin

[2]In reality more resources are needed for quantum error correction.

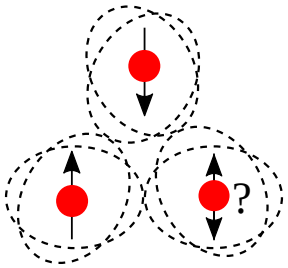

Figure 1.1: System frustration: Let's take, as example, three entangled spins like in the figure, where their interaction forces the spins to have opposing directions. Let's assume that we perform a projective measurement on the first two spins and we get their spin direction, the third one is in a situation where whatever is the outcome, it will be in contradiction with the minimal energy rule. For example, the possibilities are: $|\uparrow\downarrow\uparrow>$, where the first and the last spins are parallel or $|\uparrow\downarrow\downarrow>$, where the second and third are parallel. This kind of situation is called frustration, all the combinations are possible and have the same energy, leading to a degeneracy of the ground state. When the number of spins is high, the problem becomes really complicated to be classically simulated.

liquids [23]. More knowledge about frustration might also lead to a better understanding of high-Tc superconductivity [24].

1.3 System of interest part 2: simple scenario with an experimental proposal

From what has been said up to now, the AQS of this project should have a Hamiltonian that emulates the state and dynamics of a selected spin-system.

In this section, an experimental proposal about the realisation of an AQS with 3D transmons is presented. The proposal (ref. [5]) focuses specifically on 1D spin-chains [6, 7, 8] or 2D spin-ladders [5, 9]. One reason to limit to these system is to have the possibility to compare the simulator behavior with already known results obtained with classical computation. It is possible indeed to simulate such systems up to a certain degree with classical algorithms (DMRG algorithm [25]), so it will be possible to benchmark the simulator. The spin ladder and chain are depicted in fig.1.2, where the J_1 and J_2 interaction strengths have been emphasized, since the J_1-J_2 approximated model has been used in the reference [5].

In order to extract information about the system phase, in the paper a

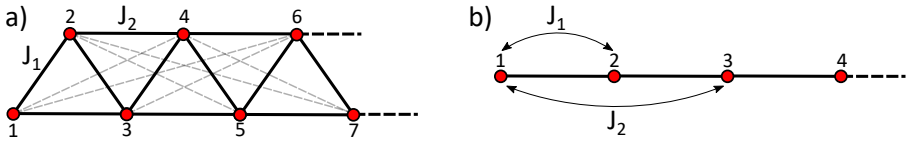

Figure 1.2: **(a)** Spin-ladder: The spins, represented as red dots, form a defined triangular structure. The interaction strengths are a function of the distances (lines). In the figure the strongest interaction strengths J_1 and J_2 are depicted with solid lines. Long distance interaction strengths (dotted lines) are ignored. The numbering has been chosen from left to right. **(b)** Spin-chain: when one allows NN or NNN then it is possible to map 2D triangular spin-ladders to an equivalent 1D spin-chain.

bond-order parameter (BOP) is introduced, particularly relevant in the dimer phase (DP)

$$D^{\alpha} = \left\langle \sum_{j=1}^{L-1} D_j^{\alpha} \right\rangle, D_j^{\alpha} = (-1)^j S_j^{\alpha} S_{j+1}^{\alpha}, \ \alpha = x, z \tag{1.6}$$

where L is the total number of spins. The D_j operator is the correlation between the spin operators S_j of a given spin in the chain and it's next neighbour. The BOP is the averaged sum of all the correlators D_j and it gives a measure of the spontaneous formation of triplets along the odd-even bonds. Moreover, in the center of the DP range, the phase can be ideally[3] identified in an even simpler way: by monitoring the bond correlation of a single pair of spins in the middle of the chain (j = L/2). For sake of simplicity, I will fix the projection axis to z

$$B^z = D^z_{L/2} \text{ (for } L = 4n, n \ \epsilon \ \mathbb{N}). \tag{1.7}$$

In Fig.1.3, a comparison between the behavior of the dimer correlation B^z against the BOP (black dashed line) as a function of the coupling ratio J_2/J_1 is shown for several values of L. One can see that measuring the BOP or B^z in the dimer phase for $J_2/J_1 > 0.5$ gives the same result and it is quite independent from L.

This concept is really important for the simulator we want to realize because it would be really hard to measure the BOP of the qubits since it will require to know the state of all of them in a given moment. With the possibility of measuring only the state of the central ones and a few more pairs, this difficulty is overcome and so we can have a way to test if the simulator is in a

[3]In reality more correlators are necessary because of experimental imperfections.

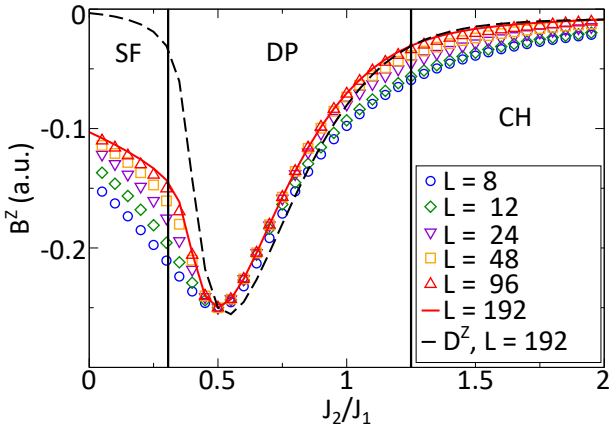

Figure 1.3: Bond order parameter: Comparison between the BOP D^z for L = 192 spins (dashed black line) and the bond correlation B^z in the middle of the chain for chains of different sizes. The regions for the three phases are also shown: superfluid (SF), dimer (DP), and chiral phase (CP). Figure taken from reference [5].

dimer phase.

Moreover in the paper [5] it is also shown that the the qubits and the coupling between them should be uniform. Avoiding a disorder larger then 35 % in the qubit frequency and interaction strength is possible thanks to a pre-selection of the qubits which will be discussed in the next section.

1.4 General idea and motivations for 3D SC architecture

The platform used for the realization of this AQS for spin-spin dipole systems is based on superconducting qubits [10], specifically 3D transmons [12]. Like a transmon realized on chip (2D) [11], it is characterized by a Josephson Junction shunted with a large capacitance (compared to the junction self-capacitance). However, the difference, that is also the main motivation for choosing the 3D transmons, is that they don't need any wiring, they are isolated and interact with each other through antennas. The isolation of each single transmon allows also to measure the normal state resistance[4] of the junction, that provides information on the qubit frequency. So we can fabricate chips with one or a few qubits and use the selected ones as building blocks for the AQS. Indeed, in the ideal system all the spins and interaction strengths are uniform, for example:

[4]The device will have a resistance at room temperature on the order of a few kΩ.

in the J_1-J_2 model for a spin ladder, $J_{i,i+1}$ is always equal to a constant value J_1; if our qubits are not identical we can't guarantee this property. To achieve the same uniformity in 2D architectures would be really hard, because if one qubit is broken or different, the whole chip must be fabricated again. It could be possible to fabricate 2D transmons on several chips and connect them with bonding wires. However, it will be challenging when the system is scaled up to achieve uniformity in the interaction strengths.

We will have two kind of 3D transmons in our system, single Josephson Junction based qubits (with a fixed frequency) and SQUID or asymmetric SQUID (aSQUID) based qubits where the frequency can be tuned by the use of an external magnetic field. The idea is to measure the frequency tunable qubits state, after interrupting the interaction with the other ones through frequency detuning. In this project the qubit state will be measured through a dispersive readout. For this reason, the aSQUID qubits must interact with a resonator. Such a resonator can be a cavity [3] or a stripline resonator in a waveguide [26].

The use of metal boxes such as cavities and waveguides, unfortunately brings up a problem in the 3D architecture that is not present in the 2D one: the injection of a magnetic flux through the SQUID loop, necessary to tune the qubit frequency. What we want to achieve is to tune the qubit frequency on a time scale that is comparable to typical qubit gates and faster than the interaction strength between qubits. The goal is to be faster than about one hundred nanoseconds. In the 2D structures this problem is solved by realizing so called flux bias lines on the same chip where the qubit is [27].

In 3D structures, it could be possible to have flux bias lines on-chip, but they would not be shielded by the ground plane. This is a problem since the qubit can strongly couple to the bias lines which leads to enhanced decoherence. External flux lines or coils can be used, but the injection of the magnetic field through the cavity wall will be slowed down by Eddy currents [13] if copper is used. The injection will even be inhibited by the Meissner effect [14] if a superconducting material like aluminium is used. The main aim of this PhD thesis is specifically to address and solve this flux problem with a 3D cavity. The solution proposed is through the use of a magnetic hose, proposed in ref. [15] and adapted to AC magnetic fields.

1.5 Thesis structure

In this chapter I have shown some models for spin systems, with their approximations and limitations. Also I introduced the analog quantum simulator we would like to realize using 3D transmons. In the next chapter the basic theory

of ideal qubits and artificial superconducting qubits is given. Models for superconducting circuits are introduced, together with the Josephson junction, which is the center of every SC qubit and the transmon qubit. Particularly relevant is the understanding of how superconducting devices couple to each other and how this coupling is useful for a qubit state readout. In the third chapter I describe the magnetic hose concept and design, central part of this PhD project and the solution used to guide magnetic flux in a metal box. All the basic concepts introduced are used together with classical simulators to design the experiment. In the fourth chapter I will explain what can be simulated and how to design the system elements and tune their parameters: cavity and qubit frequencies, qubit anharmonicity, coupling between qubit and cavity, hose field transfer, etc. Finally, in the fifth chapter, the experimental setup is explained, followed by the measurements I performed to characterize the qubit: decay and decoherence times, qubit temperature, flux noise, etc. The most important measurement is the characterization of the flux in the cavity, how much and how fast can we change the frequency of a qubit in a cavity thanks to a magnetic hose? Measurements of this so named flux jump will be the conclusion of this thesis.

Chapter 2

Theory

2.1 Basics

In this chapter I will introduce the building blocks of our AQS, based on 3D transmon qubits and 3D waveguide cavities. First the quantum bit, as an ideal two level system, is introduced. In the second part of the chapter I will go through the basics[28] of the circuit Quantum Electrodynamics (cQED) related to superconducting devices to have an understanding of the single elements and especially their interaction. Generally, superconducting linear circuits are built with elements like capacitances and inductances. Resistances are typically neglected because of the ideal non-dissipation characteristic of superconductors. However, another element is available in the superconducting circuits world: the Josephson Junction, that is a non-linear, dissipationless element based on quantum tunneling. This device is very important as it introduces a non-linearity in the system that provides the required anharmonicity between energy levels that allows us to address specific states of the circuit. Effectively this system will now behave like a two level system (TLS) and thus be close to the behavior of a spin.

2.1.1 Qubit as two level system

Like a classical bit, a qubit is characterized by two states: $|0\rangle$ and $|1\rangle$. A quantum two-level system has some probability to be found in one of its states and it is possible to control such probability, together with an additional phase. The qubit state can be represented as (note the similarity with the spinor 1.3):

$$\Psi_{qb} = \alpha|0\rangle + \beta|1\rangle = \alpha \begin{pmatrix} 1 \\ 0 \end{pmatrix} + \beta \begin{pmatrix} 0 \\ 1 \end{pmatrix}$$
$$|\alpha|^2 + |\beta|^2 = 1;\ \alpha, \beta \in \mathbb{C}. \tag{2.1}$$

In this case the probability to find the qubit in the $|0\rangle$ state is $|\alpha|^2$.

If we associate an energy E_0 to the state $|0\rangle$ and an energy E_1 to the state $|1\rangle$, it is quite straightforward to write a qubit Hamiltonian as:

$$H_q = \frac{E_1 + E_0}{2}\mathbb{1} - \frac{E_1 - E_0}{2}\hat{\sigma}_z \tag{2.2}$$

We can now define the qubit energy as $\hbar\omega_q = E_1 - E_0$ and ignore constants in the Hamiltonian to finally get:

$$H_q = -\frac{\hbar\omega_q}{2}\hat{\sigma}_z \tag{2.3}$$

It is, in general, more convenient to represent the qubit state on a sphere, by redefining the coefficients α and β such that the qubit state becomes:

$$\Psi_{qb} = \cos\left(\frac{\theta}{2}\right)|0\rangle + \sin\left(\frac{\theta}{2}\right)e^{i\varphi}|1\rangle \tag{2.4}$$

With $0 \leq \theta \leq \pi$ and $0 \leq \varphi < 2\pi$. In this way the state of the qubit can be represented as a vector on a sphere[1], named Bloch-sphere (Fig.2.1) and changing the qubit state means rotating the vector.

A qubit state can be rotated by applying a rotation operator $\hat{R}_k(\theta)$ that performs a rotation of an angle θ anti-clockwise around the axis k. A rotation operator can be written in terms of pauli matrixes:

$$\hat{R}_k(\theta) = \cos\left(\frac{\theta}{2}\right)\hat{\mathbb{1}} - i\ \sin\left(\frac{\theta}{2}\right)\hat{\sigma}_k \tag{2.5}$$

where k = x, y, z. A rotation around a general axis n with coordinates (θ_n, φ_n) in the Bloch sphere, can be decomposed in the application of several $\hat{R}_k(\theta)$ rotations. A rotation of an angle α around the axis n results in

$$\hat{R}_n(\alpha) = \hat{R}_z(\theta_n)\hat{R}_y(\varphi_n)\hat{R}_z(\alpha)\hat{R}_y(-\theta_n)\hat{R}_z(-\varphi_n). \tag{2.6}$$

In this way the first two rotations (two rightmost operators in the equation)

[1] One has to keep in mind, however, that the qubit state belongs to the SO(3) group and it cannot be represented exactly in a 3D sphere.

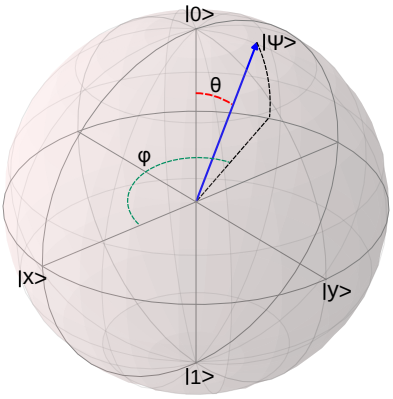

Figure 2.1: State vector in the Bloch-sphere: the qubit state is represented by the blue arrow, and is a function of the two angles (θ, φ). The vertical axis is represents the qubit polarization. The projections of the vector on the axis are the expectation values of the corresponding Pauli operators.

first rotates the vector such that it is coincident with the z-axis. Afterwards the desired α rotation is performed around the z-axis, now coincident with the n-axis. Finally the last two operators (leftmost in the equation) bring back the vector in the original position.

Given the qubit Hamiltonian 2.3, an easy way to implement a rotation around the z-axis would be to start from the state:

$$|\Psi_0\rangle = \frac{1}{\sqrt{2}}(|0\rangle + |1\rangle) \tag{2.7}$$

that corresponds to a vector on the Bloch sphere equator, and let it evolve over time. The time evolution of this Ψ_0 state corresponds to a rotation around the z-axis with a frequency equal to ω_q:

$$|\Psi(t)\rangle = e^{-i\frac{H_q}{\hbar}t}|\Psi_0\rangle = \frac{1}{\sqrt{2}}\begin{pmatrix} e^{i\frac{\omega_q}{2}t} \\ e^{-i\frac{\omega_q}{2}t} \end{pmatrix} \tag{2.8}$$

But what about rotations around the x and y-axis? We need to couple the qubit to an external drive. The total Hamiltonian will be the sum of equation 2.3 and an additional term that is proportional to the applied drive. In the qubit rotating frame, such an additional term can be written as:

$$\hat{H}_D = \Omega V_D(t)(\cos(\omega_q t)\hat{\sigma}_y - \sin(\omega_q t)\hat{\sigma}_x). \tag{2.9}$$

where Ω is a term that depends on the coupling strength between the drive

and the qubit and $V_D(t)$ is the applied signal.

An ideal signal can be considered as a waveform with frequency ω_D:

$$V_D(t) = V_0 s(t)\sin(\omega_D t+\phi) = V_0 s(t)[\cos(\phi)\sin(\omega_D t)+\sin(\phi)\cos(\omega_D t)] \quad (2.10)$$

where V_0 is the signal amplitude and s(t) represents a normalized envelope, like a step function, a gaussian function, etc. The $\cos(\phi)$ and $\sin(\phi)$ are respectively the so named in-phase (I) and quadrature (Q) components of the signal. By substituting 2.10 in 2.9, dropping fast rotating terms[2] and assuming that $\omega_q = \omega_D$, we finally get:

$$\hat{H}_D = -\frac{1}{2}\Omega V_0 s(t)(I\hat{\sigma}_x + Q\hat{\sigma}_y). \quad (2.11)$$

This equation shows that the in-phase component of the drive can perform rotations around the x-axis, and the quadrature component can perform rotations around the y-axis. Since only relative phases matters, the choice of I and Q is arbitrary as long as there is a 90 degrees phase between them. In the case where the drive frequency is not equal to the qubit frequency, however, a portion[3] of I also rotates the qubit around the y-axis and a portion of Q rotates the qubit around the x-axis. The rotation of a qubit state is described and shown in chapter 5.

2.1.2 Qubit decoherence

The state of an isolated qubit is stationary in the rotating frame. However, coupling the qubit to a thermal bath will lead to a change of its state due to noise. Since a qubit must be controlled, i.e. needs to be coupled to a drive, the coupling to a thermal bath is unavoidable.

The stochastic noise that affects a qubit is usually divided in two parts: longitudinal and transverse. Longitudinal noise can be seen as a qubit rotation around the z-axis, that corresponds to a change of the qubit phase and difficulty in qubit control, since the difference $\delta\omega$ between the frequency of the drive and the one of the qubit will change randomly over time. Transverse noise instead can be seen as a rotation around the other two axis, that affects the qubit polarization (the angle θ in the Bloch sphere 2.1.1).

Another mechanism that affects the qubit polarization is the qubit temperature. When the qubit is coupled to a thermal bath, it will start to decay exponentially with a decay rate Γ_1. The thermal decay rate is split in two parts: the cooling rate $\Gamma_{1\downarrow}$, that is the frequency of emission of a photon to

[2] In this case we can drop terms that oscillates with speed $\omega_q+\omega_D$ thanks to the rotating wave approximation.

[3] $I\cos(|\omega_D-\omega_q|t)$ rotates around the x-axis, and $-I\sin(|\omega_D-\omega_q|t)$ around the y-axis

the bath, and the heating rate $\Gamma_{1\uparrow}$, that is the frequency of absorption of a photon from the bath. These rates can be expressed as:

$$\begin{aligned} \Gamma_{1\uparrow} &= \gamma n_{th} \\ \Gamma_{1\downarrow} &= \gamma(n_{th}+1) \end{aligned} \tag{2.12}$$

where γ is a factor that is proportional to the coupling strength with the bath and the bath energy. The average thermal photon number n_{th} follows a Bose-Einstein statistic. Assuming the bath is however relatively cold, i.e. few mK, it is possible to use a Boltzmann statistic due to the low photons density. So we can express the heating rate as:

$$\Gamma_{1\uparrow} \approx \Gamma_{1\downarrow} \exp^{-\frac{\hbar\omega_q}{k_B T}} \tag{2.13}$$

For superconducting qubits we have $\hbar\omega_q \gg k_B T$ and the heating rate is close to zero. As a consequence, after waiting enough time, the qubit population will be found in the ground state. Ideally, the decay rate of a qubit from the excited state to the ground state is limited by the coupling with the bath, but in general additional transverse noise from the environment contributes to increase it.

For the dephasing rate instead, it is typical to divide it in two parts:

$$\Gamma_2 = \frac{\Gamma_1}{2} + \Gamma_\varphi \tag{2.14}$$

where the first term takes in account that, when the qubit decays to the ground state, the trasnversal orientation of the Bloch vector (the angle φ in the Bloch sphere 2.1.1) is lost. The second term instead is the effect of the total longitudinal noise.

For a qubit at T = 0 K it is possible to write the Bloch-Redfield density matrix [29]:

$$\rho_{BR} = \begin{pmatrix} 1+(|\alpha|^2-1)e^{-\Gamma_1 t} & \alpha\beta^* e^{i\delta\omega t} e^{-\Gamma_2 t} \\ \alpha^*\beta e^{-i\delta\omega t} e^{-\Gamma_2 t} & |\beta|^2 e^{-\Gamma_1 t} \end{pmatrix} \tag{2.15}$$

where the diagonal terms suggest that a qubit in the ground state keeps the state[4], but otherwise it will decay to the ground state after a time longer than $T_1 = \Gamma_1^{-1}$. The off-diagonal terms instead decay to a 0 value after a time longer than $T_2 = \Gamma_2^{-1}$. In chapter 5 I will show how to experimentally measure these two quantities.

[4]In reality transverse noise can still excite the qubit from the ground state.

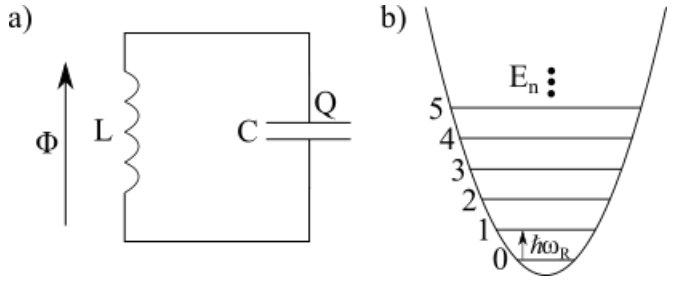

Figure 2.2: LC circuit as harmonic oscillator: a) circuit schematic of an LC circuit, with a charge Q stored on the capacitor C and a flux Φ across the inductance L. b) Resonator energy levels, the parabola is given by the potential (inductive energy) and the gap between energy levels is uniform ($E_{n+1} - E_n = \hbar\omega_R$).

2.2 Circuit QED building blocks

The idea behind artificial two level systems is to find an object, like an atom or a material, that has two energy levels we can address and control. On the other hand it is possible to artificially build such systems. That's the case of superconducting qubits, constituted by several non equi-spaced energy levels, artificially designed. In this chapter I will introduce first the basic models used in superconducting circuits, especially the Josephson junction, that is the base of every superconducting qubit. The chapter will then continue with the coupling between these elements. In this project only capacitative coupling is considered, but in general it can also be inductive.

2.2.1 LC circuit model

The first model presented in this chapter is the LC circuit model or linear resonator. Such resonator can be modeled with a parallel LC circuit (fig. 2.2a), where the capacitance and inductance continuously exchange energy, just like in a mechanical pendulum, where the potential energy is periodically converted in kinetic energy and vice-versa. In order to get the LC model Hamiltonian, first it is good to remember that the energy associated with an electronic element is given by

$$E(t) = \int_{-\infty}^{t} I(\tau)V(\tau)d\tau \tag{2.16}$$

where I is the current across the element and V is the potential difference at its extremes. Given a circuit element and its potential difference V, it is

possible to define a flux associated to it (fig.2.2a shows the flux associated to the inductor) as

$$\Phi(t) = \int_{-\infty}^{t} V(\tau) d\tau. \tag{2.17}$$

By using the current-voltage (I-V) relations:

$$I_C = C \frac{dV_C}{dt} \tag{2.18}$$

for a capacitor with capacitance C and

$$I_L = \frac{1}{L} \int V_L \tag{2.19}$$

for an inductor with inductance L, the element energies can then be evaluated together with the formula 2.16. Considering the capacitative energy as a kinetic one, the LC-model Lagrangian where the flux Φ is used as a coordinate is

$$\mathcal{L}_R = \frac{C\dot{\Phi}^2}{2} - \frac{\Phi^2}{2L}. \tag{2.20}$$

A conjugate momentum to the flux can then be defined as

$$Q = \frac{\partial \mathcal{L}_R}{\partial \dot{\Phi}} = C\dot{\Phi} \tag{2.21}$$

that has the dimensions of a charge (it represents the charge Q stored on the capacitance, see fig.2.2a). By using the Legendre transformation

$$H = \sum_i (\dot{\Phi}_i \frac{\partial \mathcal{L}}{\partial \dot{\Phi}_i}) - \mathcal{L} \tag{2.22}$$

and using the ralation 2.21, finally the Hamiltonian is obtained:

$$H_R = \frac{Q^2}{2C} + \frac{\Phi^2}{2L} \tag{2.23}$$

The Hamiltonian can then be quantized, introducing creation and destruction operators that are functions of a charge operator $\hat{Q}$ and a flux operator $\hat{\Phi}$ [30]. So a quantum linear resonator Hamiltonian results in

$$\hat{H}_R = \hbar\omega_R \left(\hat{a}^\dagger \hat{a} + \frac{1}{2} \right) \tag{2.24}$$

where the natural frequency of the circuit is expressed as

$$\omega_R = \frac{1}{\sqrt{LC}}. \tag{2.25}$$

It is good to underline that the second term in the Hamiltonian 2.24 represents a parabolic potential, and the resulting energy levels are equally spaced by an amount $\hbar\omega_R$, as depicted in fig.2.2b.

2.2.2 3D waveguide cavity

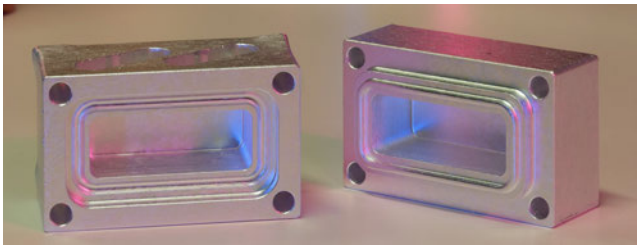

Figure 2.3: Two halves of a 3D waveguide aluminium cavity: The left side, on the top, has two holes for SMA connectors, used to excite the cavity modes. The two halves will be held together by screws inserted in the four corners. Indium is often also used to achieve a better sealing of the two halves.

In this project a 3D waveguide cavity is used as a linear resonator (fig. 2.3). This type of cavity is simply a metal box, where standing waves form between opposite walls. The frequency $\omega_{l,m,n}$ for each possible mode is a function of the three cavity dimensions, according to the formula [31]:

$$\omega_{l,m,n} = \frac{c}{\sqrt{\mu_r \epsilon_r}} \sqrt{\left(\frac{l\pi}{X}\right)^2 + \left(\frac{m\pi}{Y}\right)^2 + \left(\frac{n\pi}{Z}\right)^2} \tag{2.26}$$

Where X, Y and Z are the three cavity dimensions and l,m,n are natural numbers that are used to identify the mode (and the standing waves pattern).

Each cavity mode can be seen as an independent resonator. Beside the frequency, also the distribution of the electrical field changes for each mode. In fig. 2.4 the E-field for the first four modes is shown. In this experiment, I will only use the first mode of the cavity, given by (l,m,n) = (1,1,0).

Another important parameter is the quality factor Q that is used to characterize the losses of a resonator. It is defined as:

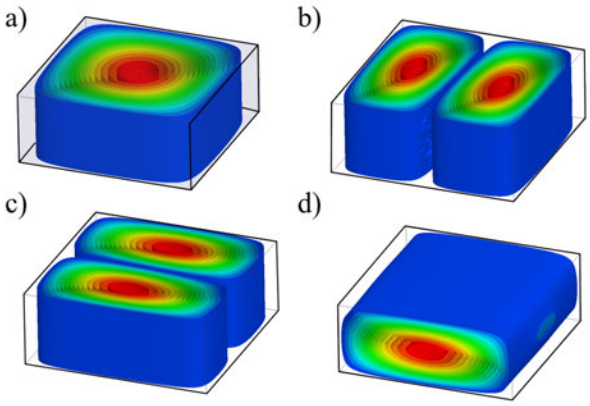

Figure 2.4: The electrical field intensity for the first four cavity modes are shown respectively from a to d. Red is high intensity, blue is low intensity (a.u.). The first mode (a) corresponding to TE_{110} is the one used in this project, with the maximum intensity of the E field in the cavity center.

$$Q = \omega \frac{\text{Total energy stored}}{\text{Total power dissipated}} = \frac{\omega}{\kappa} \tag{2.27}$$

where ω is the resonator frequency and κ is the energy decay rate. The reciprocal of κ can be seen as the average life time of a photon in the resonator.

In order to excite a resonator, it must be coupled to an external environment. Because of this coupling, the resonator quality factor will change. The total quality factor of the system Q_{tot} can be decomposed in two parts: the internal quality factor Q_{int}, that corresponds to the isolated resonator (losses of the material and imperfections on the surfaces) and the external or coupling quality factor Q_C, that is a complex number that is proportional to the coupling strength. The imaginary part of the coupling quality factor produces a phase shift of the signals that interact with the cavity. The total quality factor is evaluated as:

$$\frac{1}{Q_{tot}} = \frac{1}{Q_c^{Re}} + \frac{1}{Q_{int}} \tag{2.28}$$

where Q_c^{Re} is the real part of the coupling quality factor. The ratio between the external and internal quality factor is used to distinguish three cases:

$Q_c^{Re} \gg Q_{int}$	under-coupled regime
$Q_c^{Re} \approx Q_{int}$	critically-coupled regime
$Q_c^{Re} \ll Q_{int}$	over-coupled regime

In this project I will use the over-coupled regime for the resonator coupling. The advantage of the over-coupled regime is that $Q_{tot} \approx Q_C$ and so it is possible

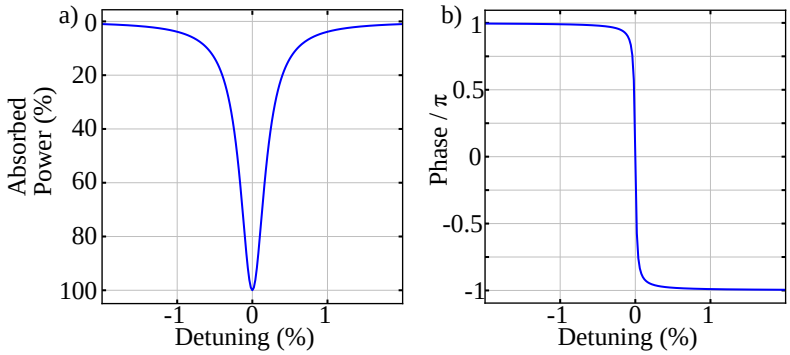

Figure 2.5: Example plots of power and phase of the cavity for $Q_C = Q_{int}$ in function of the frequency detuning: **a)** The signal power is absorbed at the resonance frequency, the width of the lorentzian is equal to κ (2.27). **b)** The signal phase undergoes a full period, following an arctangent function centered at the resonance frequency.

to engineer the resonator k with the coupling strength. Although a relatively small k is usually desired (explained in chap. 2) in qubits experiments, it also "slows down" the resonator. When a cavity mode is excited, it will require a long signal to actually excite the mode, and the same time will be required to "empty" it. The length of the signal is inversely proportional the the value of k. The possibility of engineering this value allows us to find a good trade-off between signal length and high Q_{tot}.

When the cavity is coupled to a drive, it is possible to excite a cavity mode and measure the output power S [32]:

$$S(\omega) = 2\frac{\frac{Q_{tot}}{Q_C}}{1 - 2iQ_{tot}\frac{\omega-\omega_R}{\omega_R}} - 1 \tag{2.29}$$

where ω_R is the cavity resonance and ω is the signal frequency. It is important to note that the absolute value of $S(\omega)$ it is a lorentzian distibution with a linewidth κ inversely proportional to Q_{tot} (2.27). The signal phase instead undergoes a transition from π to $-\pi$ following an arctangent function centered at ω_R. In fig. 2.5 an example of power absorption and phase change is shown for $Q_C = Q_{int}$.

Although dissipation is present in the resonator, the previously introduced LC model can be applied to a 3D waveguide mode coupled with an external drive (or environment). In this case the dissipation is "moved" to the environment, and the resonator is modeled as dissipation-less.

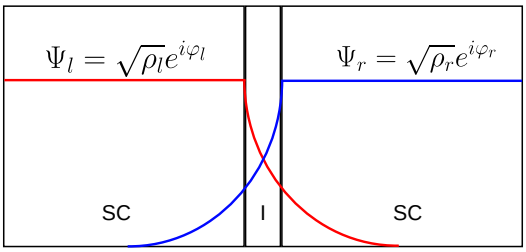

Figure 2.6: Schematic representation of a Josephson Junction: Two superconducting islands separated by an insulating material. The two $\Psi_{l/r}$ functions represent the Cooper-pair order parameter on the islands ($\rho_{l/r}$ is the charge density in each island). If the insulating barrier I is weak enough, a portion $K << 1$ of the Ψ_l can tunnel to the right superconductor and vice-versa (more details can be found in ref. [14], chap. 4).

2.2.3 SC qubits and the Josephson Junction

Typical SC artificial atoms are constituted by different energy levels that we can arbitrarily address. It is impossible to achieve this result with linear resonators[5], so we need to introduce a non-linear, dissipation-less element in the circuit. In superconducting circuits, the above mentioned non-linear device, that is the core of every SC qubit, is the Josephson Junction (JJ). This device is constituted by two superconducting plates separated by an insulating barrier (Fig.2.6) through which Cooper pairs[6] can tunnel. Each superconducting island will be in a state that can be described as:

$$\Psi = \sqrt{\rho} e^{-i\alpha} \tag{2.30}$$

where ρ is the charge density and α is a phase factor. The barrier must allow tunneling of the charges between the two superconductors. The current and voltage across the barrier obey the Josephson equations [14, 33]:

$$\begin{cases} I = I_C \sin(\varphi) \\ V = \frac{\Phi_0}{2\pi} \frac{\partial \varphi}{\partial t} \end{cases} \tag{2.31}$$

where I_C is the critical current (function of the thickness and area of the junction), φ is the phase difference across the junction and Φ_0 is the quantum flux, equivalent to $h/2e$. This two equations are valid when $I < I_C$, otherwise the JJ will behave like a resistor.

[5] A drive will excite several energy levels, creating a coherent state

[6] In a SC, the charge is called Cooper pair [14], constituted indeed by two electrons bound together and therefore with a charge value of 2 times the electron charge.

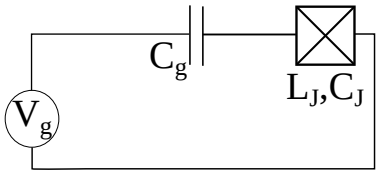

Figure 2.7: CPB circuit model: A Voltage generator is coupled to the Josephson Junction with a coupling capacitance C_g. The voltage provided can be used to change the charge offset n_g n the superconducting islands.

Using the formula 2.16 to calculate the energy of the JJ, we get the Hamiltonian:

$$H_J = -E_J \cos(\varphi) \tag{2.32}$$

with:

$$E_J = \frac{\Phi_0}{2\pi} I_c \tag{2.33}$$

defined as Josephson energy.

The phase φ can be related to the flux through the second Josephson equation (2.31) and the flux-voltage relation (2.17):

$$\varphi = \frac{2\pi}{\Phi_0}\Phi \tag{2.34}$$

By using this last relation and by comparison with the LC harmonic oscillator (2.24) we can associate a non-linear inductance to the junction:

$$L_J^{-1} = \frac{\partial^2 H}{\partial \Phi^2} = E_J \left(\frac{2\pi}{\Phi_0}\right)^2 \cos\left(2\pi\frac{\Phi}{\Phi_0}\right) = L_0^{-1}\cos\left(2\pi\frac{\Phi}{\Phi_0}\right) \tag{2.35}$$

where:

$$L_0 \stackrel{\text{def}}{=} \left(\frac{\Phi_0}{2\pi}\right)^2 \frac{1}{E_J} = \left(\frac{\Phi_0}{2\pi}\right)\frac{1}{I_C} \tag{2.36}$$

Because of the structure of the JJ, that is constituted by two SC islands and an insulator, we expect it to also have a capacitance C_J. The symbolic representation of a JJ can be seen in fig.2.7.

2.2.4 From CPB to the transmon

The first realized superconducting qubit is the Cooper pair box (CPB). It is characterized by a Josephson junction coupled to a voltage source through a capacitance C_g (fig. 2.7). The CPB Hamiltonian [11] is constituted by a

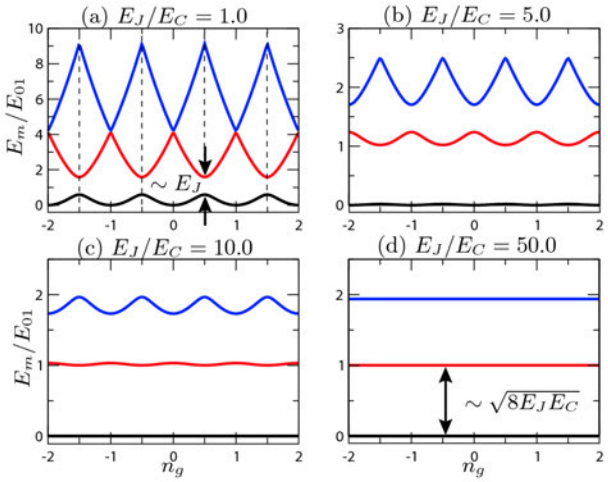

Figure 2.8: First three CPB energy levels as a function of the charge offset n_g: **(a)** The CPB is characterized by a ratio $\frac{E_J}{E_C} \approx 1$. **(b,c,d)** The energy levels "flattens" when the ratio $\frac{E_J}{E_C}$ is increased. **(d)** For $\frac{E_J}{E_C} > 50$ the energy levels are practically constant and insensitive to variations of n_g. Image taken from ref. [11].

kinetic term, function of the capacitance $C_\Sigma = C_J + C_g$ and the Josephson potential 2.32:

$$\hat{H}_{CPB} = 4E_C \left(\hat{n} - n_g\right)^2 - E_J \cos(\hat{\varphi}) \tag{2.37}$$

where:

$$E_C = \frac{e^2}{2C_\Sigma} \tag{2.38}$$

and the factor of 4 takes in account the Cooper pair charge.

By changing the gate voltage V_g it is possible to change the charge offset n_g. In fig. 2.8, the effect of such a change on the CPB energy levels is shown. The classic CPB has a ratio between the E_J and E_C energies less or on the order of 1. In fig. 2.8a the first energy levels are shown for such a ratio. The energy difference between the black (ground level) and red lines (first excited level) is proportional to the qubit frequency. We can observe that changing the value of n_g changes the gap. The derivative of the energy levels with respect to n_g is the sensitivity (charge dispersion) of the CPB to charge fluctuations. For a CPB this is quite high and leads to qubit decoherence. Except energy minima, where the sensitivity is zero at the first order and they can be used as working points for qubit rotations. Increasing the $\frac{E_J}{E_C}$ ratio instead shows a reduction of the sensitivity, that becomes zero for values above 50. This

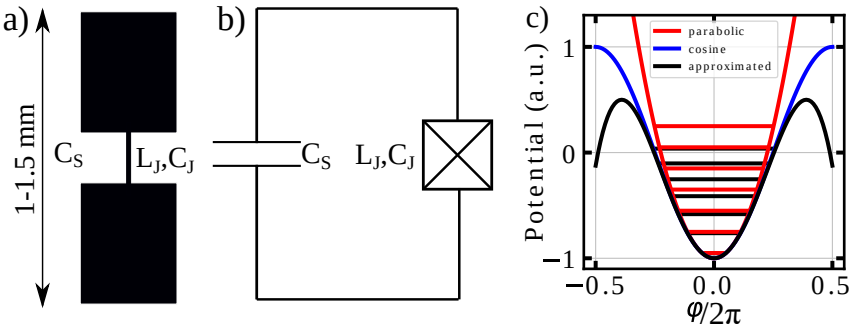

Figure 2.9: 3D transmon, circuit model and energy levels: **a)** 3D transmon with rectangular antenna pads, the JJ is placed in the middle of the wire connecting them, the shunt capacitance C_S is given by the pads size and their separation. **b)** circuit model of the transmon qubit, with a Josephson Junction on the right, characterized by a Josephson inductance L_J and a self-capacitance C_J, shunted with the additional capacitance C_S. **c)** One period of the Josephson cosine potential energy in blue; its approximation at the second order (parabolic, equivalent to a linear resonator) in red and with the fourth order correction in black. Energy has been normalized such that the cosine amplitude is 1. Energy levels in black are anharmonic, evaluated for a E_J/E_C ratio equal to 50.

evolution of the CPB (from charge sensitive to charge insensitive) is called transmon [11], a new kind of qubit that shows enhanced coherence compared to its ancestor. The price to pay is, however, a relatively small anharmonicity (In fig. 2.8d the difference between the blue and red line is a few % smaller than the difference between the red and black line).

2.2.5 Transmon qubit

In order to increase the ratio $\frac{E_J}{E_C}$ and bring it in the transmon regime (above 50), we need to increase E_J or decrease E_C. The increase of E_J can be achieved by fabricating a Josephson junction with a thinner barrier or with a larger area. However, there are practical limitations for such changes. The alternative is to decrease E_C by shunting the JJ with a relatively big capacitance. In this project I use 3D transmons (fig. 2.9a), that are characterized by having a big antenna pad for each superconducting island. The antenna pad can be designed to provide the additional capacitance that lowers E_C. The design used and the general transmon circuit representation are shown in figure 2.9a-b. The quantized transmon Hamiltoninan is equivalent to 2.37 but without

the n_g term:

$$\hat{H}_T = 4E_C\hat{n} - E_J\cos(\hat{\varphi}) \tag{2.39}$$

As already mentioned in the previous section, by comparing the transmon Hamiltonian with a Harmonic oscillator one, we can observe that E_C is related to a kinetic energy. Now that the kinetic component has been lowered compared to the potential (E_J), the phase φ will be confined in a minimum of the cosine shaped potential. We are allowed then to expand the cosine (typically up to the 4^{th} order, figure 2.9b)

$$\cos(\varphi) \approx 1 - \frac{\varphi^2}{2} + \frac{\varphi^4}{24} \tag{2.40}$$

Substituting the expansion in the transmon Hamiltonian 2.39 we get (constant terms in the Hamiltonian are neglected)

$$\hat{H}_T = 4E_C\hat{n}^2 + \frac{E_J}{2}\hat{\varphi}^2 - \frac{E_J}{24}\hat{\varphi}^4 \tag{2.41}$$

The first 2 terms bring us back to a harmonic oscillator Hamiltonian, allowing us to introduce two construction and destruction operators b and $b^\dagger$ like the ones for the LC. Where:

$$\begin{cases} \hat{n} = i\sqrt[4]{\frac{E_J}{32E_c}}(\hat{b} - \hat{b}^\dagger) \\ \hat{\varphi} = \sqrt[4]{\frac{2E_C}{E_J}}(\hat{b} + \hat{b}^\dagger) \end{cases} \tag{2.42}$$

such that the resonator energy is

$$\hbar\omega_{01} = \sqrt{8E_JE_C} \tag{2.43}$$

By adding and treating the fourth order Hamiltonian term as a perturbation we get

$$\hat{H}_T \approx (\sqrt{8E_JE_C} - E_C)\hat{b}^\dagger\hat{b} - \frac{E_C}{2}\hat{b}^\dagger\hat{b}^\dagger\hat{b}\hat{b}. \tag{2.44}$$

where RWA has been used, neglecting terms like $\hat{b}^\dagger\hat{b}\hat{b}\hat{b}$ and their conjugates. A comparison between the harmonic oscillator, full cosine potential and the approximation used, is shown in fig. 2.9. So a transmon is an anharmonic oscillator, and allows us to drive the population from one energy level to another avoiding 'climbing' the energy ladder like in a linear resonator. If the qubit is weakly driven, i.e. ${\Omega_D}^7 \ll$ anharmonicity, only two levels are effectively used, the Hamiltonian 2.44 can be further simplified to the ideal

[7] Ω_D is equal to $\Omega V_D(t)$ in equation 2.9

two level system one (2.3) with

$$\hbar\omega_Q = \sqrt{8E_J E_C} - E_C \tag{2.45}$$

2.2.6 Tunable frequency transmon

It is possible to create a frequency tunable transmon by changing the effective Josephson energy. By substituting the qubit JJ with two of them in parallel, a so called SQUID, we change the Josephson energy to

$$E_J^{eff} = 2E_J \cos\left(\pi \frac{\Phi_{ext}}{\Phi_0}\right) \tag{2.46}$$

where Φ_{ext} is an applied external flux (magnetic field through the SQUID area) and E_J is the Josephson energy of the two identical junctions. As one can notice from this formula, when the flux ratio is a multiple of 0.5, the energy goes to 0. The qubit frequency in this case is shown in fig. 2.10, in blue. With the vanishing of E_J, the transmon starts to become sensitive to charge fluctuations (it behaves like a CPB). Moreover, the sensitivity to flux fluctuations (derivative of the curve) is also high. To overcome this problem, it is possible to add a non-zero minimum to the E_J^{eff} by having two different JJ. We can then define the ratio:

$$d = \frac{(E_{J1} - E_{J2})}{(E_{J1} + E_{J2})} \tag{2.47}$$

as asymmetry factor. The Hamiltonian becomes

$$H_{aSQ} = E_J^{max} \cos\left(\pi \frac{\Phi_{ext}}{\Phi_0}\right) \sqrt{1 - d^2 \tan^2\left(\pi \frac{\Phi_{ext}}{\Phi_0}\right)} \tag{2.48}$$

with $E_J^{max} = E_{J1} + E_{J2}$. Also note that the points where the derivative as a function of the external flux is zero are known as 'sweet spots'. These are points where the qubit is not strongly influenced by flux noise[8]. By increasing the value of d, we can increase the frequency of the lower sweet spot. A graphical representation for the formula 2.48, where the parameters E_{J1}, E_{J2} and E_C have been fixed, is shown in fig. 2.10. For $d > 0$ a lower sweet spot with finite frequency starts to appear. As a consequence, also the flux sensitivity is reduced. It is usually a good rule to set the parameters such that the minimum qubit frequency is still in the transmon regime, ideally when E_{Jmin} is larger

[8]It is sensitive to the second order derivative

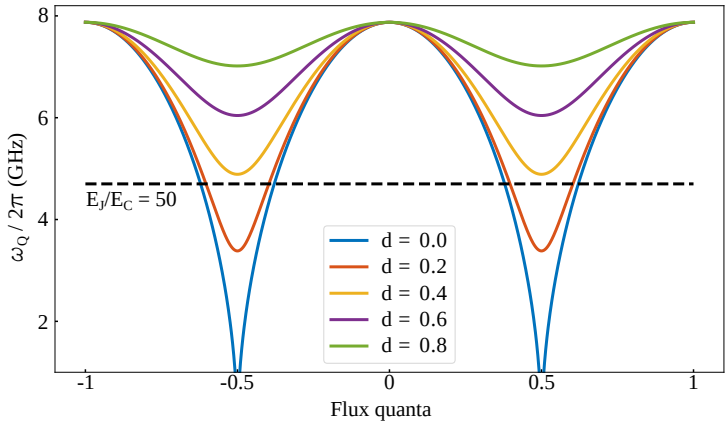

Figure 2.10: Frequency tunability for several asymmetry factors: $d = 0$ (blue) diverges, so only one sweet spot is available. For all the other values another sweet spot appears and its frequency increases proportionally to the d factor. The dotted black line represents the limit ($E_J = 50E_C$)for a good transmon qubit, if the qubit frequency is always above this line, the transmon will not be affected by charge noise.

than 50 E_C.

2.3 Circuit QED coupled system

Now that the basic building blocks of this project have been discussed, the capacitative coupling between elements is explained in this chapter. I will start with a coupling between two linear resonators, not used in reality in this project, but it is a good starting point to understand the coupling between a qubit and the linear resonator. The coupling between qubits and the 3D cavity is fundamental for the qubit state readout and, as a consequence, for the AQS readout.

2.3.1 Capacitative coupling between two linear resonators

Let's consider the case of two capacitatively coupled LC harmonic oscillators, where the circuit representation is shown in fig. 2.11. The circuit Lagrangian is

$$\mathcal{L}_{RR} = \frac{C_1}{2}\dot{\Phi}_1^2 + \frac{C_2}{2}\dot{\Phi}_2^2 + \frac{C_g}{2}(\dot{\Phi}_1 - \dot{\Phi}_2)^2 - \frac{1}{2L_1}\Phi_1^2 - \frac{1}{2L_2}\Phi_2^2. \tag{2.49}$$

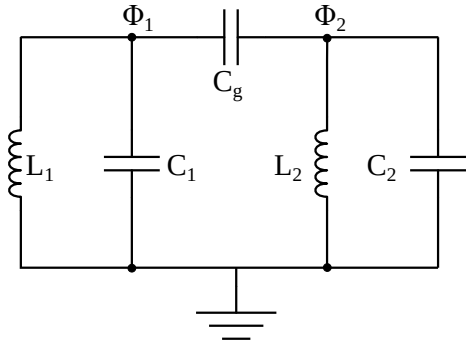

Figure 2.11: Circuit model of two coupled resonators: Two LC circuits can be inductively or capacitatively coupled (also both). In this project only capacitative coupling is considered, here given by the capacitance C_g.

The conjugate momenta of the fluxes are

$$\begin{pmatrix} Q_1 \\ Q_2 \end{pmatrix} = \begin{pmatrix} C_1 + C_g & -C_g \\ -C_g & C_2 + C_g \end{pmatrix} \begin{pmatrix} \dot{\Phi}_1 \\ \dot{\Phi}_2 \end{pmatrix} \tag{2.50}$$

that show how the capacitange C_g couples the charges of the two LC circuits. By applying the Legendre transformation on the Hamiltonian we get

$$H = \frac{(C_1 + C_g)}{2}\dot{\Phi}_1^2 + \frac{(C_2 + C_g)}{2}\dot{\Phi}_2^2 - C_g\dot{\Phi}_1\dot{\Phi}_2 + \frac{1}{2L_1}\Phi_1^2 + \frac{1}{2L_2}\Phi_2^2. \tag{2.51}$$

The first three terms of the Hamiltonian can be written in the following matrix form

$$H_C = \frac{1}{2}\begin{pmatrix} \dot{\Phi}_1 & \dot{\Phi}_2 \end{pmatrix} \begin{pmatrix} C_1 + C_g & -C_g \\ -C_g & C_2 + C_g \end{pmatrix} \begin{pmatrix} \dot{\Phi}_1 \\ \dot{\Phi}_2 \end{pmatrix}. \tag{2.52}$$

By inverting the matrix 2.50, 2.52 can be now written in terms of the charges Q_1 and Q_2. Adding the inductive parts to it results in

$$H = \frac{1}{D}\left[\frac{(C_2 + C_g)}{2}Q_1^2 + \frac{(C_1 + C_g)}{2}Q_2^2 + C_gQ_1Q_2\right] + \frac{1}{2L_1}\Phi_1^2 + \frac{1}{2L_2}\Phi_2^2 \tag{2.53}$$

where:

$$D = C_1C_g + C_2C_g + C_1C_2. \tag{2.54}$$

Now one can proceed with quantization as it is usually done. Here I will just introduce construction and destruction operators for the two resonators

by using the following relations:

$$\begin{aligned} \hat{\Phi}_1 &= \sqrt{\tfrac{\hbar Z_1}{2}}(\hat{a}+\hat{a}^\dagger); \quad \hat{Q}_1 = i\sqrt{\tfrac{\hbar}{2Z_1}}(\hat{a}^\dagger-\hat{a}) \\ \hat{\Phi}_2 &= \sqrt{\tfrac{\hbar Z_2}{2}}(\hat{b}+\hat{b}^\dagger); \quad \hat{Q}_2 = i\sqrt{\tfrac{\hbar}{2Z_2}}(\hat{b}^\dagger-\hat{b}) \end{aligned} \tag{2.55}$$

with:

$$Z_1 = \sqrt{\tfrac{L_1(C_2+C_g)}{D}}; \quad Z_2 = \sqrt{\tfrac{L_2(C_1+C_g)}{D}} \tag{2.56}$$

The Hamiltonian then transforms[9] into

$$\hat{H} = \hbar\omega_1\hat{a}^\dagger\hat{a} + \hbar\omega_2\hat{b}^\dagger\hat{b} + \hbar g(\hat{a}^\dagger\hat{b} + \hat{a}\hat{b}^\dagger) \tag{2.57}$$

with the following definitions:

$$\begin{aligned} \omega_1 &= \sqrt{\tfrac{Z_1}{L}} = \sqrt{\tfrac{(C_2+C_g)}{DL_1}} \\ \omega_2 &= \sqrt{\tfrac{(C_1+C_g)}{DL_2}} \\ g &= \tfrac{1}{2}\sqrt{\omega_1\omega_2}\,\tfrac{C_g}{(C_1+C_g)(C_2+C_g)} \end{aligned} \tag{2.58}$$

The first two terms of the Hamiltonian can be seen as effective resonances, indeed the coupling capacititance couple the charges of the two resonators, changing their effective impedances and resonances. The third term is an interaction term between the resonators, where the destruction of an excitation in one resonator is followed by the creation of an excitation in the second.

Now one can proceed to diagonalize the Hamiltonian and find the system energies:

$$\hbar\omega_\pm = \frac{1}{2}\left(\hbar\omega_1 + \hbar\omega_2 \pm \sqrt{4g^2+\Delta^2}\right) \tag{2.59}$$

where Δ is the difference between the coup;led resonances. It is interesting to note that, when Δ is equal to 0, the two eigenmodes are separated by a distance equal to 2g, known as avoided crossing.

2.3.2 Coupling between a qubit and a cavity mode

Let's now consider a capacitative coupling between a resonator and a qubit. For a 3D transmon, the coupling strength is proportional to the dipole moment of the antenna and the electrical field strength in the cavity. How the interaction strength can be engineered is explained in ref. [5]. As discussed

[9]Fast rotating terms in the 2.57 are neglected using the rotating wave approximation, since g $\ll \omega_1, \omega_2$. Also constant terms have been neglected.

in section 2.3.1, this kind of coupling couples the charges, with an interaction term defined as g (I will use J when two qubits are coupled).

In section 2.2.5 I have shown that the transmon Hamiltonian is composed of a linear part H_0 and a perturbative term coming from the 4^{th} order cosine expansion. This last term introduces a non-linearity that is equal to the capacitive energy.

Treating the qubit as an effective two level system, the interaction part of the full Hamiltonian becomes (RWA is used)

$$\hat{H}_{RQint} = \hbar g(\hat{a}^\dagger \hat{\sigma}_- + \hat{a}\hat{\sigma}_+) \tag{2.60}$$

for a linear resonator (with $\hat{a}^\dagger$ and $\hat{a}$ the creation and destruction operators) and qubit ($\hat{\sigma}_+$ and $\hat{\sigma}_-$ as raising and lowering operators) coupled together. Or

$$\hat{H}_{QQint} = \hbar J(\hat{\sigma}_{1-}\hat{\sigma}_{2+} + \hat{\sigma}_{1+}\hat{\sigma}_{2-}) \tag{2.61}$$

in the case of two qubits coupling. This last interaction is similar to the one between two spins, introduced in chapter 1. So by engineering properly the interaction strength J, we can simulate the exchange interaction between spins with 3D transmons.

2.3.3 Purcell effect

In chapter 2.2.2 I said that the cavity has a decay rate that is a function of the intrinsic losses and the coupling with the environment. Now that I discussed the coupling between the qubit and the cavity, one can realize that the qubit and the environment are indirectly connected. This decay channel is known as Purcell effect [34] and it can be evaluated with the formula

$$\Gamma_P = k\left(\frac{g}{\Delta}\right)^2 \tag{2.62}$$

where k is the resonator decay rate which is inversely proportional to the total quality factor, g is the coupling strength between the qubit and the resonator and Δ is their frequency difference. So the system should be properly designed such that the qubit lifetime is not limited by the Purcell effect. For a frequency tunable qubit, ideally Γ_1 should not be limited by the Purcell effect for all the frequency range. In this project the cavity frequency is always higher than the qubits frequency, so the frequency corresponding to $E_{Jmax} = E_{J1} + E_{J2}$ should be smaller than the cavity resonance. In some experiments Purcell filters [35] are used to lower the Purcell decay rate.

2.3.4 Dispersive regime

A special case regarding the qubit-resonator coupling is the dispersive regime, where the coupling g is much smaller than the qubit and resonator frequencies and their difference Δ. It is possible to derive the dispersive Hamiltonian by using a unitary transformation [11] on the Hamiltonian $\hat{H}_{tot} = \hat{H}_R + \hat{H}_T + \hat{H}_{int}$ (respectively 2.24, 2.3, 2.60).

Before showing the result, it is important to define the dispersive couplings $\chi_{i,j}$ as

$$\chi_{i,j} = \frac{g_{i,j}^2}{\omega_{i,j} - \omega_R} \tag{2.63}$$

where the indexes refer to the qubit energy levels, g is the coupling between the qubit and the resonator, but in function of the involved levels excitations in the qubit, $\omega_{i,j}$ is the transmon energy gap divided by $\hbar$ and ω_R is the resonator frequency. These terms are coupling terms, and affect both the resonator and qubit resonances. Moreover, because of the coupling between the qubit and the linear resonator, the latter also acquires an anharmonicity, although relatively small.

The dispersive Hamiltonian is

$$\hat{H}_{Disp} = \hbar(\omega_R' + \frac{\chi}{2}\hat{\sigma}_z)\hat{a}^\dagger\hat{a} + \frac{\hbar}{2}\omega_q'\hat{\sigma}_z. \tag{2.64}$$

where the qubit resonance $\omega_q' = \omega_q + \chi_{0,1}$ and the resonator frequency $\omega_R' = \omega_R - \frac{\chi_{1,2}}{2}$ has been renormalized by the $\chi_{i,i+1}$ quantities, called Lamb shift. The term χ in the equation 2.64 is instead equal to:

$$\chi = \chi_{0,1} - \frac{\chi_{1,2}}{2} \approx -\frac{2g^2 E_C}{\Delta(\Delta - E_C)} \tag{2.65}$$

where the last term is valid for a transmon[10] [11] and from now on $g = g_{0,1}$[11]. In order to analyze the dispersive Hamiltonian, let's consider it under two aspects: the so called "number splitting", where the qubit frequency depends by the number of photons in the resonator; and the qubit readout, where the resonator frequency depends by the qubit state.

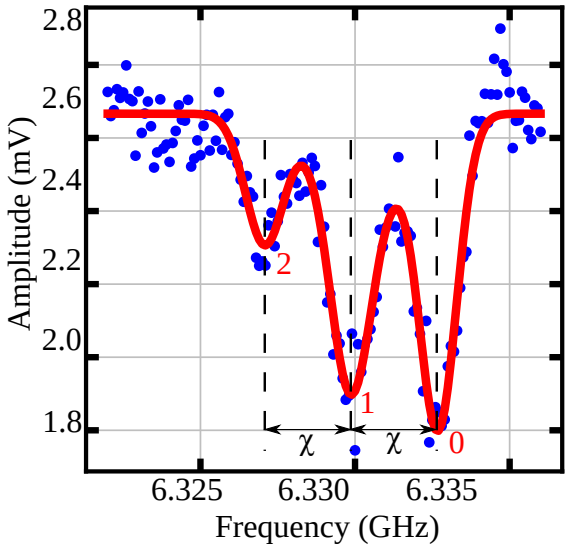

Figure 2.12: Number splitting example. When measuring the qubit frequency, if the cavity is in a coherent state $\alpha > 0$, more than one qubit resonance is found in the measurement. In the picture the rightmost peak corresponds to the qubit frequency when the cavity is not excited. The other peaks are separated by an amount equal to χ between each other. On the y-axis the amplitude of the readout signal transmitted though the cavity is linear, in mV. The amplitude of the peaks follows a poissonian distribution. In the example $\alpha^2 \approx 0.899$.

2.3.5 Number splitting

Combining the second and third term in equation 2.64 leads to:

$$\hat{H}_{NS} = \frac{\hbar\hat{\sigma}_z}{2}(\omega_q' + \chi\hat{a}^\dagger\hat{a}). \tag{2.66}$$

This equation shows that the qubit frequency shifts by an amount equal to χ multiplied by the number of photons in the cavity. When the cavity is in a coherent state α the probability of having Foch state $|n\rangle$ populated is:

$$P(n) = e^{-\alpha^2}\frac{\alpha^2}{n!}. \tag{2.67}$$

[10] By applying the two level system approximation before the unitary transformation, $\chi \approx \frac{g_{0,1}^2}{\Delta}$ is obtained. Expression typically valid for a CPB.

[11] For the last term of 2.65 $g_{n,n+1} = \sqrt{n}g_{0,1}$ is considered

So if the cavity is in a coherent state, the qubit transition frequency will split in several peaks, this phenomenon is called number splitting. The frequency separation between neighbour peaks is χ and their amplitude follows a poissonian distribution. This relation between the qubit frequency and the cavity photon number introduces, unfortunately, another dephasing mechanism that contributes to lower Γ_2. As a matter of fact, if the qubit frequency changes, the qubit time evolution (2.8) also changes. Also the detuning between drive and qubit will change, compromising qubit rotations. The amount of dephasing added by thermal photons n_{th} in the cavity is [36]

$$\Gamma_{TP} = n_{th}\kappa\frac{\chi^2}{\chi^2 + k^2}. \tag{2.68}$$

This equation shows that to reduce this effects, besides cooling down the resonator as much as possible, it is better to use high quality resonators (low κ).

2.3.6 Qubit readout

Combining the first and third term in equation 2.64 leads to:

$$\hat{H}_{QR} = \hbar(\omega'_R + \frac{\chi}{2}\hat{\sigma}_z)\hat{a}^\dagger\hat{a}. \tag{2.69}$$

In this case the frequency of the cavity is dependant on the qubit state. If the qubit is in the ground state the cavity frequency is $\omega'_R + \frac{\chi}{2}$ and if the qubit is in the excited state it is $\omega'_R - \frac{\chi}{2}$, for a total shift equal to χ.

In order to distinguish the two peaks it is necessary to have $\chi \approx \kappa$ or $\chi > \kappa$. In this way it is possible to measure the qubit state by measuring the power transmitted/reflected by the cavity or the signal phase change, like it is shown in fig. 2.13.

In case of two qubits coupled to the same resonator instead, the resonator part of the system Hamiltonian will be the sum of two different χ_i, corresponding to the two different qubits

$$\hat{H}_{QR2} = \hbar(\omega'_R + \frac{\chi_1}{2}\hat{\sigma}_z^{(1)} + \frac{\chi_2}{2}\hat{\sigma}_z^{(2)})\hat{a}^\dagger\hat{a}. \tag{2.70}$$

Even if the qubits are perfectly identical, the two χ_i terms can be engineered to be different. For example the two qubits can be coupled to the resonator in a different way or the frequency detuning with respect to the resonator is larger for one of the two qubits.

An example of the readout for two non-interacting qubits is shown in fig.

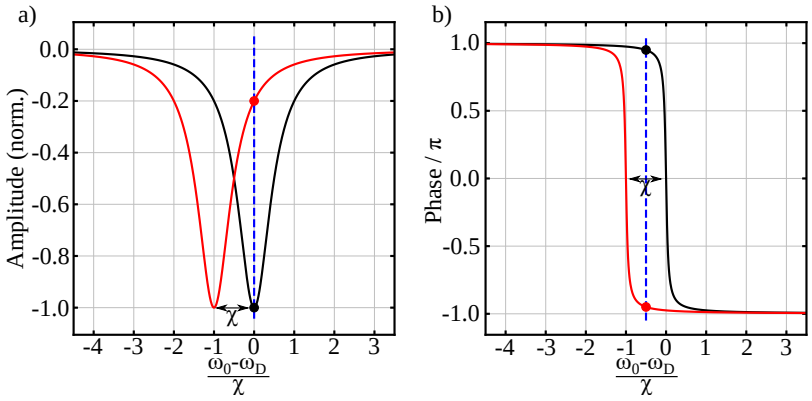

Figure 2.13: Dispersive shift example for a resonator with $\chi = \kappa$. **a)** Example of the dispersive readout for a power measurement, where ω_D is the signal frequency. When a signal with frequency $\omega_D = \omega_0 = \omega'_R + \frac{\chi}{2}$ is used, the measured value corresponds to the black marker when the qubit is in the ground state and to the red marker when it is in the excited state. The maximum contrast is given when the readout frequency is fixed on one of the two resonances. **b)** For a phase measurement instead the optimal readout is obtained when the signal frequency is in the middle of the two resonances.

2.14. If both qubits are in the ground state, the cavity resonance frequency is maximum (blue lorentzian). If the first qubit is excited, the cavity resonance frequency shifts of an amount equal to χ_1 (black line). If the second qubit is excited, the cavity resonance frequency shifts of an amount equal to χ_2, supposed larger than χ_1 in the example (green line). Finally, if both qubits are excited, the cavity resonance frequency is minimum and the total shift is the sum of the two dispersive shifts $\chi_1 + \chi_2$ (red line).

A good way to readout the qubits state is to send a pulse with a frequency equal to $\omega_D = \omega_0 - \frac{\chi_1}{2} - \frac{\chi_2}{2}$. This frequency corresponds to the red dotted line in the fig. 2.14a. However, an amplitude measurement does not distinguish all the four cases in this way. The blue and red peaks are crossing each other at the readout frequency and the same applies to the green and black peaks. By measuring also the phase it is possible to plot the measurements in an I-Q plane by defining

$$\begin{aligned} I_S &= A_S \cos(\varphi_S) \\ Q_S &= A_S \sin(\varphi_S) \end{aligned} \tag{2.71}$$

where A_S is the amplitude of the measured signal and φ_S is its phase. The values of (I_S, Q_S) for all the four cases are shown in fig. 2.14b. The dots are separated both in amplitude (distance from the origin) and phase (angle with the I-axis) and so they can be distinguished even in presence of a few percent

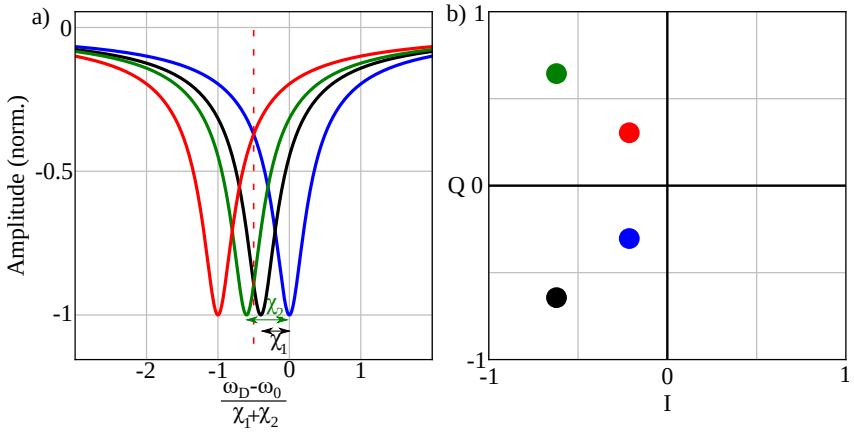

Figure 2.14: Dispersive readout example for two qubits dispersively coupled to the same resonator and with $\chi_2 > \chi_1$. **a)**The cavity frequency shifts as a function of which of the two qubits is excited (or both). A good way to measure the qubits state is to drive in the middle of the blue and red peaks, as shown by the red dotted line. Both amplitude and phase of the signal must be measured to distinguish all the four cases. **b)** From the amplitude and phase of the signal it is possible to plot the measurement in the I-Q plane, four different points correspond to the different cases in the example.

of noise.

This kind of measurement is however only possible if the two qubits are not interacting. In case of two interacting qubits in resonance, the two qubits would hybridize in a singlet or triplet state. In particular, the state $\frac{1}{\sqrt{2}}(|0,1\rangle + |1,0\rangle)$ corresponds to a so named "bright state". In this state the two electrical dipole moments of the qubits oscillate at the same frequency and with the same phase. In this situation it is not possible to distinguish which one of the two qubits is excited. The state $\frac{1}{\sqrt{2}}(|0,1\rangle - |1,0\rangle)$ instead cannot be measured and it is called "dark state". In this case the dipoles are again oscillating with the same frequency, but with opposite phase, creating a destructive interference. As a consequence there is no interaction with the resonator E field.

When a dispersive readout is performed with a few photons, this measurement is Quantum Non-Demolition (QND), meaning that projecting the state of the qubit, does not "destroy" its state. If the readout is repeated, it will give the same result unless the qubit state is decayed because of its limited lifetime. The number of photons typically used in this measurement should be less than [37]

$$N_{crit} = \left(\frac{\Delta}{2g}\right)^2 \tag{2.72}$$

where Δ is the qubit-cavity detuning and g is the qubit-cavity coupling. In summary less than a few tens of photons are used in a dispersive readout.

When more and more photons are used in the measurement, as the resonator energy levels start to fill, also the energy levels of the qubit will start to populate because of the coupling. In this situation the qubit will behave as a non-linear resonator and not anymore as a good two level system. This measurement is not anymore QND, but it is still possible to measure the qubit state.

When a high number of photons is sent to the resonator, one can observe that the readout peak at $\omega_R' - \frac{\chi}{2}$ starts to disappear as we increase the signal power. However, when the power is high enough to fill also the qubit levels, the hybridization between the qubit and the resonator is broken and a peak at frequency ω_R appears. It has been shown [38] that if the qubit is in the excited state, the power required to "break" the hybridization is lower. Because of this effect, a high-power readout for the qubit state is also possible. The advantage is a higher signal to noise ratio (SNR) but more time is required for the qubit and resonator to spontaneously relax. Also, one should consider possible overheating of the input line, with consequent increase of thermal photons. The number of photons necessary to "break" the qubit-cavity hybridization is on the order of 10^4 photons [37].

2.3.7 AQSIM readout concept

The goal of this PhD project is to design and experimentally realize a way to extract information from the AQS.

In the chapter 1 I pointed out that we need identical qubits in order to create the system we want to simulate, and that a first step would be to characterize the correlations between (at least) two qubits in the middle of a spin ladder. Therefore, some qubits are coupled to a linear resonator (the 3D cavity) and a dispersive readout can be performed (section 2.3.4) to know the qubit state, or a qubit pair correlation.

It should be possible to extract information from the simulator at any given time. If one wants to know a qubit or a qubit pair state, it should be possible to stop the interaction with the other qubits not involved in the readout. In this way the state will not change during the measurement time. In addition, the qubits that are not involved in the readout, should not be coupled to the resonator in order to avoid a non-direct interaction between them and the readout qubits. One way to stop the interaction between the readout qubits and the rest is through frequency detuning. When the readout is performed, the frequency of the readout qubits must be changed, in order to separate their frequency from the qubits in the rest of the chain. On the other hand,

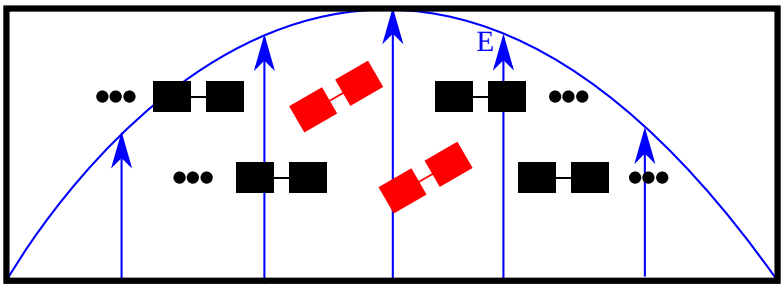

Figure 2.15: AQS spin ladder design: The qubits arrangement is geometrically identical to the spins in a 2D triangular spin ladder. In black, the 3D Transmon qubits used exclusively to simulate spin behavior, with their antenna orthogonal to the resonator E-field. The blue arrows represent the direction of the E-field and the curved blue line the intensity distribution (see also fig. 2.4). The readout Transmons, in red, are tilted such that the interaction is non-zero while still being coupled to the resonator.

the readout qubit frequency will be brought closer to the cavity frequency, keeping a resonable frequency difference such that a dispersive readout can now be performed.

So in summary, in order to have the desired readout we would need:

1. Tunable frequency qubits, coupled with the other qubits and the resonator

2. A linear resonator coupled only with the external world and the readout qubit pair

3. The possibility to interrupt the interaction between the readout qubits and the other qubits of the ladder

In a more general design, more resonators and readout qubits (or readout qubit pairs) can be used.

In ref. [5] it is explained how the interaction between 3D transmons is a function of the antenna angle. This allows us to achieve the first two points: by having the main chain qubits with an antenna orientation orthogonal to the cavity $\boldsymbol{E}$ field (fig. 2.15 in black), the interaction between them and the resonator is suppressed. For the readout qubit pair, it is possible to position the antenna diagonally in order to have a coupling with the other qubits and with the $\boldsymbol{E}$ field at the same time (fig. 2.15 in red). The readout qubits will also based on SQUIDs (chapter 2.2.6) to provide frequency tunability.

The correlation between qubit pairs can be measured as described in the previous section. I just want to underline that the two qubits should not be

hybridized. Frequency detuning between the qubit pair is a way to measure the state of both of them in a readout.

The frequency tuning of a transmon involves a magnetic field, however, in order to interrupt the interaction between the readout qubits and the chain qubits, we also should be able to change their frequency on fast timescales. In this case it means faster than the interaction strength between the qubits, which is on the order of tens up to hundreds of MHz. The realization of an AQS using 3D architecture has several good points, described already in chapter 1, but the injection of a magnetic field inside metal boxes like waveguides or cavities is a problem that needs to be solved.

If our cavity would be fabricated from copper, changing the field would be prevented by Eddy currents and their decay time is on the order of tens of ms. For an SC cavity which is typically preferred in SC circuits experiments, the Meissner effect would prevent flux to enter the cavity, even at DC. Inserting a coil or bias lines inside the cavity is not a solution, since they will couple to the qubit providing a lossy decay channel for it and also for the cavity itself. Indeed, all experimental efforts introducing control lines into waveguide cavities allow only for the application of DC magnetic fields [39] and even reduce the quality factor of the cavity to 10^5 or less [40, 41].

This PhD project solves the flux injection problem in 3D structures used to change the qubits frequency. The proposed solution to this problem, is through the use of a so called magnetic hose, presented for the first time in ref. [15]. In this article, the authors could already demonstrate experimentally that a DC magnetic field is transferred four times more efficient through the hose in open space as compared to e.g. a ferro-magnetic rod. However, the hose must be modified to ensure that it can work with AC fields in the range of (10 - 100) MHz and to avoid dissipating the cavity and qubit energies.

In the next chapter I will talk about the magnetic hose concept, design and simulation results.

Chapter 3

Magnetic hose for cavities and waveguides

In the previous chapter I explained the dispersive readout when one or two qubits are coupled to a resonator. Then I explained how to apply the readout to the analog quantum simulator and the necessity for frequency detuning. The frequency tunability of the AQS readout qubits requires magnetic fields. Magnetic fields must be changed on timescales $< 100\,\text{ns}$. In order to overcome the Meissner effect of a SC cavity and reach such fast timescales, a solution must be found. The magnetic hose is the solution to this problem proposed in this project. In this chapter first an ideal magnetic hose is presented. Then the chapter continues with the design of a meta-material based hose that approaches the behavior of the ideal one. Simulation have been performed on the hose with the meta-material structure to have an idea of its behavior when it is inserted inside a cavity wall. The magnetic field is provided by a coil places outside the cavity and the field is evaluated inside the cavity, around the qubit position. In the example shown in this chapter, two qubits have been used. The chapter concludes with an explanation about the assembling of hte real hose, how it is inserted into the cavity and how it is thermalized.

3.1 Hose concept

Nowadays many artificial materials with unique properties related to their electric permittivity ϵ and magnetic permeability μ have been realized thanks to the application of transformation optics [42]. In ref. [15], the authors have used this technique to realize a material that can transfer magnetic field from one point of the space to another without any alteration. Given a propagation direction x, they have shown that such material would need to have a magnetic

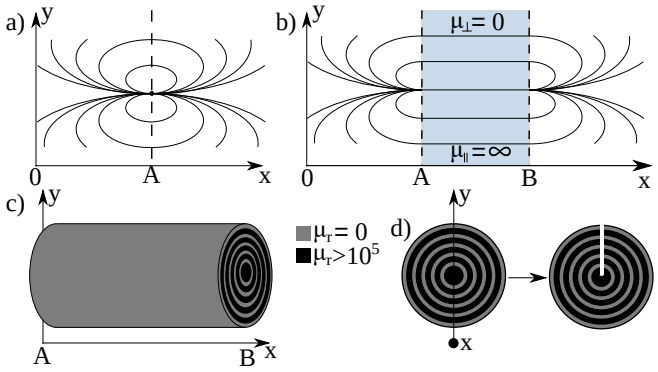

Figure 3.1: Hose concept and ideal magnetic field transfer: **a)** In a free space where a magnetic field is propagating, an ideal material with a μ_r perpendicular to the propagation direction equal to zero and a μ_r parallel to the propagation direction equal to ∞ is inserted at point A. **b)** The field propagates inside this ideal material without any curvature and without losses. Effectively "stretching" the space from A to B. **c)** A magnetic hose is realized in a cylindrical shape, with alternating layers of a high magnetic permeability material and a superconductor ($\mu_r = 0$). **d)** Front view of the hose. A cut is made along the hose, from the perimeter to the center, to avoid circulating currents in the SC shells.

permeability along the y and z directions $\mu_y = \mu_z = \mu_\perp = 0$ and a magnetic permeability along the propagation direction $\mu_x = \mu_{||} = \infty$.

To have a better understanding of the concept, let's imagine the field produced, for example, by a small magnetic dipole, as shown in fig.3.1a. The idea is to create a cut in the space, along the dotted line at the point A, and separate the two parts. The gap between A and B needs to be filled with a material that is able to transfer the field that enters from one side to the other side, without any curvature and dissipation, like in fig.3.1b.

An intuitive way to understand why $\mu_\perp = 0$ is needed is that, in this way, the field in the medium cannot curve from the propagation direction, and so it must move on a straight line. $\mu_{||} = \infty$ instead acts like the iron in a transformer, it is used to help the propagation of the field. The higher the μ_r, the lower the losses.

A material with such properties does not exist in nature, but it is possible to create an artificial material that can approximate the behavior of the ideal one. So a meta-material structure with alternating layers of a ferromagnetic material with high magnetic permeability[1] and a superconducting material ($\mu_r = 0$) has been designed. The higher the layers density, the more the meta-

[1]We used annealed μ-metal, that should have a $\mu_r > 80000$

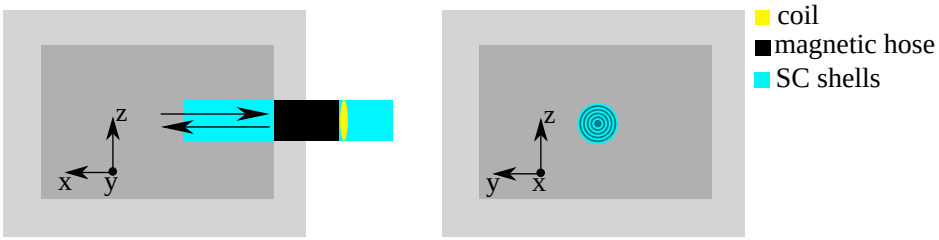

Figure 3.2: Magnetic hose and cavity: The magnetic hose is inserted only in the cavity wall, the SC shells extends inside the cavity and only the outer SC shell extends outside the cavity. The magnetic field can enter and exit through the hose, allowing injection also in superconducting boxes. A coil is placed outside the cavity and inside the extend outer shell. To avoid field dispersion before the produced magnetic field reaches the hose, the coil is placed as close as possible to it.

material will approach the ideal one. A cylinder made of this meta-material is used in this project and it is shown in fig.3.1c.

A cut along the cylinder radius is made to prevent circulating currents in the shells. These currents forms inside a superconducting loop when an external field is applied. These current loops creates a magnetic field that opposes to the applied field, cancelling it. Breaking the SC loops with a cut also prevents magnetic field to be trapped during the normal metal-superconductor transition when cooling down.

Unfortunately, the use of a ferro-magnet is not ideal in superconducting architectures because it can dissipate energy. So placing the hose inside the cavity and close to the qubit would lead to dissipation. For this reason the hose has been modified like it is shown in fig.3.2. A hole is drilled into the cavity wall and the magnetic hose is inserted only into the wall, while the superconducting shells are extended further into the cavity. The purpose of the SC shells inside the cavity is to guide the magnetic field and avoid dispersion before it reaches the qubit SQUID. However, because of the lack of the ferromagnetic shells, part of the magnetic field will route back and go out of the cavity before reaching the qubit (see fig.3.4). The outer shell of the hose extends also outside the cavity, it acts as a socket for the coil. Simulations have shown that the best efficiency is given by a discoidal coil[2]. The hose allows the magnetic field to enter the cavity, but also to exit (fig. 3.2). In this way the system can work also for SC boxes, because flux quantization is preserved as the net flux through the hose and hole section is zero.

[2]The idea is that the field that is closest to the hose, is less affected by dispersion and losses.

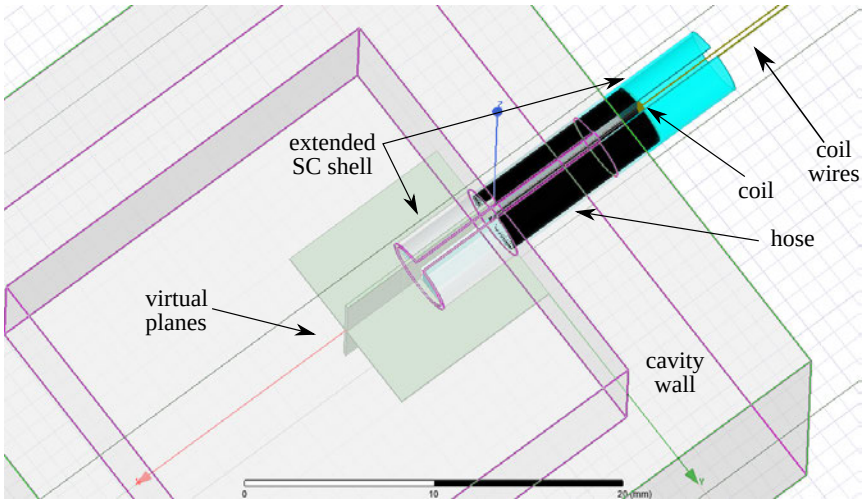

Figure 3.3: Screenshot of the design in the simulation software: the hose is constituted of 6 layers, as described in the text. In the figure the hose (black) sits in the cavity wall center and does not enter into the cavity space. The extended SC shells (light blue), enters 5 mm in the cavity. Two virtual planes used for the field evaluation are placed in the cavity center along the z and y directions. An higher mesh is used on the virtual planes. The discoidal coil is also simulated, where the wires can be stimulated with a current.

To evaluate the amount of field transferred to the qubit center or, more generally the field propagation into the hose and the cavity, a simulation with a finite element simulation software is performed. First a discoidal coil is designed and simulated, such that it produces $30\,\mu$T at its center, when a current of 1 mA is flowing through it. The hose is modelled in the simulation with 6 alternating layers of a material with $\mu_r = 10^{-8}$ ($\mu_r = 0$ is not allowed in the software, neither superconductors) and with $\mu_r = 10^4$. The hose, cavity and coil design in the software is shown in fig. 3.3

From now on the reference system in the simulations will have the x-axis along the hose axis and the z-axis upwards. The origin of the axis will be at the inner face of the cavity wall, as shown in fig.3.4. In this figure, results of the field propagation and field strength (B_x component) are shown. The inner hose SC extended shell is chosen 5 mm long and the qubit is placed on a sapphire substrate at the coordinates (6,0,0) mm (1 mm from the hose end). Another qubit is placed at coordinates (6,0,-2) mm. The simulated field is evaluated as 22.4 nT at the first qubit center and 5.8 nT at the second, corresponding to a flux cross-talk of 26 %. The total field transfer at the qubit on the center is on the order of 0.08 %. This seems a very low efficiency but it is actually much

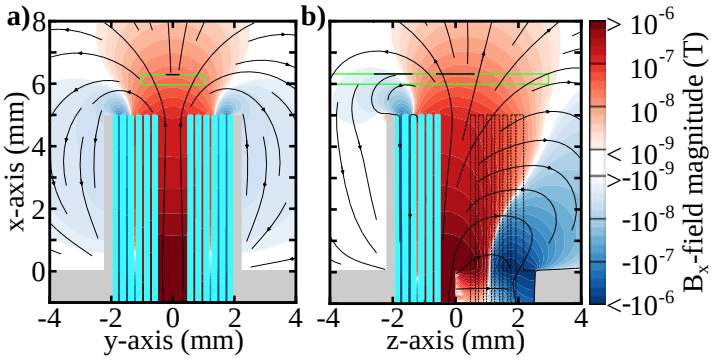

Figure 3.4: Top (a) and side (b) view of the setup, showing the magnetic field's x-component on a logarithmic scale, for the axis orientation refer to fig.3.2. The grey part depicts the cavity wall and the light blue surfaces indicate the superconducting shells of the magnetic hose, where the magnetic field is zero. The qubits positions are represented by black lines on green squares, which indicate the sapphire chips. The magnetic field distribution is calculated by a finite element simulation for the case of static magnetic fields. In this case the setup simplifies to its magnetic properties only and the superconductor and ferromagnet are approximated by materials with $\mu_r = 10^{-8}$ and $\mu_r = 10^4$, respectively. The field at the hose input is $30\,\mu$T.

better than the result without the hose, which is on the order of a few tens of fT.

For comparison, the same field value could be obtained with a coil placed at coordinates ($\approx 0.5,0,0$) mm. Simulation results for different coil placements are shown in fig. 3.5. A very strong point about the hose is that it acts as a filter that does not allow e.m. energy in the range of 0 - 60 GHz to pass through it, preserving in this way the system quality factor. This is obtained by the hose cut, that acts as a waveguide with a high frequency cutoff. The effect of this filtering will be experimentally shown in chapter 5. It is also worth to mention here that the experimental results show that the magnetic field at the qubit center is around 10 times larger than predicted. This means that actually to obtain the same field the coil has to be placed even more inside. The discrepancy between the simulations and the experiment is most probably due to the fact that it is hard to match all the parameters precisely in the real system and the simulation. A few iterations with different hose+cavity systems have been done to reach the final design and the improvements scaled up correctly with the simulations, suggesting that the discrepancy could actually be just an offset.

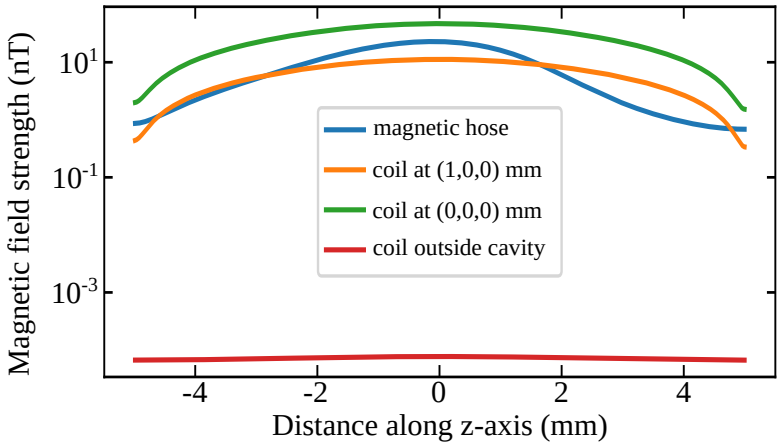

Figure 3.5: Comparison between hose and coil field at (6,0,0) mm: without hose and with the coil outside the cavity, only few fT of field can be found in simulations at the qubit center. The field that is obtained with the hose (22.4 nT), could only be obtained with a coil placed just inside the cavity, at 0-1 mm from the wall.

3.2 Manufacturing a magnetic hose

The SC hose shells are made of pure aluminium, that will become a superconductor below a temperature of 1 K. The aluminum shells are cut from a full aluminum block by wire erosion. At this stage the layer thickness is about 300 μm, which is close to the minimal thickness accessible using wire erosion before the shells are deformed. Next the aluminum shells are etched down to a layer thickness of about 150 μm using an aluminium etchant with an etching rate of 10 nm/s at 50 °C. The mu-metal parts are also cut by wire erosion. The central mu-metal wire is cut from a 1 mm thick mu-metal wire. The mu-metal shells are cut from a 100 μm thick mu-metal sheet and bent into cylindrical shape by hand afterwards. Finally, the individual parts of the magnetic hose are assembled by hand. One slides the individual shells on top of each other starting with sliding the innermost aluminum shell on top of the mu-metal wire. The coil is made out of a coated superconducting wire and it is wound around a stycast hand-crafted rod. It is then inserted into the extended outer SC hose shell. Everything is held by a copper clamp and the opening of the clamp is aligned to the hose cut, in order to not create a closed loop for currents. The clamp is fixed to the cavity with a screw and additionally it has a copper braid on one side, used for thermalization. A picture of the parts and the full assembly is shown in fig. 3.6

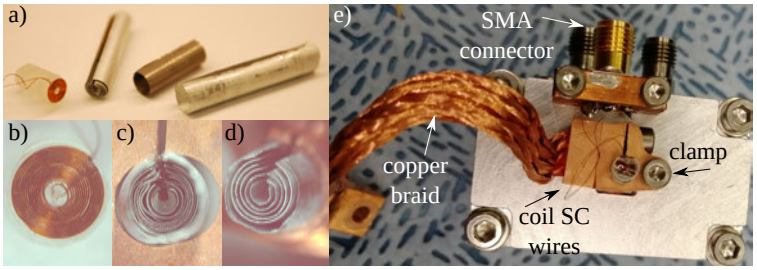

Figure 3.6: Parts of a magnetic hose. In a) a discoidal coil, an assembled core, a single mu-metal shell, and a single aluminum shell are depicted from left to right. Figure b) shows a close-up of the discoidal coil. In c) and d) the input side and output side of a fully assembled magnetic hose are visible, respectively. The outermost shell in c) is out of focus as it extends 5 mm out of the focus plane. e) Picture of the back of the cavity, with the copper clamp that holds the hose, an SMA connector with the SC coil wires soldered to it and a copper braid used for thermalization.

Chapter 4

Simulations

In chapter 2 the Hamiltonian of a system constituted by qubits and resonators has been shown. However, the parameters design becomes more and more complicated as the system scales up. Nowadays, Black Box Quantization (BBQ) [43] is used to design system parameters (in the dispersive regime). This theory allows the calculation of the system eigenmodes and anharmonicities in a way that can be done with classical[1] electromagnetic solvers. Such simulators have been used for decades for the simulation of devices like stripline, co-planar waveguides, cavities, etc. In this chapter, details about the simulation and black box theory application are carefully described. The aim of this chapter is to design a system constituted by a cavity and two 3D transmon qubits, built on the same sapphire substrate. Since a dispersive readout is desired, the frequency difference Δ between qubits and cavity should be much larger than the cavity-qubit coupling g, which means a $\Delta > 1\,\mathrm{GHz}$. The frequency of the first mode of the cavity for this experiment has been chosen to be higher than the qubit frequencies.

4.1 Black Box Theory

The relations that have been derived in chapter 2.3 must hold also for the Black Box theory. However, the system eigenmodes and anharmonicities are written in terms of the characteristic impedances of each mode. The reason behind this choice is that the characteristic impedances can be evaluated through a circuit simulation.

In the BBQ theory each system element is linear. Even the qubits are approximated by an LC circuit. However, anharmonicities are added to the system as perturbations afterwards. So each single system element is modeled

[1] No quantum mechanics is involved

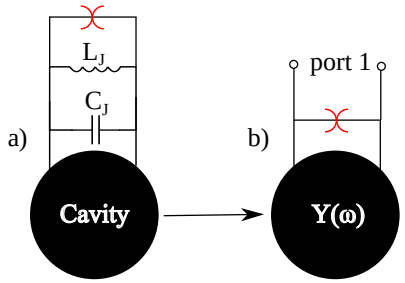

Figure 4.1: BBQ concept: **a)** All the circuit elements are linear, a qubit is modeled as a parallel L_JC_J circuit. The anharmonicity, represented by the red symbol, is added afterwards. **b)** The system admittance $Y(\omega)$ is evaluated through a port parallel to the junction. When the anharmonicity is introduced, all the single elements characteristic impedances (and resonances) will be influenced by it. This procedure can be scaled up with more resonators and qubits (and ports).

as a linear resonator and the full system, including the couplings, is considered as a "Black Box" (fig.4.1) with a given admittance $Y(\omega)$. The system admittance is evaluated through a port at the Josephson junction, as shown in fig. 4.1b. The system resonances occur when the imaginary part of the admittance $Y_{11}(\omega)$ is equal to zero.

Indeed, by considering a parallel LC circuit (2.2), its admittance Y is:

$$Y(\omega) = \left(\frac{1}{j\omega L} + j\omega C\right) = \left(\frac{1}{j\omega L}\right)\left[1 - \left(\frac{\omega}{\omega_0}\right)^2\right]. \tag{4.1}$$

This admittance is zero for ω equal to the resonance frequency ω_0 (2.25). From the admittance derivative $Y'(\omega)$ evaluated at the resonance frequency, one can evaluate the resonator impedance with the formula

$$Z = \frac{2}{\omega_0 \,\mathrm{Im}[Y'(\omega_0)]} = \sqrt{\frac{L}{C}}. \tag{4.2}$$

The impedances Z is used later as a weight to distribute the anharmonicity of the JJ. The higher the impedance of an element, the less its resonance will be affected.

With a finite element simulator it is easy to get the imaginary part of the full system admittance for each junction (or for each port). According to Fosters theorem [43], the linear part of the system can be written as a sum of

LC resonators. After quantization, the Hamiltonian is

$$\hat{H}_0 = \hbar \sum_{i=1}^{N} \left(\omega_i \hat{a}_i^\dagger \hat{a}_i \right) \tag{4.3}$$

where ω_i are the (effective) resonances extracted from the admittance and N is the number of resonators in the system.

The next step is the addition of the non-linearity into the system. Each resonance is shifted by an amount given by

$$\Delta_i^* = -\frac{e^2}{2L_J} \left(Z_i \sum_{j=1}^{N} Z_j - \frac{Z_i^2}{2} \right) \tag{4.4}$$

where Z_i is the impedance (eq. 4.2) of the i-th resonator. The effect of more JJ added to the system can be evaluated to first order by adding another port and repeating the process.

In equation 4.4 it is typical to isolate the term $i = j$, that corresponds to the resonator i "acquired" anharmonicity. It can be expressed as

$$\chi_{i,i} = -\frac{e^2}{2L_J} Z_i^2 = -\frac{C_J}{L_J} \frac{L_i}{C_i} E_C \tag{4.5}$$

with E_C equal to the effective qubit capacitive energy (2.38).

Summing up, for N elements in the system, the Hamiltonian becomes

$$\hat{H}_0 + \hat{H}_{NL} = \hbar \sum_{i=1}^{N} \left[\left(\omega_i - \sum_{j=1}^{N} \Delta_{i,j}^* \right) \hat{a}_i^\dagger \hat{a}_i + \frac{1}{2} \sum_{j=1}^{N} \chi_{i,j} \hat{a}_i^\dagger \hat{a}_i \hat{a}_j^\dagger \hat{a}_j \right]. \tag{4.6}$$

The dispersive shift terms $\chi_{i,j}$ are the terms in 4.4 with $i \neq j$, that can be evaluated using the anharmonicities as

$$\chi_{i,j} \approx -2\sqrt{\chi_{i,i}\chi_{j,j}}, \tag{4.7}$$

an approximation valid in the dispersive regime.

4.1.1 Example of a linear resonator coupled to a qubit

For a linear resonator R, coupled to a qubit Q, equation 4.4 simplifies to

$$\Delta_i^* = -\frac{e^2}{2L_J}\left(Z_i^2 + Z_i Z_j - \frac{Z_i^2}{2}\right) = \frac{\chi_{i,j}}{2} + \frac{\chi_{i,i}}{2}. \tag{4.8}$$

with i = R and j = Q or the opposite. By defining $\chi_{R,R}$ as α_R, $\chi_{Q,Q}$ as α_Q and $\chi_{R,Q}$ as χ, the system Hamiltonian is:

$$\hat{H}_{BBQ} = \hbar\omega_R^*\hat{a}_R^\dagger\hat{a}_R + \hbar\omega_Q^*\hat{a}_Q^\dagger\hat{a}_Q + \hbar\chi\hat{a}_R^\dagger\hat{a}_R\hat{a}_Q^\dagger\hat{a}_Q + \frac{\hbar\alpha_R}{2}(\hat{a}_R^\dagger\hat{a}_R)^2 + \frac{\hbar\alpha_Q}{2}(\hat{a}_Q^\dagger\hat{a}_Q)^2 \tag{4.9}$$

with:

$$\begin{aligned}\omega_R^* &= \omega_R - \tfrac{1}{2}(\chi + \alpha_R)\\ \omega_Q^* &= \omega_Q - \tfrac{1}{2}(\chi + \alpha_Q)\end{aligned} \tag{4.10}$$

It is worth to mention that in practice, the resonator and transmon frequencies are much larger than χ and α_R, so these terms in 4.10 can be omitted.

4.2 Architecture

Now that the Black Box quantization has been introduced, it is time to design and simulate the experiment. The architecture used in this project is a 3D waveguide cavity with two frequency tunable 3D transmon qubits. In the simulations the qubits are simulated as single JJ based 3D transmons. The aSQUID calculations can be done afterwards, without the simulator aid. After the parameters like dimensions, JJ inductance, etc. have been tuned, the next process is the physical fabrication of cavity and qubits. Explained in the second part of this chapter.

4.2.1 Single junction qubit design

In the following I explain the simulation procedure I performed using the HFSS software from Ansys. A sketch of the simulation setup is shown in fig.4.2.

A 3D waveguide cavity can be simulated by drawing a vacuum box,in grey in the figure. The box dimensions are evaluated in order to have the desired frequency for the first mode (see 2.26). The cavity width and depth are 22 mm and the cavity height is 10 mm.

The qubits are fabricated on a sapphire substrate with a width of 2 mm and a thickness of 330 μm. When the sapphire is placed in the cavity, the cavity frequency will be lowered.

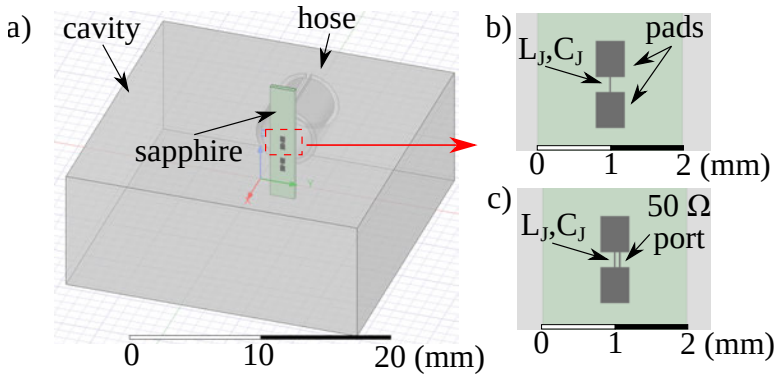

Figure 4.2: Simulation procedure: **a)** Full drawing of the cavity, hose and the sapphire with two qubits. **b)** Detail of the 3D transmon qubit, modeled with two PEC pads and a wire in the middle of the pads. An inductance L_J (around 4-6 nH) and a capacitance C_J (around 6 fF) are assigned to this wire. This is sufficient to evaluate the system eigenmodes. **c)** Another wire is created, parallel to the junction. To this wire a virtual 50 Ω port is assigned in order to measure the system admittance $Y_{11}(\omega)$.

As mentioned in section 2.2.2, the electrical field of the first mode is maximum at the center. However, in this project the substrate with the qubits is placed between the center and the cavity wall, as show in fig.4.3b and explained in chapter 3.

The next step of the simulation consists in placing the hose into the cavity, where for the simulation only the part inside the cavity matters. In this simulation the hose is centered at (x,y,z) = (0,0,0), it extends 5 mm into the cavity and has a diameter of 2.5 mm, with a thickness of 0.4 mm. The simulation includes also a 0.4 mm wide hose slit (chapter 3). The hose acts as a $\lambda/4$ resonator, creating an electrical field that can interact with the qubits, as shown in fig.4.3e-f. For this reason, the hose is designed to have a resonance frequency higher than the first mode of the cavity, at around 10 GHz. Together with the estimated hose-qubit coupling of 20 MHz, it will not influence the qubit decay through the Purcell effect (2.3.3).

The 3D transmon is designed as a Perfect Electrical Conductor (PEC) sheet, with two pads of dimensions 400 μm along the y-direction and 500 μm along the z-direction, separated by a gap of 200 μm, for a total antenna length of 1.2 mm (fig. 4.2b). One qubit is placed in the center (qubit center is at z = 0 mm), and the other is placed below, such that the qubit center-to-center distance is 2 mm (fig. 4.2a).

As mentioned in the previous chapter, the qubit is modeled as an LC circuit. The inductance L_J is provided by the Josephson junction in reality,

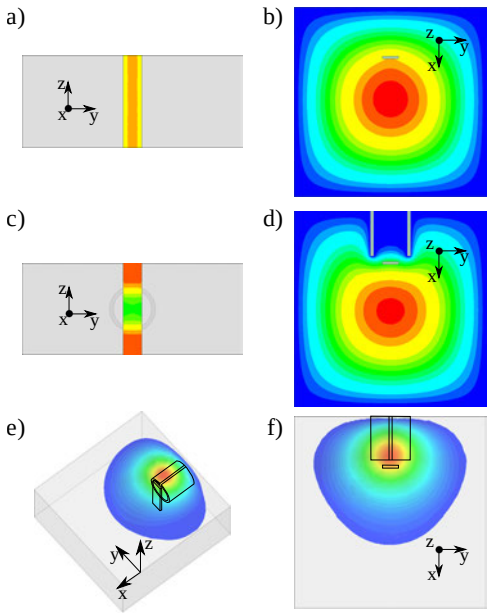

Figure 4.3: Simulated cavity modes: In all the plots red is the maximum field intensity and blue is the minimum. **a)** distribution of the electrical field on the sapphire chip, from this pictures we can see that the position of the qubit along the z-axis does not alter its coupling with the field. **b)** Top view of the field distribution inside a cavity with a sapphire chip at $x = 5\,\text{mm}$ from the wall ($x = 0$). **c)** The distribution of the electrical field on the sapphire chip changes with the presence of the hose. The hose effectively shields the qubit, lowering the coupling between the cavity and the qubits. The position of the qubits along the z-axis is now important. **d)** Top view of the field distribution of the fist cavity mode in presence of the hose. The hose is deforming the field, pushing it away. **e-f)** Hose electric field distribution inside the cavity. The hose acts as a $\lambda/4$ resonator with a frequency around $10\,\text{GHz}$

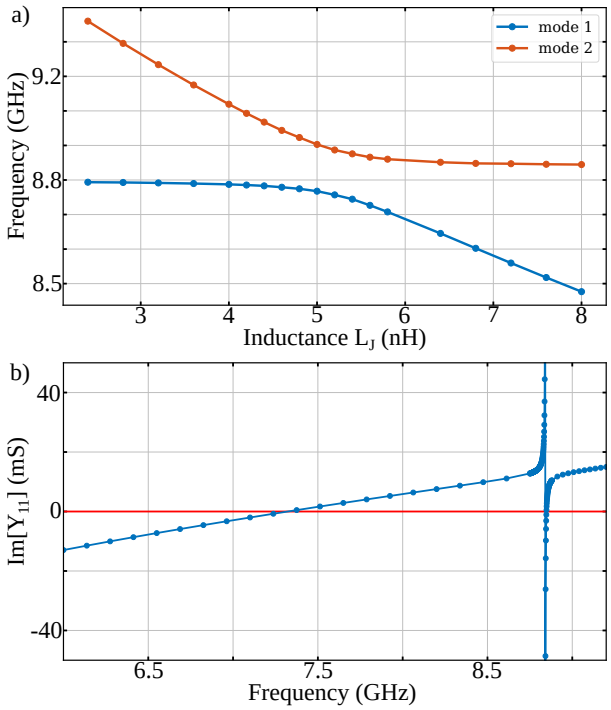

Figure 4.4: Simulation result examples: **a)** Measurement of an avoided crossing between qubit and cavity. For the simulator the two curves correspond to two different system modes. In reality the horizontal line at 8.8 GHz is the first mode of the cavity. The other curve is the qubit resonance, which changes its frequency as a function of the inductance. **b)** Simulation result of the imaginary part of the admittance measured through a port parallel to the junction. The line crosses the x-axis two times. Resonances and impedances are extracted from this plot and its derivative around the zero-crossings.

while in the simulation it is assigned to a PEC wire that connects the two pads. The capacitance C_J is also assigned to the same wire (fig. 4.2b). The total capacitance of the qubit is however engineered through the pads design and it will be evaluated by the simulation. Moreover, the hose proximity will increase the total capacitance compared to an empty cavity.

By progressively changing the inductance value L_J, it is possible to simulate the 'avoided crossing' (2.59, fig. 4.4a) between the two qubits, between qubits and cavity and finally between qubits and the hose mode. The minimum distance of the two resonances in the avoided crossing is given by two times the interaction strengths g or J.

Without hose, the evaluated qubit-cavity coupling for the center qubit is around 250 MHz. It drops to 80 MHz in presence of the hose which is due to

a shielding effect which can be seen in fig. 4.3a-c. The qubit-qubit interaction is 120 MHz with or without the hose. Simulations also show a 20 % variation of the capacitance of the qubit in presence of the hose.

To estimate the qubit anharmonicity α_q and the dispersive shift χ, a port is added to the system. It is placed parallel to the junction and it is connected to the pads (fig.4.2c). The imaginary component of the system admittance is evaluated as a function of the frequency, as required by the black box theory. The curve is shown in fig.4.4b. The curve crosses the zero value twice: the first crossing corresponds to the qubit resonance frequency ω_q, while the second one to the cavity resonance frequency. From the derivative of the function evaluated at the zeroes, the impedances and anharmonicities of the qubit and the cavity are estimated. Then finally the dispersive shift is evaluated using formula (4.7). The qubit and resonator frequencies must be corrected with the anharmonicities as shown in eq.4.10.

By using the formulas 2.36, 2.38 and 2.45 also the ratio E_J/E_C can be calculated. According to ref. [11], it should be larger than 50 for a transmon qubit.

4.2.2 aSQUID design

As mentioned before, in the simulation the value of the inductance L_J, related to the Josephson junction, is fixed. From the simulation all the other qubit parameters are extracted.

If the single JJ between the pads is substituted by a SQUID, with two JJs with inductances $2L_J$, the maximum qubit frequency would be unchanged[2]. However, the effective Josephson frequency is now magnetic flux dependant, as described in section 2.2.6, but it will have a minimum resonance frequency equal to zero.

In order to have a minimum finite frequency ω_{min}, we need to determine the right asymmetry factor and the correct split of the inductances L_1 and L_2. It can be shown, by evaluating the limit of the formula 2.48 at $\Phi_{ext}/\Phi_0 = 0.5$, that the asymmetry factor is given by

$$d = \left(\frac{\omega_{min}}{\omega_{max}}\right)^2 . \tag{4.11}$$

[2]The total inductance is the parallel of the two inductances, so: $L^{-1} = 2(2L_J)^{-1} = L_J^{-1}$

Knowing the required E_{Jmax} (formula 2.36 evaluated with L_J), the system:

$$\begin{cases} E_1 + E_2 = E_{Jmax} \\ \frac{E_2 - E_1}{E_2 + E_1} = d \end{cases} \tag{4.12}$$

must be solved to get the two E_i values related to the two different junctions.

4.3 Fabrication and assembly

The two aSQUID based qubits are fabricated on a sapphire substrate through electron beam lithography and aluminium deposition. The barrier is constituted by oxided aluminium, that is an insulator.

To realize the asymmetric SQUID based 3D transmon qubit for this project, two Josephson junctions with different areas are created. Indeed, the critical current density for each junction is the same, so a different area corresponds to a different critical current and different E_J.

The junction with larger area (figure 4.5a) is fabricated with a bridge-free technique [44]. The smaller JJ (figure 4.5b) is instead realized with a cross-junction [45] technique.

The qubits are fabricated locally, in the cleanroom of the University of Innsbruck. The combination of the two techniques mentioned above allows the creation of a large and small area JJ for one qubit.

After the fabrication, the normal state resistance R_n is measured. This can be done easily since the qubits are not connected by wires. The relation between the JJ critical current and its normal state resistance is given by [46]

$$I_c = \frac{\pi \Delta}{2R_n} \tag{4.13}$$

where Δ is the superconducting gap. By using formula 2.33 it is possible to get E_J from the critical current. In order to know the qubit frequency (or maximum frequency in the case of the tunable 3D transmon), it is necessary to know E_C (see formula 2.45). The capacitive energy can be quite accurately determined by the simulations. A more precise result is obtained through the measurement of the anharmonicity later in the experiment. 3D transmons with the same design will have the same E_C.

After selecting a chip with working qubits, it can be finally inserted in the cavity. In order to thermalize the sapphire, it will be held by a copper clamp, that can be inserted on the bottom of the cavity and tightened to it with screws. The sapphire will enter through a slit, at the bottom of the

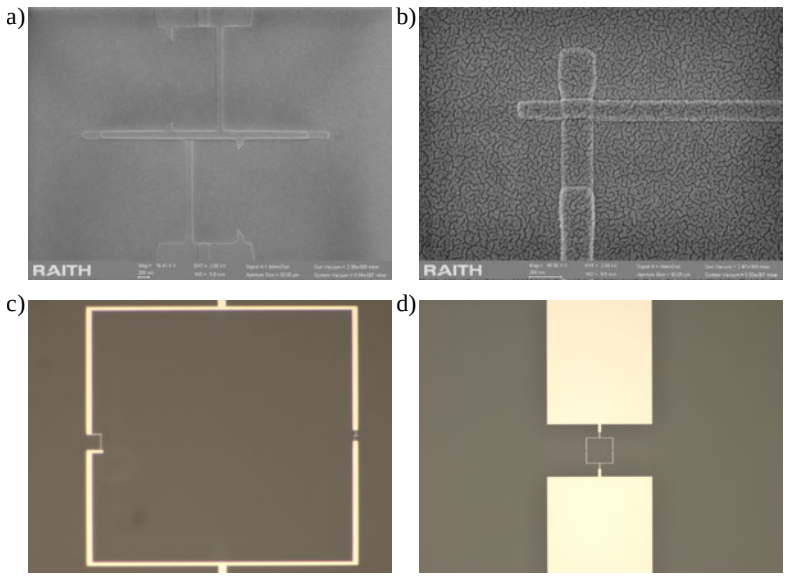

Figure 4.5: Scanning electron microscope (SEM) image of two Josephson junctions: **a** a large Josephson junction created with a bridge-free technique. **b** A small Josephson junction created with a cross-junction technique. The two asymmetric Josephson junctions in these pictures are the one used in the tunable 3D transmon used in this project. **c** aSQUID loop, with the small junction (b) on the left, and the large (a) on the right. **d** aSQUID loop (50x50 μm^2) with the two antenna pads (400x500 μm^2) connected to it.

cavity, placed around 6 mm from the wall. The sapphire thickness is taken in consideration such that the distance between the qubit and the hose is as close as possible to 1 mm. The clamp has also a copper braid that can be connected directly to the base plate of the cryostat.

Ideally the sapphire length is designed such that when it is flush to the clamp edge, one of the qubit is in the cavity center and in front of the hose center. However, since the assembly is done by hand, some imprecision must be taken in account.

The 3D waveguide cavity is composed of two halves, that will be closed with screws. In figure 4.6a the cavity half showing the hose on the backwall, and the qubits is presented.

Figure 4.6: Photograph of one half of a rectangular waveguide cavity with two transmon qubits fabricated on one sapphire piece, separated by a distance of 2 mm along the z-axis. The cavity is machined with an empty cylinder in the middle of the back wall to insert a magnetic hose. On the bottom of the cavity, a copper clamp is used to hold and thermalize the sapphire. On top of the cavity two holes are machined for the insertion of two pins, that act as antennas. SMA connectors are used to hold the pins and couple the cavity with the external environment. More details in chapter 5.

One can notice that the outer shell of the hose is machined out of the same block of aluminium as the rest of the cavity. This change has been made to prevent currents flowing on the outer shell surface to pass through the cavity

hole. This problem is not present in simulations, where the outer shell is 'fused' already with the cavity wall. So having the outer shell machined from the same aluminium block as the cavity, brings the reality closer to the simulations. The other shells are inserted into the hole and are almost flush with the embedded outer shell.

The two holes on top of the cavity will be used to couple the cavity to the external environment. The experimental setup and and measurement are described in the next chapter.

Chapter 5

Experimental setup and measurements procedures

5.1 Experimental setup and instruments

In the previous chapters I explained that the aim of this project is to test the magnetic hose on two flux-tunable aSQUID based qubits. The system can be designed and simulated thanks to the BBQ theory and a finite element simulator (see chapter 4). The aim of this chapter is to explain the measurements that have been performed with the aim of testing the qubits behavior and the hose.

Before proceeding with the measurements, the coupling between the cavity and the external world is needed. Without this coupling, one would not be able to interact with the system, for example by sending microwave signals. The system needs also to be cooled down to temperatures as close as possible to the absolute zero. For this purpose, a cryostat is used.

So in this chapter I first describe how to carefully design the experimental setup outside and inside the cryostat. First the cryostat working principles is explained. Then I continue with the design of the input and output lines, used to transfer signals through the cryostat. How the coupling between these lines and the cavity and qubits system is done and the filtering used to reduce the environmental noise.

Finally I introduce some instruments that I used in this experiment. These devices work typically in the microwave regime (RF), from DC to a few tens of gigahertz.

5.1.1 Cryostat

Following the Bose-Einstein statistic, the temperature of a qubit should be much less than the qubit energy $\hbar\omega_Q$ divided by the Boltzman constant k_B. As an example, this equivalent temperature is around 240 mK for a qubit frequency of $2\pi \cdot 5$ GHz. However, a superconducting qubit should be ideally cooled as much as possible to reduce the probability of quantum jumps and make sure that it is in the ground state.

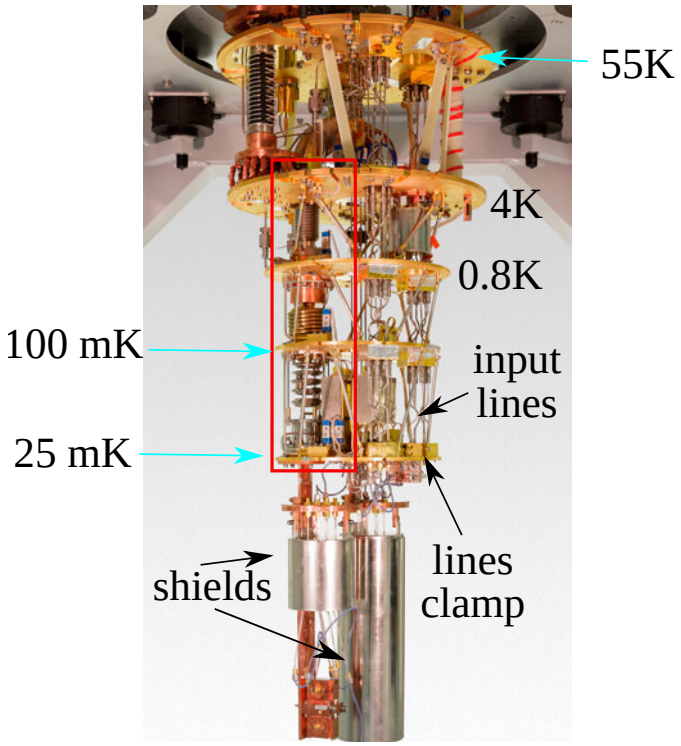

Figure 5.1: **a)** Picture of the cryostat showing its plates with their respective temperature, and the additional shields with a sample (a waveguide in this picture) at the bottom. The dilution unit can be seen in the red rectangle. Input microwave lines can be seen on the right side. These lines are fixed with clamps connected to each plate.

In order to reach such extreme temperatures, a cryostat must be used. The one used in our lab is a "cryogen free" dilution cryostat, meaning that it does not require a liquid Helium bath (4 K). The cryostat is divided in sections, each sperated by a plate with a different temperature and cooling power. A picture of the cryostat and the plates is shown in fig.5.1.

The first two plates are cooled down by a pulse tube. The pulse tube is a powerful pump that switches continuously between two reservoirs containing

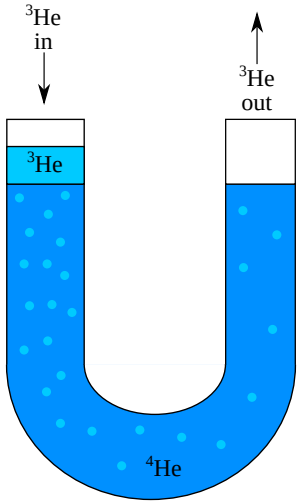

Figure 5.2: Scheme of a mixing chamber: The mixing chamber has an input, where ^{3}He enters, and an output, where ^{3}He evaporates. The ^{3}He (brighter color in the figure) deposits on the surface of ^{4}He and then naturally diffuses into it. On the other side of the chamber the ^{3}He is evaporated by using a pump to reduce the pressure. Then it is cleaned and kept into circulation.

Helium gas at two different pressures. Compression and decompression of a gas is a well known mechanism used to cooldown also domestic fridges.

At the begin of a cooldown, He gas is injected in the so called 'pre-cool' lines. Pre-cool lines are pipes that run through the plates and they can be used to thermally connect the bottom plates to the top section. The higher the pressure in the lines, the higher the thermal contact. The mechanism described so far, together with a vacuum of less than 10^{-6} Bar, is sufficient to bring all the cryostat base to around 10 K. During the cooldown, the pressure in the pre-cool lines is gradually reduced. When the thermal connection is interrupted by completely emptying the lines, the second plate of the cryostat will have a temperature of around 4 K. This temperature is sufficient to liquefy the ^{4}He.

When the cryostat base is below 10 K, a mixture of ^{3}He and ^{4}He is injected in the dilution lines (they are on the left in fig.5.1). The ^{4}He liquefies and deposits in a pot positioned at the base (bottom) plate of the cryostat, named mixing chamber (MXC). A mixing chamber scheme can be seen in fig.5.2

The ^{3}He enters the MXC input and deposits on the surface of the liquid ^{4}He. The ^{3}He will spontaneously dilute in ^{4}He and, since it has a lower boiling point, will then evaporate at the output. If the ^{3}He is continuously supplied at the input and expelled at the output, this mechanism can continue. The

passage of ^{3}He from the deposit at the input (pure phase) in the mix ^{4}He-^{3}He (diluted phase) increases the system entropy and so it absorbs heat. So everything connected to the base plate (and so to the MXC), will be cooled down.

The mix in a cryostat is in a closed circuit. After the ^{3}He exits the cryostat, it is cleaned by a cold trap. A cold trap is usually based on a set of pipes filled with an absorbent material (i.e. charcoal) and cooled down by liquid nitrogen. The idea is that everything but Helium freezes and stops circulating in the cryostat lines (also some Nitrogen could escape the trap). Colder (but smaller) cold-traps are inside the cryostat, to improve the cleaning, blocking also Nitrogen gas. The ^{3}He can in this way circulate continuously, allowing to keep the system running for long times (limited by problems like air leakage and condensation). The dilution of the ^{3}He in the liquid ^{4}He, brings the cryostat base temperature to less than 9 mK when the cryostat is empty. Because of the microwave lines (thermal conduction between plates) and because of additional shields and the samples, the base temperature usually rises to 20 - 40 mK. This temperature is still much less than the temperature of 240 mK estimated before. The excited state population for a qubit with a frequency of 5 GHz is around 0.2 % at 40 mK.

5.1.2 Microwave coaxial input lines

The lines used to bring a signal from room temperature to the base of the cryostat and to the sample must follow a few specifications. First of all the RF instruments connectors and cables are designed to have a 50 Ω impedance, so in order to have maximum power transfer and no reflections, coaxial cables that have such impedance at the frequency range of interest should be used for the cryostat lines. For the material, something that does not conduct heat well is needed to avoid overheating the several cryostat sections. The input lines have been hand fabricated from a steel coaxial cable and SMA connectors. Two sets of input lines have been designed and built, each constituted by six lines. A scheme of the input lines can be seen in fig.5.3. The set is divided in five sections, each section goes from one plate of the cryostat, to the next one. The steel lines are first cut longer than the distance between the plates, then bent in the center to avoid stress due to shrinking when cooling down. The SMA connectors, in stainless steel, have a ferrule made out of an alloy of Beryllium and Copper. The ferrule is soldered to the coaxial cables using a non-corrosive flux. The inner conductor and the ferrule, now soldered to the outer conductor, are inserted in the stainless steel part of the SMA connector. Each section has a male connector on one side and a female on the other. Each line is tested after soldering, ensuring that the reflection scattering matrix parameters are

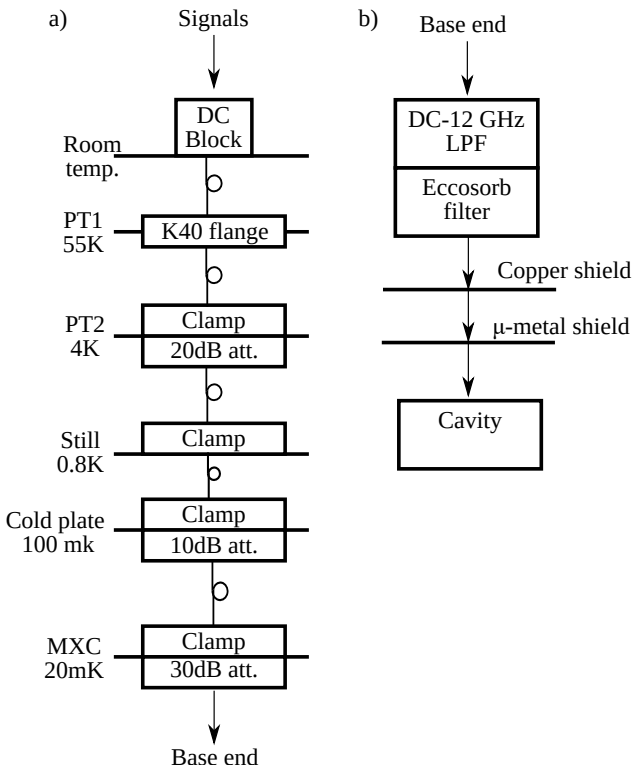

Figure 5.3: **a)** Input lines scheme. The lines are divided in five sections, one for each cryostat stage. The lines are made of stainless steel and are clamped to each plate for thermalization. This allows a simple change of the configuration at room temperature and at the base, but not in the middle. **b)** When the signals reaches the end of the input line, it undergoes filtering. Then it enters the additional shields before reaching the cavity. More details about input lines and filters can be found in the text.

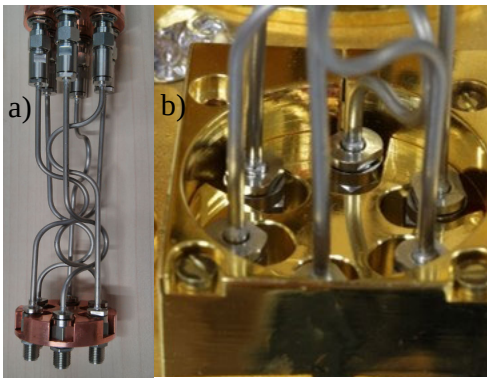

Figure 5.4: Input lines and clamps: **a)** One section of the input lines, that goes from one plate of the cryostat to the next one. On the top the male SMA connectors, connected to the female ones of the previous section. In the middle the cable bending can be seen. At the bottom, the female connectors are inserted and tightened into a copper disc, made of copper and used for thermalization. **b)** Each disc is coated with gold and is inserted into a clamp connected to the plate. Also these clamps are made out of copper with a gold coating.

below -20 dB in all the frequency range of interest (see fig.5.6a).

The female connectors are then inserted in a round copper disc where they can be clamped, the disc is coated with gold to avoid oxidation that would lead to a bad thermal conductivity. Clamps for these discs, also made out of copper and coated with gold, are mounted to each plate of the cryostat. They can be tightened around the disc with screws. Pictures of a section of the input lines and the clamp are shown in fig.5.4.

Since the cryostat will be under vacuum, SMA feedthroughs connectors with a vacuum seal are used on top of the cryostat. They are inserted in a K40 flange with machined D-shaped holes to prevent rotation. DC-blocks for the inner and outer coaxial conductors are also placed on the cryostat input lines, at room temperature, to avoid ground loops when connecting instruments to the lines. Flange and DC-blocks are shown in fig.5.5c.

Even if heat conduction between plates is reduced by a proper choice of materials, microwave lines can still transport thermal radiation from room temperature down to the base. In order to reduce this effect, attenuators are placed inside the lines, at different sections of the cryostat. One must consider, however, that despite attenuating the radiation and the signal, the attenuator will also radiate as a black body. In this experiment I used a 20 dB attenuator at the second plate of the cryostat (4 K), 10 dB attenuation at the cold plate and 30 dB attenuation at the base. In total the thermal radiation at room

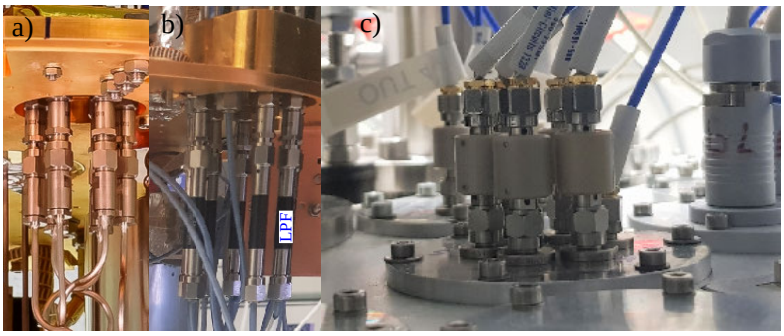

Figure 5.5: **(a)** Pictures of the 20 dB cryogenic attenuators mounted below the 4 K plate. **(b)** Picture of the 30 dB cryogenic attenuators followed by low pass coaxial filters (LPF), from DC to 12 GHz. Additional 10 dB attenuation is added at the cold plate. A single line without attenuation is used to excite the coil, with a low pass filter (not visible) from DC to 100 MHz. **(c)** DC-blocks for the inner and outer part of the coaxial lines are placed on top of the cryostat, to avoid ground loops. However, in this experiment one DC-block must be removed for the coil (rightmost connector). A K40 flange with vacuum compatible SMA connectors is also visible in the picture.

temperature will be attenuated by a factor of 10^6. The radiation produced by the attenuator at 4 K will instead be reduced by a factor of 10^4 and so on. With this choice, the thermal photons that arrive at the cavity can be estimated as:

$$n_{eff} = \frac{n_1(300\,\mathrm{K})}{10^6} + \frac{n_2(4\,\mathrm{K})}{10^4} + \frac{n_3(0.1\,\mathrm{K})}{10^3} + n_4(25\,\mathrm{mK}) \tag{5.1}$$

where n_i are the photons produced by black body radiation at the given temperature. Evaluating the effective photon number without attenuation, would give more than 400 thermal photons at 8 GHz. With the attenuation the number of thermal photons that reach the base is around 0.04 (in average). By reverting the Boltzmann distribution, it results in an effective temperature around 84 mK if evaluated at 8 GHz.

After mounting the set of microwave lines in the cryostat, it is tested at room temperature without the base attenuator. An example of a reflection and transmission measurement are presented in figure 5.6. In this plot the impedance match (the reflected power is below -20 dB) and the transmission loss are shown. The latter starts from the -30 dB of the attenuators for low frequencies and then gradually increases due to frequency dependence.

In order to reduce generic noise, at the end of the input line, low pass filters (LPF) are used. The filter used in this project has a frequency range from DC

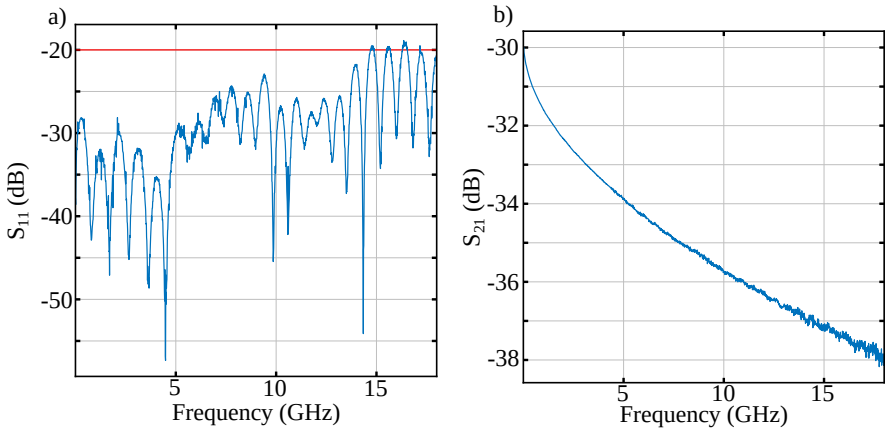

Figure 5.6: Scattering matrix parameters of an input line at room temperature. **a)** A reflected power below -20 dB means that less than 1 % if the signal is reflected (red line). The reflected power as a function of the frequency is below -20 dB up to at least 12 GHz. **b)** The transmission loss starts from the attenuator value and increases because of cable losses at higher frequencies. 4 - 6 dB of losses are expected in stainless steel coaxial cables around 70 cm long for frequencies between 5 - 10 GHz.

to 12 GHz. It is followed by a home-made Eccosorb filter (the fabrication is explained in the appendix) used to filter high frequency radiation (infrared). In pic.5.5a-b the attenuators and filter are shown (Eccosorb filter is not in the picture).

Since I plan to use a coil, which will be excited with a current that will change on time scales of nanoseconds, the same coaxial input lines are used for this purpose. Cryostats are usually supplied with lines used for DC coil excitation that are obviously not suitable for this experiment. For the bias fast-flux line, the last two attenuators are removed and the low pass filter is changed to a custom made DC-100 MHz LPF with low resistance. Commercial filters have a resistance close to 10 Ω, more than sufficient to overheat the system when hundreds of μA or more are sent to the coil. Also the DC-block on this selected line is removed from the top to allow a DC offset. The presence of the 20 dB attenuator at 4 K reduces the current by a factor of 10 (100 in power). So most of the power is dissipated there and it can lead to overheating at the second plate of the cryostat, limiting the amount of current that can be used.

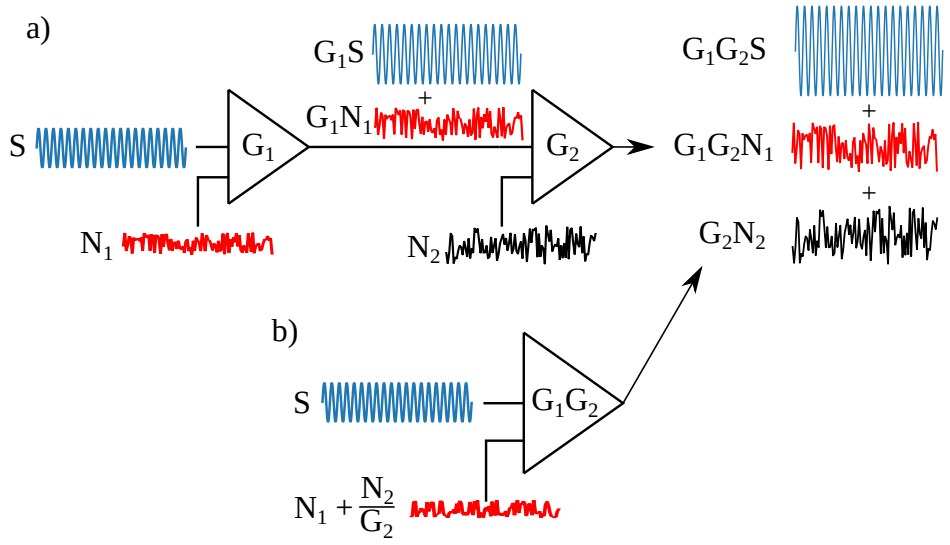

Figure 5.7: **a)** An amplifier adds some noise to the signal before the amplification. In a chain of two amplifiers, the initial signal S is amplified two times, together with the added noise. The noise of the second amplifier is amplified only once. **b)** Equivalent amplifier scheme. When a signal S is applied to an amplifier equivalent to the previous chain, the output must be the same. So the total gain is given by G_1G_2 and the added noise is $N_1 + \frac{N_2}{G_1}$.

5.1.3 Chain of amplifiers

Before describing the microwave output lines setup, it is important to explain how an amplification chain works. Since the input lines have a chain of attenuators, the total attenuation must be recovered by the output line. As a matter of fact, the output signal will pass through the several cryostat stages, with a higher and higher temperature, increasing the thermal noise. Since many instruments are typically sensitive to hundreds of μV, even more amplification is needed when only a few photons are used for a readout. Because of the small signal amplitude, amplifiers that are classified as ultra-low noise are needed for SC qubits experiments. These kind of amplifiers have a gain in the range of 20-40 dB. This does not provide sufficient amplification and so more than one amplifier must be used in cascade.

In fig.5.7 a scheme of two cascaded amplifiers is shown. The power of the signal that enters the first amplifier is multiplied by the amplifier power gain G_1. Then the amplified signal reaches the second amplifier and its again multiplied by its gain G_2. The power of the signal at the end of the chain

is G_1G_2S. An amplifier[1] adds noise to the signal, worsening the Signal-to-Noise ratio (SNR). It is typical to associate an intrinsic noise to an amplifier that is then added to the signal before the amplification. For this reason the intrinsic noise N_1 of the first amplifier in the chain will also undergo the same amplification of the signal, for a total of $G_1G_2N_1$. The noise of the second amplifier instead will be amplified only once. The full amplifiers chain can be represented as a single amplifier. When the same signal S is used, the output of this equivalent amplifier must be the same as before. So the equivalent gain is equal to G_1G_2, but what about the added noise? In order to have the same output, the noise added by the second amplifier must be divided by the gain of the first amplifier. In this way the equivalent noise results in $N_1 + \frac{N_2}{G_1}$. Multiplying the equivalent noise by the equivalent gain leads to the same output noise of before. Since the amplifiers gains are usually large number (typically larger than 100), the best SNR is obtained when the amplifiers are stacked in order of increasing intrinsic noise. However, also the amplifier saturation must be taken in consideration. At each stage of the amplifier chain, the signal plus the noise must be lower than the 1 dB compression point of the next amplifier.

In this project the first amplifier of the chain is placed at the second plate of the cryostat. It is a high electron mobility transistor (HEMT) amplifier. These amplifiers can work at a temperature of 4 K and provide around 30-40 dB of amplification with only a few photons of noise added. The HEMT used has a bandwidth in the range of 4-16 GHz. The gain and noise as a function of the frequency can be seen in fig.5.8c. The second amplifier of the chain, placed at room temperature, has a 40 dB gain, a bandwidth of 4-12 GHz and a noise temperature of around 120 K.

5.1.4 Microwave output lines

For the output lines of the cryostat a different design compared to the input line must be used. As explained, the output lines will have amplification instead of attenuation. However, the output line can also bring thermal radiation from the top part of the cryostat (mainly from the HEMT) down to the base, so attenuation is also required. In order to have attenuation from room temperature to the base (reverse direction) but not in the other direction (forward), cryogenic isolators are used, mounted at the base plate (see fig.5.9). Isolators are devices based on a permanent magnetic field and a ferrite, used to break the transmission symmetry of the device. Indeed, any two ports passive device is characterized by equivalent scattering matrix $S_{21}(\omega)$ and $S_{12}(\omega)$

[1] With the exception of a quantum limited phase insensitive amplifier

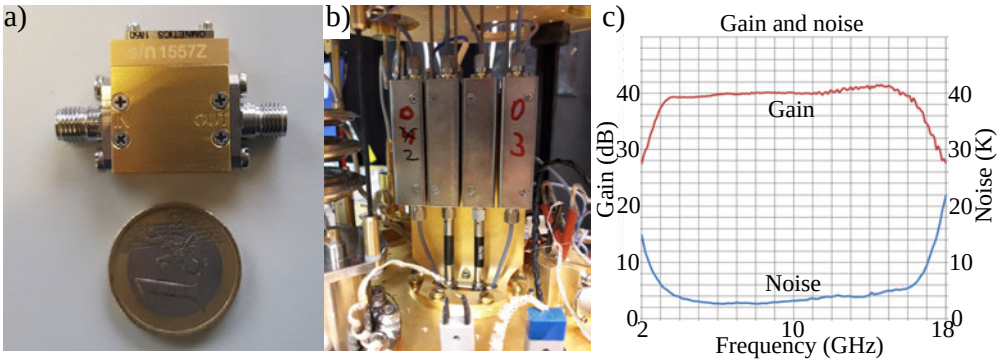

Figure 5.8: **a)** picture of a HEMT amplifier, placed at the 4 K plate, that provides around 40 dB amplification. **b)** Pictures of the isolators and filters. The signal passes first through the LPF coaxial filter (on the bottom), then through two isolators in cascade. This provides an attenuation of around 1 dB in the forward direction and around 40 dB in reverse. **c)** Gain and noise of the HEMT amplifier when its temperature is 5 K.

parameters. This simmetry can be broken by a ferrite or by using an active device, like a mixer or an amplifier. Two isolators in cascade offer an attenuation of 40 dB. A LPF from DC to 12 GHz is also added to the cascade to reduce thermal radiation at the base. A picture of the isolators and the filters can be seen in fig.5.8b.

For the signal transmission through the output lines in the forward direction, as little as possible attenuation of the signal is desired to get the highest SNR. For this reason superconducting coaxial cables connect the base to the 4 K plate. These lines are made of an alloy of Niobium (Nb) and Titanium (Ti) which is superconducting below 9 K. These lines cannot be bent as this alloy is very brittle. For this reason they are inserted in the "line of sight" port in the middle of the plates. Some space is left on the two extremities to avoid stress due to the thermal contraction and expansion during cooldown and warm up. It is possible to see these straight lines in the middle of the cryostat's plates in picture 5.1a and their schematic in fig.5.9.

After the HEMT amplifier, mounted at the top of the second plate, a coaxial line made of an alloy of Copper and Nickel is used to bring the amplified signal out of the cryostat. This alloy is used because it offers lower losses compared to a stainless steel and has less thermal conductivity compared to copper. At the output vacuum SMA feedthroughs and DC-blocks are used like for the input lines.

For the output lines the main source of thermal noise should be the HEMT amplifier. In the best case the noise can be modeled as black body radiation

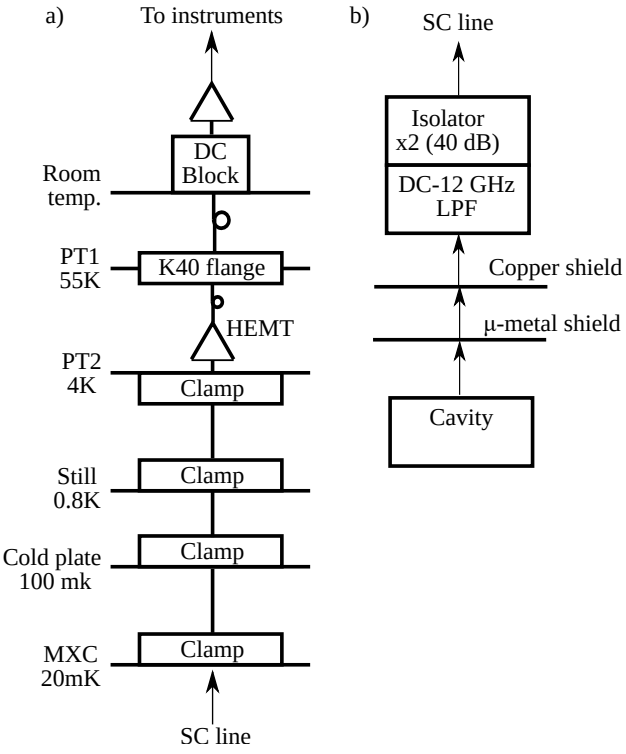

Figure 5.9: **a)** Output lines scheme. These lines are made out of a superconducting alloy of NbTi and are mounted in a straight line in the center of the plates. The top part, between the HEMT amplifier and the top of the cryostat, are instead coaxial cables of Cu-Ni with a bend in the center. More details in the text. **b)** The output signal passes through a LPF filter and two stages of isolation, for a total of 40 dB isolation in the reverse direction.

produced by a 50 Ω resistor at 4 K. This radiation is attenuated 40 dB by the two isolators. A small amount of noise is produced at the base (25 mK), by isolators and filters. The calculated effective temperature is around 56 mK at 8 GHz if no further thermal noise is added by the amplifier itself.

5.1.5 Sample mounting

After preparing the microwave lines it is time to think about mounting the system, at the base of the cryostat. Some space is reserved below the last cryostat plate. The total volume is around 60-70 cm, multiplied by the plate area of around 29 cm. The cryostat already has shields to protect the inside from e.m. radiation that would prevent reaching extreme temperatures. However, these shields are ineffective against magnetic fields and low frequency e.m. radiation. For this reason it is important to provide more shielding to SC systems.

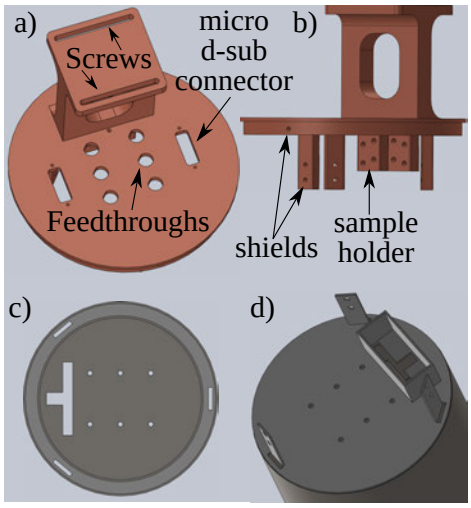

Figure 5.10: **a)** Schematic of the copper support for the additional shields, top view. Holes for screws, micro d-sub and feedthroughs connectors are visibile. **b)** Side view, where the supports for the bottom shields and the sample holder can be seen. **c)** Bottom view of the top part of the μ-metal shield, constituted by two concentric cylinders glued together. Both cylinders can be seen. Also the holes for the bottom shield supports and cables are more evident. The T-shaped cut is instead for the sample holder. **d)** Top view, where the supports can be seen.

A copper circular support (fig. 5.10a-b) is anchored with screws to the base plate. D-shaped holes are drilled in the support such that SMA feedthroughs

can be inserted and fixed to it. Also two holes for micro D-sub connectors are present, used for DC wiring.

The support is used to hold the additional shields, made out of μ-metal, that is effective against B-fields thanks to its high magnetic permeability. Also a vertical beam, made out of copper and with a T-section, can be attached to the support. Finally, another shield is added on top of the μ-metal one. I decided to use copper for this last shield, since Eddy currents can shield from high frequency e.m. fields. The Meissner effect of the SC cavity provides further shielding from magnetic fields. The full assembly is shown in fig. 5.11.

The μ-metal shield is divided in two parts: top and bottom. Each part is constituted by two concentric cylinders (fig. 5.10c-d). The cylinders of the top part are open on the bottom, while the cylinders of the bottom part are opened on the top. The bottom part inner cylinder slides into the gap between the two cylinders of the top part when mounting. As shown in fig. 5.11a.

The top part of the μ-metal shield is fixed just below the copper support. The top part has holes for coaxial cables and a big T-shaped slit used for the insertion of a vertical sample support. Also three slits can be seen on the perimeter (fig. 5.10c). These slits allow the supports of the bottom shield to pass through the top part and be anchored to the copper support as well, as shown in the inset of fig.5.11. SMA cables are assembled through the holes and connected to the support feedthroughs, in this way signals can pass through the shields and reach the cavity.

The cavity is placed on a copper beam with a T-section. On this beam I drilled 4 holes for the cavity and two for the copper braids. The screws I use are made out of stainless steel. Molybdenum washers are used to compensate the different thermal expansion coefficients of steel and copper during the cooldown. Alternatively brass screws can be used as brass shrinks more than copper. The copper beam can be easily attached to the circular support using screws. The idea is to keep the support with the top shield part always in place and remove only the vertical beam to change samples between cooldowns. After the vertical beam is installed, before closing all the shields, the cavity must be connected to the input and output lines. In the next chapter the coupling between the cavity and the lines is explained.

5.2 Coupling and signals

In chapter 2.2.2 I introduced the internal and coupling quality factors. In this section I explain how to engineer the coupling Q_C (real part) for the cavity, in order to connect the system to the input and output lines.

In the second part of this chapter I explain which instruments and signals

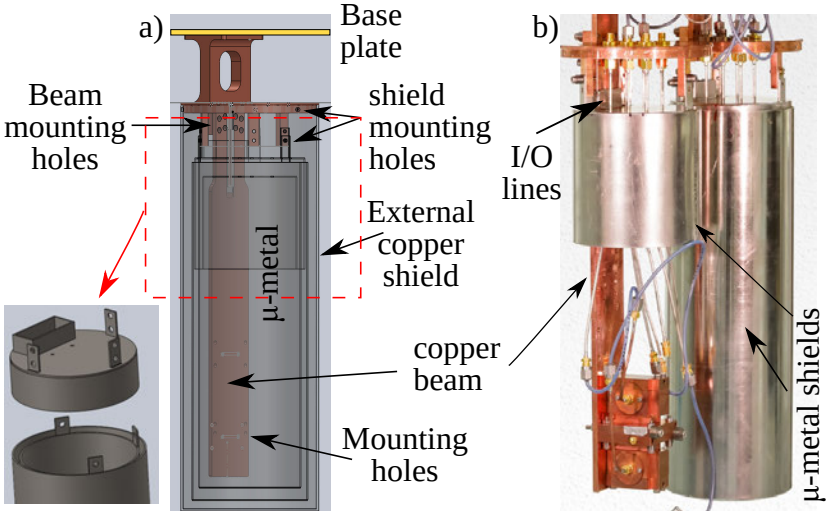

Figure 5.11: **a)** Schematic of the shields and the sample holder. This schematic shows also that an additional shield is added on top of the μ-metal one. In the inset (red rectangle) a schematic of how the two μ-metal parts are assembled together. **b)** Picture of the shields used to protect the sample, with the vertical copper sample holder on the left side. A waveguide in copper is mounted to the beam, on the bottom. On the right, the μ-metal shield is closed. On top of the shields, Input/Output coaxial cables made out of copper run through the holes in the shields and reach the top copper support.

are used in order to be able to perform a readout and drive the qubits.

5.2.1 System coupling to the lines

The coupling between the cavity and a $50\,\Omega$ coaxial microwave connector can be done by drilling a hole in the top part of the cavity wall and inserting a small pin, that acts as an antenna, inside the cavity. The pin (typically made of copper), can be inserted into an SMA flange connector. The more the pin enters the cavity, the stronger will be the coupling.

When cooling down the cavity from room temperature to base temperature, it is expected that the Q_{int} increases. Starting from a few thousands at room temperature, below 1 K the aluminium becomes a superconductor and the dissipation decreases. For a 3D waveguide cavity, that is divided in two halves, the seam between the two halves limits the Q_{int} to around 10^6. Q_C, on the other hand, is roughly constant during the cooldown as the pin shrinks when cooling down, but so does the cavity wall and the difference will be minimal.

With an instrument like a network analyzer, it is possible to measure the real and imaginary part of the reflected power (or amplitude and phase) and use the circlefit algorithm [47] to extract the cavity quality factors by using formula 2.29. In this way, starting with a long pin, it is possible to shorten its length and repeat the measurement until the desired Q_C is reached.

After tuning the Q_C to around $200 \cdot 10^3$, I performed a cold measurement of the cavity Q_{int} and Q_C. To connect the cavity port to the input and output lines, a circulator must be used. The working principle of a circulator is similar to the isolator, but it has three ports (see fig.5.12). A signal that enters the circulator, can propagate in forward direction with low losses. In the reverse direction around 20 dB of isolation is provided. The circulator is placed after the filters and before the additional shields. If port 1 is connected to the input line, then port 2 is connected to the cavity, and port 3 to the output line. In this way I can measure the reflected power when the cavity is at base temperature. In order to measure the cavity Q_{int}, the sapphire has not been placed inside the cavity, but the hose has been used. The aim of this measurement is, indeed, to ensure that the hose is correctly acting as a filter, avoiding losses otherwise introduced by the hole.

In fig. 5.13 the circle fit executed on this reflection measurement is shown. The fit parameters are the following:

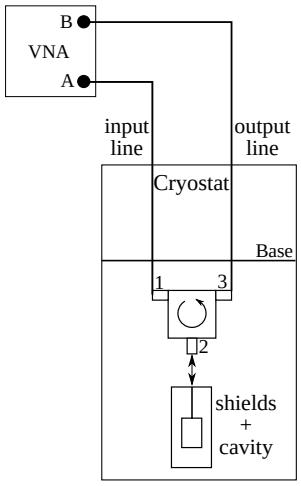

Figure 5.12: Schematic of a reflection measurement in the cryostat. In the example a circulator port 1 is connected to the end of the input line. The signal travels from port 1 to port 2 of the circulator with around 0.5 dB loss. From port 2 onward the signal enters through the additional shields, reaches the cavity and it is reflected back to the port 2. The isolation from port 2 to port 1 is up to 20 dB. Most of the signal coming from the cavity will propagate to port 3, connected to the base of the output line. A VNA measures the transmitted power from port A to port B.

Fit parameters	Value	Error
Q_C	$223.96 \cdot 10^3$	80
Q_{int}	$1.221 \cdot 10^6$	$6 \cdot 10^3$
Q_{tot}	$189.3 \cdot 10^3$	100
$\omega/2\pi$	8.94708432 GHz	10 Hz

The internal quality factor is close to the limit of a 3D waveguide SC cavity.

For the measurements in chap. 6 characterizing qubit and hose, I decided to measure the cavity in transmission, avoiding the use of the circulator. The reason behind this choice is to avoid having a magnetic field close to the system.

In order to perform a transmission measurement, it is possible to use two coupling ports and connect one to an input line and the other to the output. So I designed the input pin for a Q_{Cin} of around $200 \cdot 10^3$ and the output pin for a Q_{Cout} of around $10 \cdot 10^3$.

The two different Q_C for the input and output must be measured one at time, with the other pin removed. When the system is cold, the Q_{tot} will be practically equal to Q_{Cout}. A $Q_{tot} = Q_{Cout} = 10 \cdot 10^3$, results in a resonator linewidth of around 1 MHz for a cavity frequency around 8 GHz (formula 2.27).

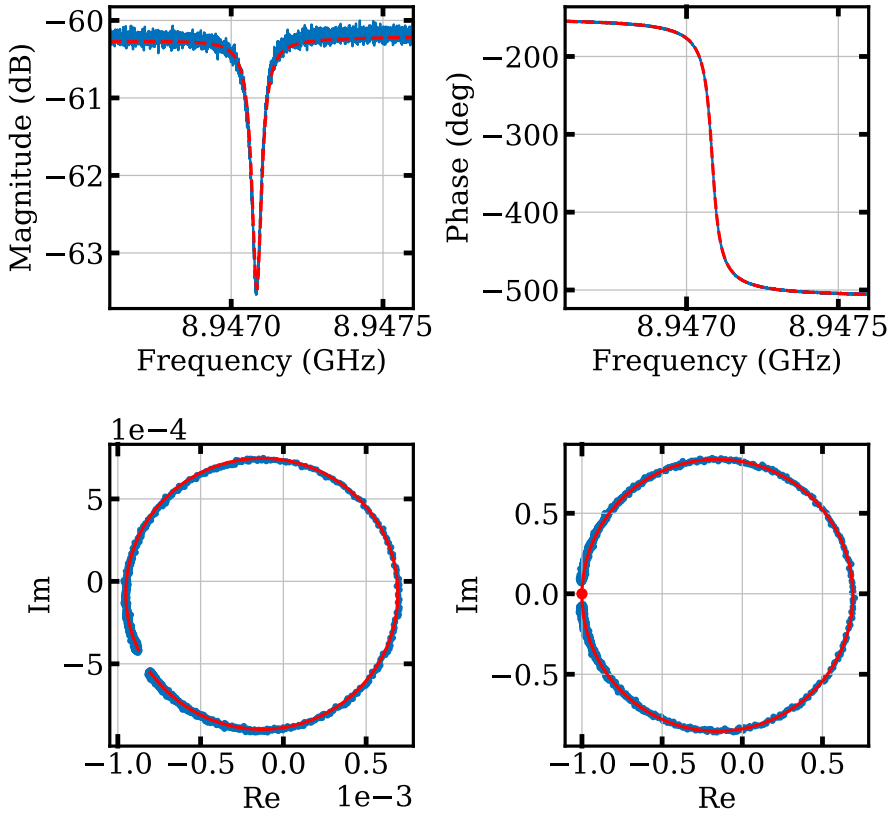

Figure 5.13: Circle fit on the cavity with hose: The top row shows the fit (red dashed line) to the magnitude and phase. The bottom row shows the fit to the circle obtained from the real and imaginary part of the reflected signal (left) and the same after normalization of the circle (right).

5.2.2 Pulses and readout signal

Generally and specially in digital quantum computation, qubit operations are performed before the readout. For this reason, good control over pulses length and timing is required. Moreover, in order to perform sequences of qubit/s operations, good phase control is required.

The signals used for the readout in the following measurements are constituted by a few photons. The white noise added by the HEMT amplifier can cover the signal. Because of the random nature of this noise, it is possible to reduce it by averaging. Averaging is performed by repeating an experiment a certain number of times and average the readout signal that is recorded by an acquisition instrument. In order to be able to perform averages two requirements are needed: the phase of the received signal must be the same (averaging signals with random phases results in zero amplitude), the repetition rate of the experiments must be large enough such that the resonator is emptied and the qubit "relaxed" to the ground state (see section 2.1.2).

In this project I use two kind of pulses: square and gaussian amplitude modulated (AM) pulses. The first one is used for the readout, so it is sent with a frequency equal or close to the cavity resonance. The second kind is used for qubit rotations and it will have a frequency equal to the qubit resonance. In order to get an AM pulse, a monochromatic microwave is multiplied by a 'shape' function. In figure 5.14, a finite square and gaussian AM pulses are shown.

The generation of a finite square pulse is usually easy. It can be obtained by switching on and off the output of a signal generator[2]. For the generation of a Gaussian AM pulse, the "shape" function is generated by an Arbitrary Waveform Generator (AWG) and it mixed with a CW signal. The gaussian pulse must have a finite length L. That means that the gaussian will be centered at $\frac{L}{2}$ and the 'tails' are cut. For the gaussian standard deviation, I have chosen a default value of $\frac{L}{6}$.

In order to record a signal, an acquisition board is used in this project. The board is sensitive to voltage and it is constitued by an Analog to Digital Converter (ADC), a buffer (memory) and a controller to manipulate data and send it to a pc. Any ADC is characterized by a sampling frequency for the time resolution and a number of bits for the amplitude resolution.

The sampling frequency is how many times per second the acquisition board records the voltage, expressed in samples/s. To understand it better, let's reference to fig. 5.15: if a disc is rotating with a given angular speed, it is possible to measure direction and speed if enough frames are available (from

[2]In order to achieve a fast switching, the "off" is actually an attenuation factor of at least 40 dB. More than sufficient for low power measurements.

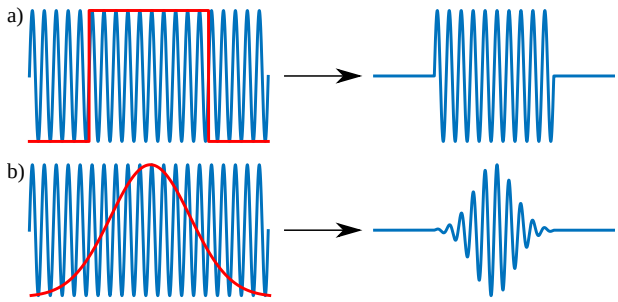

Figure 5.14: Amplitude modulation examples: **a)** Finite square pulse, used for the readout; **b)** Gaussian modulated pulse, used for qubit rotations. The sigma is here set to the total pulse length divided by 6.

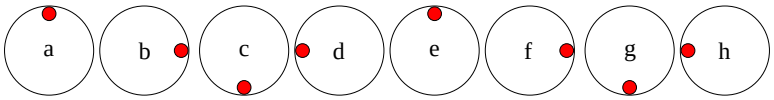

Figure 5.15: Frames of a rotating disc: If sufficient frames are available, it is possible to understand that the disc is rotating and in which direction. With less frames it becomes harder and harder to get frequency and direction of the rotation.

a to h in the example). If the sampling frequency is too slow, for example only the frames a,d,g are taken, it would look like the disc is rotating in the opposite direction compared to reality[3]. In case the sampling frequency is twice the rotation speed (frames a,c,e,...) it would be possible to understand that the disc is rotating, but direction and speed are impossible to retrieve. This last condition is called Nyquist limit, and the sampling frequency of the acquisition board must be higher than this limit in order to correctly acquire the signals of our interest. So in summary the acquisition board requires a sampling frequency larger than 2 times the signal frequency.

Now let's consider the amplitude resolution. The acquisition board will have a voltage range (sometime it is variable) that will be divided in steps given by the number of bits. The minimum step is the amplitude resolution:

$$A_{res} = \frac{V_{pp}}{2^B} \tag{5.2}$$

where V_{pp} is the peak-to-peak voltage range of the ADQ and B is the number of bits. The acquisition board I used is a SPDevices ADQ14. The board has

[3]It can actually happen to record a tire of an accelerating car and the playback will show that the tire spins in the opposite direction. This is due to the limitation of the camera sampling frequency.

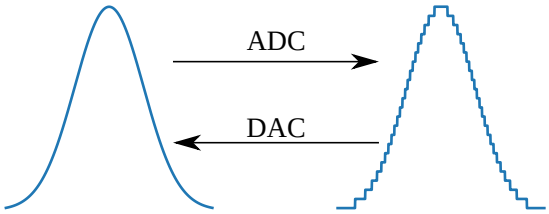

Figure 5.16: DAC and ADC example: A signal (left) is recorded after it has been digitized by an Analog to Digital converter. On the other hand, a digitized signal can be recreated by a Digital to Analog Converter.

a fixed 1.9 V_{pp} with 14-bits, resulting in a resolution of 116 μV. If a measured voltage falls between two step, the lower one is taken. An example of a signal digitization is shown in fig.5.16. The input port of the board is AC-coupled, that it is an advantage in terms of noise added by the instrument. For an AC-coupling, indeed, the low frequency noise is filtered out (up to 100 Hz for the board used), with the disadvantage that DC signals cannot be recorded.

Unfortunately it is hard to have a good amplitude and time resolution at the same time[4], for this reason, a relatively slow ADC with 1 Gsamples/s is used for this project.

Since the readout signal frequency is much higher than the ADC sampling frequency, a down-mixer must be used. The down-mixer is a device with two input ports. The local oscillator (LO) port requires a so named "pump", that is a continuous wave (CW) with a fixed amplitude and a frequency that is chosen by the user. The other input (RF) is for the signal which must be down-converted in frequency. The output of the mixer (IF) produces a signal equivalent to the input one, but with a frequency given by the difference between the input and the pump.

The down-converted signal is then filtered and amplified further before recording. The further amplification is required in order to adapt the signal to the ADC voltage range. Indeed, if the signal (including noise) would have a peak-to-peak amplitude of 10 mV, I would only use up to 7 bits of the 14 available. In order to avoid that and be limited by the resolution, amplifying the signal up to 1.9 V_{pp} is ideal.

A schematic of the setup used for the readout can be seen in fig.5.17c. If the signal produced is down-converted directly and recorded (5.17c dotted line bypass), the acquired signal is expected to be a square AM pulse with a lower frequency. This kind of detection is also called "heterodyne" because the information "travels" on two different frequencies (opposite to homodyne,

[4]It is important to understand that the indetermination of the phase of a pulse is a function of both the time and amplitude resolution of the instrument.

where the signal is down-mixed to DC). The bypass is a good way of testing the setup and the averaging. If the acquisition is repeated, the new acquired signal should overlap perfectly with the previous one in order to be able to average correctly. This can be done by choosing a time interval between experiments that is a multiple of the down-mixed period. For example, for a 50 MHz acquired signal, a repetition period of 1 ms would work.

When sending a pulse through a limited bandwidth system, like the cavity, the pulse is distorted. It will have now a finite charge and discharge time, plus a delay introduced by the longer path[5].

As already mentioned, the signal will "pick up" thermal noise at room temperature. Since the nature of this noise is random, it is possible to reduce it with averaging. The plot in fig.5.17b is obtained by recording a signal constituted by a few tens of photon at the cavity output, after averaging it 10^3 times.

After the signal is recorded, a portion is selected (between the red dotted lines in fig.5.17b) and the Fourier transform is executed on it. In fig.5.17d the magnitude of the Fourier transform (up to the Nyquist limit of 500 MHz for the ADQ used) is shown. Two times the amplitude of the peak centered at the down-converted frequency corresponds to the average amplitude of the recorded signal. In case coherent noise is present, more than one peak can appear in the Fourier transform. It is a good rule to perform this procedure also without signal and choose a down-converted frequency far from unwanted coherent noise.

If the readout setup is doubled, recording the bypassed signal and the readout one at the same time, it is possible to measure both phase and amplitude of the output signal.

5.2.3 AWG for qubit pulses

Since a transmon has more than two levels and a relatively small anharmonicity, particular care is required to avoid excitation at higher levels. As mentioned previously, the preferred pulses for qubit rotations are gaussian amplitude modulated. The reason for this choice is that the Fourier transform of a gaussian is still a gaussian, but with a standard deviation that is proportional to the reciprocal standard deviation in time-domain. For a finite square AM pulse, the Fourier transform is a $\frac{\sin(x)}{x}$ function, that has "oscillating tails" that could excite higher levels of the transmon.

[5]Cryostat lines plus room temperature cables are around L=10 m long. This will add a delay of $\frac{3L}{2c}$ =50 ns. Where it has been considered that the speed of the signal in the coaxial cables is about $\frac{2}{3}$ of the speed of light c.

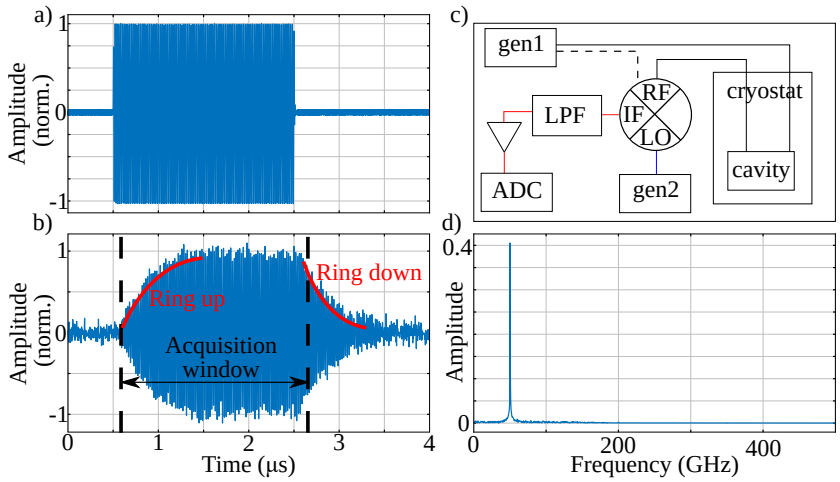

Figure 5.17: Readout scheme and example. **a)** The squared AM pulse generated at the cavity frequency, is down-converted to 50 MHz and recorded, bypassing the cryostat (dotted path in **b**). The amplitude is normalized. **b)** The same signal recorded after entering the cryostat and passing through the cavity. The signal shows an evident ring up and ring down due to the limited bandwidth of the cavity, that acts as a filter. **c)** Schematic of the setup: A signal generator gen1 sends a square AM pulse to the system. After passing through the cryostat and the cavity, the signal frequency is changed by the down-mixer. The signal generator gen2 is continuously powering the mixer with a CW signal with a frequency that is 50 MHz higher than the signal one. The new down-converted signal is filtered by a DC-80 MHz low pass filter and amplified to get a signal in the range of 1-2 V at the ADC. **d)** The acquired signal is cut in the area of interest (so named "acquisition window", limited by the black dotted vertical lines in **b**). Then a Fourier transform is executed. In this plot the Fourier transform magnitude is plotted between 0 and the Nyquist frequency of the ADQ.

Generating a gaussian AM pulse for qubit rotations is not as easy as a square AM pulse. To generate the correct modulation function an Arbitrary Waveform Generator is used. This device can produce arbitrary shaped waveforms as long as the device specifications are observed.

The qubit control requires high precision in the amplitude and the phase of the pulses. As for the digitizer board, in order to have good amplitude resolution and high sampling frequency (with respect to the signal frequency), a Digital to Analog Converter (DAC, see fig.5.16) can be used to generate low frequency signals that will be up-converted afterwards. The AWG used in my experiment has 4 channels with 14 bits of vertical resolution and a sampling frequency of 1 GSamples/s.

The device used for the up-conversion is an IQ-mixer, a 4 port device that requires a pump (LO) and two inputs I and Q. The output (RF) is, ideally, equal to:

$$RF(t) = \mathrm{I(t)}\cos(\omega_{\mathrm{LO}}\mathrm{t}) + \mathrm{Q(t)}\sin(\omega_{\mathrm{LO}}\mathrm{t}) \tag{5.3}$$

where ω_{LO} is the pump frequency, also known as carrier. In summary the pump is split in two parts inside the mixer and one side is delayed in order to have a 90 deg phase shift. Then the two pumps are multiplied for the I and Q signals and the result is combined. If constant I and Q are used, the output will be a signal with the carrier frequency. Instead, if an AC signal is sent to the two ports, the mixer output will be constituted by the sum of two new signals: the left sideband (LSB), with a frequency given by the carrier minus the signal frequency; and the right sideband (RSB), with a frequency given by the carrier plus the signal frequency. Two special cases can be realized when a cosine at a certain frequency is sent to the I port and a $\pm$sine with the same frequency is sent to the Q port. In summary

$$RF(t) = \cos(\omega_S t)\cos(\omega_{LO} t) \pm \sin(\omega_S t)\sin(\omega_{LO} t) = \cos((\omega_{LO} \mp \omega_S)t) \tag{5.4}$$

where ω_S is the signal frequency at the ports I and Q. The output will be constituted by only the LSB ($\omega_{LO} - \omega_S$) or the RSB ($\omega_{LO} + \omega_S$), resulting in the desired up-conversion of the signal without unwanted frequencies.

IQ-mixers are typically diode based and present a non-linear behavior. When the I and Q signal are close to 1 V, higher harmonics can start to appear at the output, producing sidebands at $\omega_{LO} \pm N\omega_{IQ}$, with N integer. To avoid such a problem, I decided to attenuate the AWG output with around 16 dB of attenuation and amplifying the mixer output signal by 26 dB, after filtering it with a band-pass filter. After the amplification, the signal passes through a directional coupler, where a small part of the signal (-20 dB in power) is routed to a spectrum analyzer, necessary for the IQ-mixer calibration. The calibrated

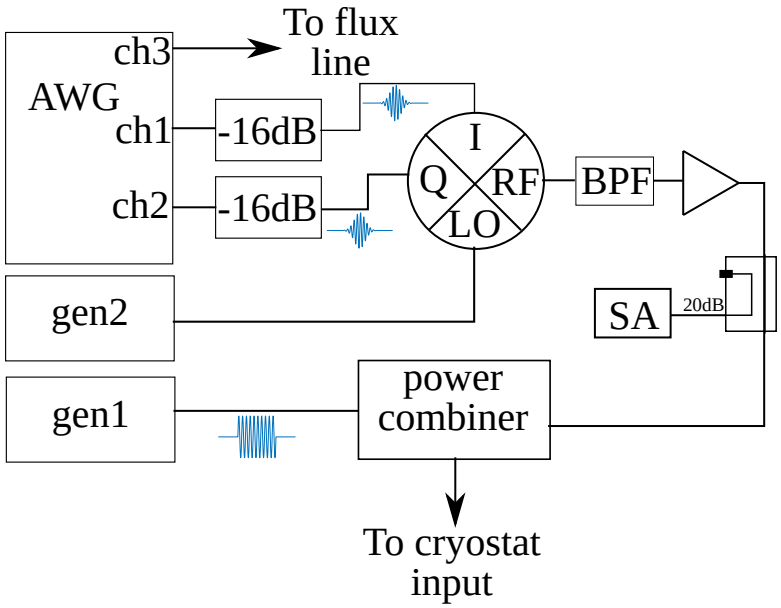

Figure 5.18: Schematic of the full setup. Two channels of the AWG are used to create gaussian AM pulses with different phase to the IQ-mixer I and Q ports. The signals are attenuated by 16 dB. A signal generator is used to provide the required LO frequency (carrier) to the mixer. The output of the mixer is filtered with a band-pass coaxial filter and then is amplified. Part of the amplified signal is routed to a spectrum analyzer (SA) through the 20 dB port of a directional coupler. Another signal generator is used to generate the square AM readout pulse. The signals are finally combined by a power combiner, with the output connected to the cryostat microwave input line. Another AWG channel is instead directly connected to the cryostat coaxial line dedicated to the coil excitation.

signal is then combined with the readout signal through a power combiner. A schematic of the full setup is shown in fig.5.18.

Unfortunately, such mixers are not perfect and there is an imbalance in the 90 deg phase delay of the pump. Also, any dc offset in the I and Q signals produces a leakage of the pump at the output.

I wrote an algorithm for the IQ-mixer calibration, that can be used to compensate the imperfections, reducing the amplitude of the unwanted sidebands. A power ratio of more than 40 dB between the signal and the other sidebands is desired.

As algorithm parameters, the user can specify the AWG frequency, amplitude and the up-mixed frequency. The uncalibrated spectrum is shown in fig. 5.19a. The LO leakage produces the carrier frequency, in the middle of the

figure. The AWG signal frequency sets the separation between the sidebands and the carrier. The user can also choose to use the left sideband (LSB) or the right one (RSB). In this example, the LSB is chosen, so the algorithm will first produce CW signals at the AWG channels[6], with a -90 deg phase difference. Then it will apply a DC offset to the I and Q channels, searching for a minimum in the carrier amplitude. Successively, it will start to modify the amplitude and phase of the Q channel, to minimize the unwanted sideband. The procedure is repeated three times. The final result is shown in fig. 5.19b. Unfortunately the calibration is amplitude and frequency dependant, so it is a good rule to calibrate for every 0.1 V and every 5 MHz. It is also good to mention that a different DC offset is required for the LO leakage when the pulse is not played (equivalent to a 0 V AC amplitude).

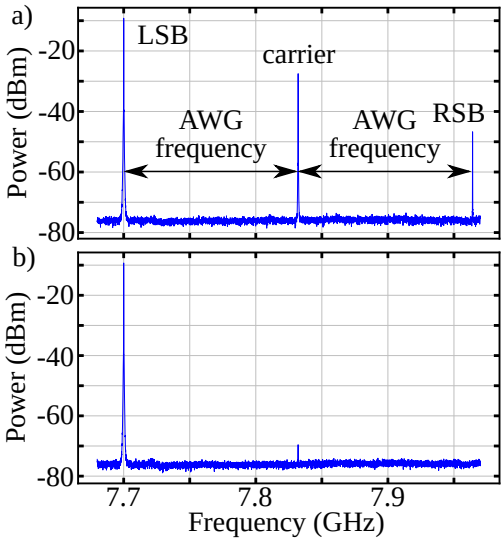

Figure 5.19: IQ-mixer calibration. **a)** The spectrum before the calibration is constituted by a carrier, equivalent to the LO frequency, and left and right sidebands (respectively LSB and RSB). The sidebands are separated from the carrier by an amount equal to the AWG signal frequency. The calibrated sideband in this example is the left one. **b)** After the calibration, the unwanted frequencies are more than 50 dB smaller than the LSB.

[6]Most of the spectrum analyzers can't detect short pulses.

Chapter 6

Measurements procedures

In this chapter I introduce the measurements procedures used for this project. I start with the cavity transmission and qubit spectroscopy, used to find the resonator and qubit frequencies.

Then qubit characterization measurements will follow, including a flux map of the qubit frequency as a function of an applied DC magnetic flux.

The final measurements are the flux-noise analysis and a "fast-flux" measurement used to quantify how fast the qubit frequency can be changed.

6.1 System check

After the cooldown I used a VNA to measure the power transmitted through the system. The measurement of the VNA can be considered CW since the pulses are much longer than the cavity and qubits lifetimes. The measurement is executed on high power (around 0 dBm at the instrument). As explained in section 2.3.6, at high power it is possible to measure the bare cavity resonance, without the frequency shift due to the coupling with the qubits. The transmitted power amplitude as a function of the frequency is shown in fig.6.1. The mode on the left corresponds to the cavity, the one on the right to the lambda/4 resonance introduced in the system by the hose.

By lowering the power, one should notice a shift in the cavity frequency. The presence of this shift is an indication of the coupling with at least one of the two qubits.

After doing this check, it is time to change the setup to the one shown in fig.5.18.

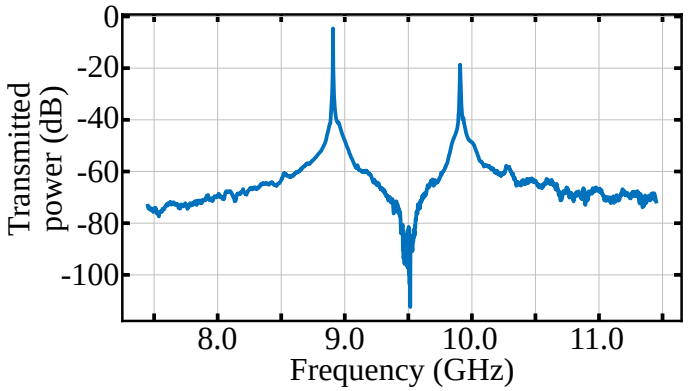

Figure 6.1: VNA measurement of the transmitted power through the cavity. The left peak corresponds to the bare cavity frequency, the right one to the resonance of the lambda/4 mode caused by the hose.

6.2 Cavity resonance measurement

In chapter 2.2.2 I explained what to expect from an amplitude or phase measurement of a CW signal passing through the cavity. For a cavity measured in transmission, the amplitude follows a Lorentzian distribution with a positive peak amplitude (the peak "points" upwards, like shown in fig.6.2).

The readout pulse I will use in all the following measurements is a square AM pulse with a length of $2\,\mu$s. The signal is then measured following the description in the previous chapter. The experiment is repeated around 400 times every 1 ms. After averaging the results, the amplitude is extracted. Then the pulse frequency is changed and everything is repeated. A Lorentzian distribution is used as a fit function with center frequency, linewidth, amplitude and offset as parameters. The measurement result can be seen in fig.6.2a. The blue dots represent the data points, and the black line the Lorentzian distribution.

If a complete population inversion is performed on one of the qubits (i.e.the qubit positioned in front of the hose), before performing the above described measurement procedure, the cavity resonance will be lower due to the dispersive shift. The result of this measurement can be seen in the fig.6.2a, represented by the red dots. The separation between the peaks is the dispersive shift χ related to the excited qubit.

In the following I fix the readout frequency at the resonance when the qubits are relaxed. So my readout amplitude will be around 16 mV when the qubits are in the ground state and to around 8 mV when the central qubit is excited.

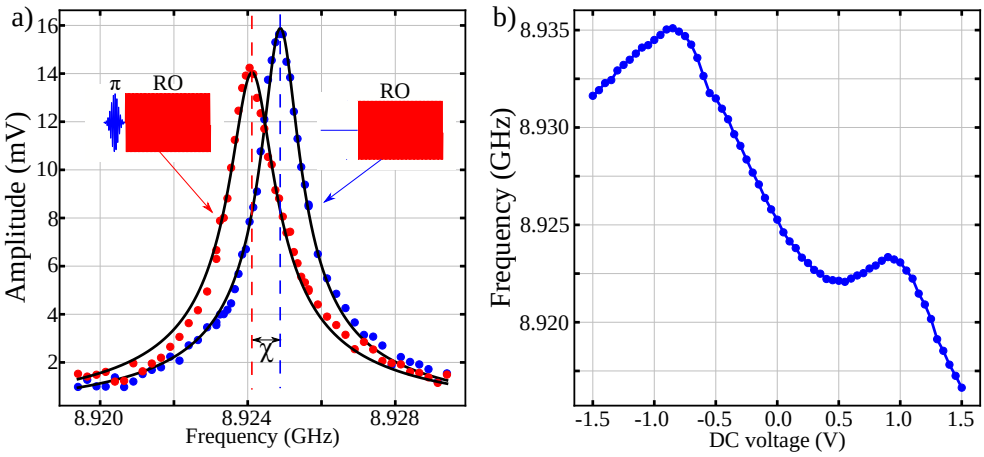

Figure 6.2: **a)** Signal transmitted through the cavity. The acquisition board is sensitive to the Voltage. Far from resonance, the signal transmitted through the cavity is low. Around the resonance the amplitude starts to be transmitted, following a Lorentzian distribution (black line). The right resonance (blue dots) is measured with just a readout pulse, and corresponds to the resonator frequency when the qubits are relaxed. The left resonance (red dots) is obtained by exciting the central qubit with a π-pulse before the readout. The separation between the two peaks is the dispersive shift χ related to the central qubit. **b)** Resonance frequency of the cavity as a function of the DC voltage applied to the coil input line. In this measurement the qubits are in the ground state.

When the qubit is prepared in a generic state, the amplitude of the averaged signal is

$$V = P_g V_g + P_e V_e \tag{6.1}$$

where V_g is the voltage one would get if the qubit is always in the ground state and V_e for the qubit in the excited state. The P_g and P_e are the probabilities to find the qubit in the ground and excited state, respectively. For example, if the qubit state is prepared in $\frac{1}{\sqrt{2}}(|0\rangle + |1\rangle)$ by a $\frac{\pi}{2}$ rotation around the x-axis of the Bloch sphere before the readout, the final voltage will be: $\frac{1}{2}(V_g + V_e)$. Given the finite temperature of the qubit, the P_g is not 100 % when the qubit is relaxed. As a consequence the measured voltage at the resonance is not equal to V_g.

Since the qubits are frequency tunable, the above mentioned resonances and χ are also frequency tunable. So the calibration of the readout frequency must be done as a function of the applied magnetic flux. To change the magnetic flux, as shown in fig.5.18, an AWG channel is connected to the coil input line. By changing this channel DC offset, the magnetic flux at the two qubits will change. The DC offset can be changed in the range [-1.5 - 1.5]V. In fig.6.2b, the resonance frequency of the cavity with the qubits in the ground state is shown as a function of the applied DC offset. This measurement is also a first indication that the hose works as intended, since the Meissner effect would repel the magnetic field otherwise.

6.3 Qubit spectroscopy and qubits flux map

After choosing the readout point, I can start to search for the qubit resonance frequency (g-e transition). The readout pulse will follow a so named "saturation pulse". A saturation pulse is a long square AM pulse (on the order of hundreds μs and with [1 - 2] times the power used for the readout pulse). By changing the frequency of such a pulse, we expect the readout amplitude to drop when one of the two qubit is excited. The continuous qubit excitation due to the long pulse brings the qubit in a superposition of the g and e state [48]. As explained in the previous chapter, the expected voltage will be close to V_g when the saturation pulse is far from the qubit resonance, and it will have a lower value when instead the qubit is excited. Ideally the measured voltage is $V = \frac{1}{2}(V_g + V_e) \approx 12\,\mathrm{mV}$.

By increasing the power, it is also possible to measure the qubit anharmonicity, as another peak appears at a lower frequency compared to the qubit resonance. This peak is due to a two photon process: two photons of the signal combine and excite the transition g-f of the transmon, where f is the third

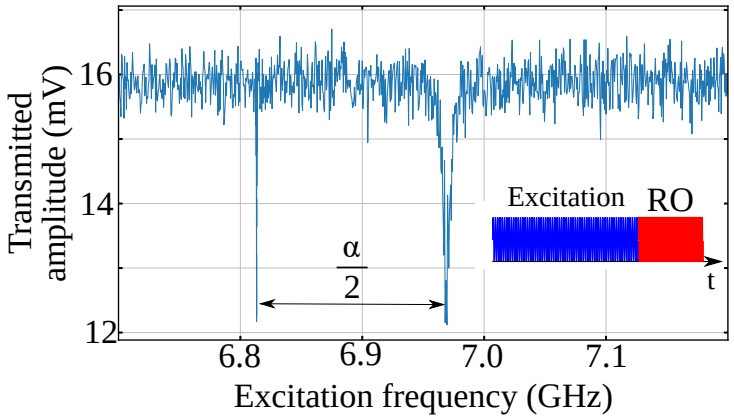

Figure 6.3: Qubit spectroscopy: The pulse sequence is shown in the lower-right, the qubit readout (Ro) follows a relatively long excitation pulse (both are squared AM pulses). The excitation frequency is changed (x-axis) at every iteration. The transmitted amplitude is constant until the excitation frequency matches the qubit one. The data follows a Lorentzian distribution. With enough power, the anharmonicity peak (two photon process) can be seen, at lower frequencies. The distance between the two peaks corresponds to half of the anharmonicity.

energy level. Since a two photon process is a rare event, not only an increase of the excitation power is needed, but also an increase of the frequency sweep step is also necessary as this peak will be relatively narrower.

A qubit spectroscopy example with the qubit resonance and the anharmonicity peak is shown in fig.6.3. Two times the distance between the peaks corresponds to the qubit anharmonicity $\alpha = -E_C$.

6.4 Qubit DC flux map

In fig. 6.4 the qubit spectroscopy for both qubits as a function of the magnetic flux is shown. The formula 2.48 is used to fit the data where the E_C value is fixed, measured with the previous method.

The summary of the parameters for both qubits are the following:

Q1 Parameters	Value	Error
E_{Jmax} (GHz)	28.58	0.05
E_C (MHz)	249.6	0.3
d	0.607	0.001
Φ_0/Volt	0.5832	0.0007

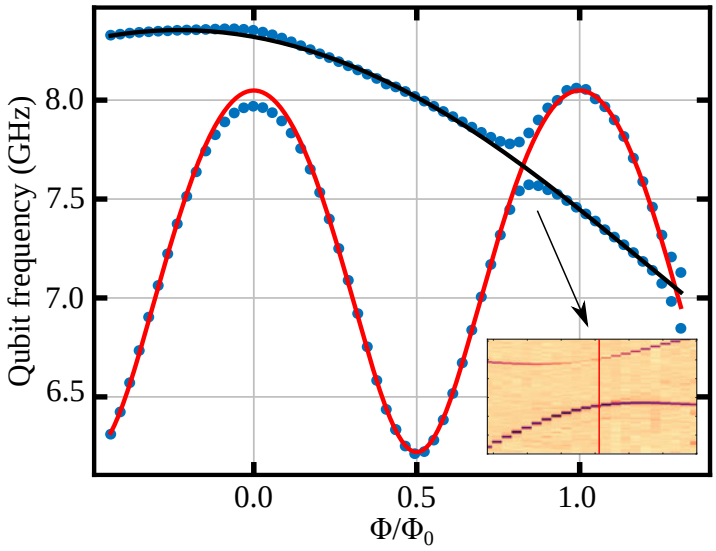

Figure 6.4: Qubits frequency flux map: the blue dots represent the experimental data and the continuous lines are fits to the data. Error bars are smaller than the point size. The red line is a fit to the qubit in front of the hose and shows that it is 5 times more tunable than the other qubit (black line). The regions where the fit lines are diverging from the experimental data are avoided crossings. A zoom of one of the avoided crossings is shown in the inset, with a splitting of about 240 MHz. The red line in the inset shows the point where the gap is smaller.

Q2 Parameters	Value	Error
E_{Jmax} (GHz)	25.0	0.2
E_C (MHz)	259.1	0.1
d	0.60	0.02
Φ_0/Volt	0.128	0.004

The last value in the tables is a calibration factor that translates the applied voltage in units of flux quanta. The ratio between this calibration factor for both qubits returns the flux cross-talk. The flux cross-talk of around 22 % is close to the value obtained with the simulation (see section 3.1). This value is, for this particular magnetic hose design, larger than for typical 2D flux-bias lines [49]. Flux cross-talk can be reduced using appropriate flux decoupling sequences [50] or by using an optimised smaller hose design with a funnel-shaped tip and optimising the qubits placement.

It is also possible to do another comparison with the simulations: 0.5 V into 50 Ω provides 1 mA at the coil because of the power attenuation of 20 dB at the 4 K stage on the flux line. According to the simulations, the field at

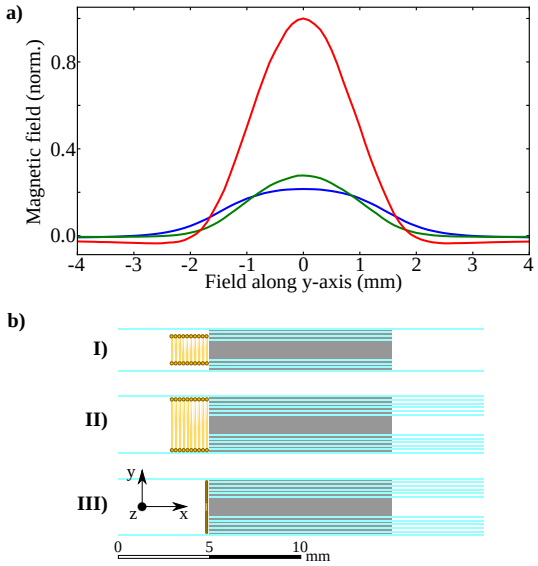

Figure 6.5: Various hose and coil designs. **a)** Simulated magnetic field intensity in x-direction along the y-axis at a distance of 1 mm from the hose for three different hose and coil designs attached to the 3D cavity. **b)** Sketches of the different designs. The blue line in **a)** represents the very first hose design **I**. The green line considers the hose with higher layer density and elongated shells as shown in the main paper but in combination with a big coil where the outer diameter matches the outermost superconducting shells inner diameter (design **II**). Finally, in red, the maximum improvement is achieved by the current design **III**, where both the hose and the coil are optimised.

the qubit center, when this amount of current excites the coil, is 22.4 nT. Given the SQUID area of 50x50 μm^2, this corresponds to 0.027 Φ_0. From the measurements, however, 0.5 V at the generator provides 0.29 Φ_0 at the central qubit, a factor of ten higher then the simulations. The reason of such discrepancy is still unclear. Since hose and coils are handmade and all the setup is assembled by hand, it is easy to get some of the parameters wrong (like distances, angles, etc.). A factor of ten in favor can be astonishing, however the hose improvements have been scaled up from previous attempts following the simulations, as illustrated in fig.6.5. For this reason, I suppose that relative fields are accurate, but absolute values are affected by an offset.

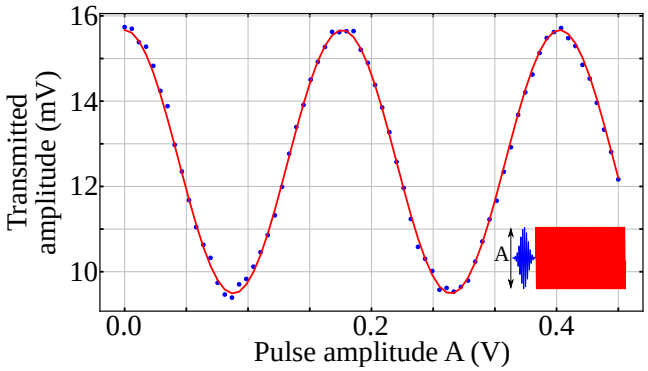

Figure 6.6: Amplitude Rabi experiment: A gaussian AM pulse is sent to the system with a frequency equal to the qubit resonance. The pulse is immediately followed by the readout. The output of the pulse is changed and the readout amplitude is plotted as a function of it. By fitting a cosine to the data, the amplitude needed for a π-pulse can be determined.

6.5 Rabi experiment

The idea of a Rabi experiment is to control the qubit population as a function of the pulse area. The pulse area is proportional to the pulse length and its amplitude. For practical reasons I usually prefer to fix the puse length and fix the gaussian sigma to one sixth of it, and vary the output voltage (so called "amplitude Rabi" experiment).

In chapter 2.1.1 I explained qubit rotations in presence of a drive. The Hamiltonian of a qubit coupled to a drive (2.11) $H_R = H_Q + H_D$ can be written in the qubit rotating frame as:

$$\hat{H}_R = \frac{\hbar A s(t) \Omega}{2} \hat{\sigma}_x. \tag{6.2}$$

where Ω is the coupling between the qubit and the drive, s(t) is a gaussian amplitude modulated pulse and A is the amplitude of the pulse s(t).

By increasing A, a qubit rotation around the x-axis is performed. As explained in section 6.2, by increasing A the expected measured voltage oscillates between 16 mV and 8 mV.

In figure 6.6 an example of an amplitude Rabi experiment with $\omega_q = \omega_D$ is shown. This result can also be used as a calibration for π-pulses and $\frac{\pi}{2}$-pulses, used in the next sections. A π-pulse is used to exchange the population of the ground state with the excited state, whereas the $\frac{\pi}{2}$-pulse is used to bring the qubit at the equator of the Bloch sphere.

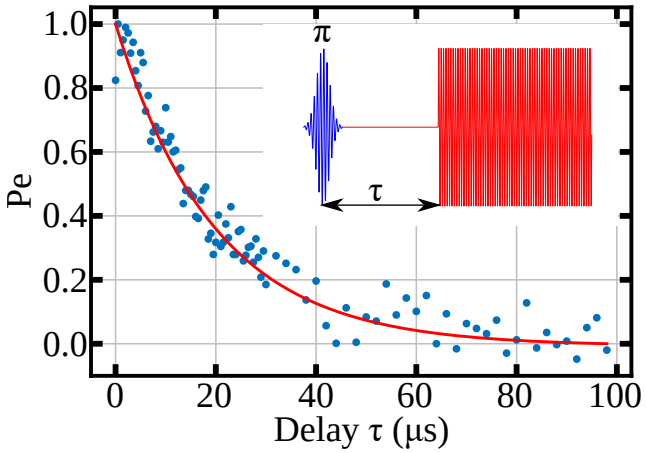

Figure 6.7: Qubit decay time measurement: A π-pulse is sent to the system to bring the qubit in the excited state. The readout is performed after a variable time delay τ. The probability of finding the qubit in the excited state versus the delay can be fit with an exponential decay (red line) which decay constant is T_1.

6.6 T1 measurement

To perform a measurement of the qubit lifetime T1, a sequence constituted by a π-pulse and a variable waiting time before the readout is used. The result and the sequence are shown in fig.6.7. An exponential decay time is extracted from a fit to the data and this value corresponds to T_1.

In fig.6.11a the T_1 is shown as a function of the central qubit frequency. It ranges from (3.6$\pm$0.4) μs at the high sweet spot up to (57$\pm$8) μs towards low frequencies. The cause of this limitation of T_1 as a function of the frequency is due to intrinsic losses of the substrate and the qubit itself. Indeed, since for a qubit $Q = \omega_q T_1$, if Q is constant, then T_1 is inversely proportional to the frequency. At high frequencies, the qubit lifetime is also affected by the Purcell effect.

6.7 Qubit temperature

In chapter 2.1.2 I explained that a transmon coupled to a thermal bath spontaneously decays to the ground state after a time longer than T_1. However, the heating rate is not exactly zero, but it is a function of the bath temperature (equation 2.13). One can expect that the qubit can be found in the excited state even though no pulses have been applied. It is then possible that the

outcome of a qubit rotation is wrong due to wrong qubit initialization.

By measuring the probability of finding the qubit in the ground state P_g and the excited state P_e it is possible to estimate the qubit temperature.

Before proceeding with this measurement it is important to remember that the transmon has more than two energy levels and there is a probability to populate higher ones. In the following I will use the convention of calling g and e the first two levels of the transmon, as it has been done previously, and f the third energy level. I also want to remind that the energy gap between g and e is equivalent to the qubit frequency, and the energy between the levels e and f is instead reduced by the anharmonicity.

The qubit temperature and the population distribution in the transmon energy levels are related through the Bose-Einstein distribution. For sake of simplicity, since we expect the qubit to be cold enough, I make the assumption that the probability of finding a qubit in thermal equilibrium with the bath in the f-state (P_f) is zero and I also use a Boltzmann distribution. In this case it follows that

$$P_g + P_e = 1. \tag{6.3}$$

A readout voltage is always a function of the populated levels, and in the following experiment the formula 6.1 must be extended by defining an additional V_f, that would be the voltage measured if the qubit population would be all in the f state.

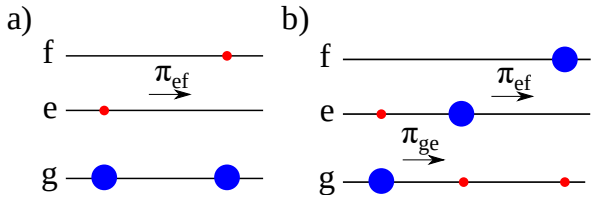

Figure 6.8: Qubit population measurement scheme. The probability of finding a qubit in the ground state is not 100 % due to the qubit temperature being higher than 0 K. **a)** On the left the initial state of the qubit, with most of the population (blue dot) in the g-level (ground) and some in the e-level (red dot).For these experiments I assume that there is no population in the f state, which is an approximation. A π_{ef}-pulse between the e and f levels shifts the e-population to the f-level. **b)** The same experiment is executed after a population inversion between the g and e level. The readout amplitude outcome after averaging changes as a function of these cases.

By referring to the scheme in fig. 6.8a and looking at the results shown in fig.6.9, if a Rabi experiment is performed between the levels e and f, the

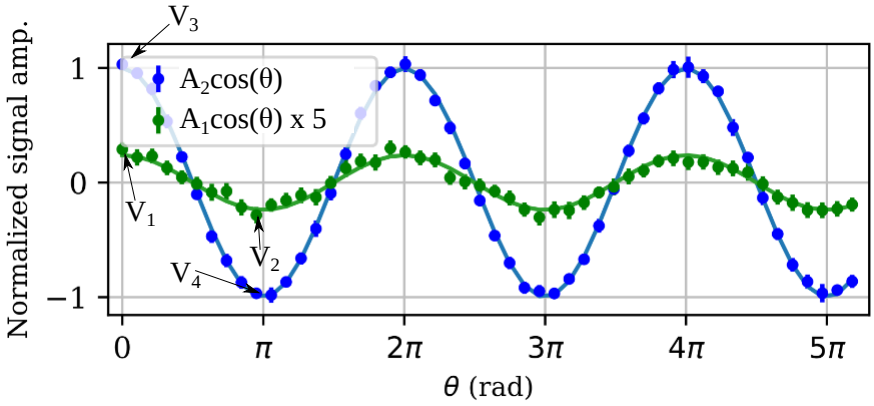

Figure 6.9: Rabi experiments for population measurements. In green a Rabi experiment performed between the e and f energy levels. The amplitude has been multiplied by a factor of 5. In blue a Rabi experiment performed between the e and f energy levels after a population inversion between the g and e levels.

voltage at the begin of the experiment and at every 2π rotation is given by

$$V_1 = P_g V_g + P_e V_e \tag{6.4}$$

and the voltage corresponding to a full population inversion between e and f (π_{ef}) is instead

$$V_2 = P_e V_f + P_g V_g. \tag{6.5}$$

So the full Rabi amplitude between the levels e and f is

$$A_1 = |V_2 - V_1| = P_e |V_e - V_f| \tag{6.6}$$

Another measurement is needed, this time the scheme presented in fig. 6.8b is followed. After a π_{ge}-pulse the readout would be:

$$V_3 = P_e V_g + P_g V_e \tag{6.7}$$

If now a Rabi between the levels e and f is performed again, the voltage level corresponding to a π_{ef} is now:

$$V_4 = P_e V_g + P_g V_f \tag{6.8}$$

resulting in an amplitude difference:

$$A_2 = |V_3 - V_4| = P_g |V_e - V_f| \tag{6.9}$$

So in summary I perform a Rabi between the level e and f and fit a cosine to the data (blue line in fig.6.9) to get A_1. Then I do the same with a π_{ge}-pulse before the same Rabi experiment (green line in fig.6.9) to get A_2. The ratio between these two amplitude is equal to the ratio between P_e and P_g. Together with the normalization 6.3 one can evaluate P_e.

It is worth to underline that, the colder the qubit, the lower is P_e and the lower the resulting amplitude A_1. Performing this measurement requires more averaging than usual.

The temperature is calculated by reverting the Boltzmann equation, and the values I found for several experiments is in the range of 60 - 80 mK. This range of temperatures is compatible with the estimation discussed in section 5.2.1.

6.8 Qubit dephasing measurements

Before characterizing the qubit dephasing and in particular the flux noise, I want to introduce the Ramsey and Echo experiments.

The Ramsey experiment consists of a sequence of two $\frac{\pi}{2}$-pulses followed, by a qubit state readout. The delay between the two $\frac{\pi}{2}$-pulses is varied and the qubit state is measured and recorded. The first $\frac{\pi}{2}$-pulse rotates the qubit from the ground to the equator of the Bloch-sphere where the qubit state will then evolve over time with an angular frequency equal to the qubit resonance frequency. One can move to the qubit rotating frame and then the qubit state will be stationary.

If the drive frequency is equal to the qubit resonance frequency, the second $\frac{\pi}{2}$-pulse will bring the qubit state to the excited state. If instead there is a non-zero detuning Δ between the drive frequency and the qubit frequency, as a function of the time τ between the two pulses there will be a phase evolution. When $\Delta\tau = 2\pi N$, with N integer, the second $\frac{\pi}{2}$-pulse will bring the qubit to the e-state, when $\Delta\tau = \pi N$, with N integer, the second $\frac{\pi}{2}$-pulse will bring the qubit back to the g-state instead. All other situations fall in between, so in a Ramsey experiment with a constantly detuned drive, we expect to measure oscillations between g and e, similar to a Rabi experiment.

It is possible to drive the qubit off-resonance and see oscillations appear in the measurement, together with the exponential decay. But the way I prefer is to drive in resonance and change the phase of the second $\frac{\pi}{2}$-pulse by an amount proportional to the delay

$$\varphi_2 = \frac{2\pi}{\text{oscillation period}}\text{delay}. \tag{6.10}$$

In this way the oscillation period is known and can be set slow enough to be recorded by the limited sampling frequency. Alternatively it can be further slowed down to reduce the number of points needed for the measurement (and so the measurement time). The effective oscillation period in a Ramsey experiment is extracted from a fit to the data and it is compared to the one created by the phase shift. The difference can be used to tune the drive frequency such that is equal to the qubit one which includes the stark shift due to pulse driving.

Noise can perturb randomly the qubit frequency, as a consequence there will be a random phase between the qubit frequency and the drive frequency during the free evolution τ. The consequence of the noise is to cause the amplitude of the oscillations to decay exponentially with a decay constant equal to T_2^*. Since the T_2^* has an upper limit equal to $2T_1$, the Ramsey experiment can be used to evaluate the dephasing due to noise by using formula 2.14.

Another similar measurement is a T_{Echo} [51] experiment, that consists of adding a π-pulse in the middle of the Ramsey sequence. This kind of sequence is less affected by pink noise and it can be used to separate the dephasing due to high-frequency noise which is not filtered by the Echo sequence from the low-frequency one. An example of a T_{Echo} measurement is shown in fig. 6.10.

In this project the qubit frequency can be changed with the injection of a magnetic flux through the SQUID loop. However, in this way the qubit frequency is also affected by flux noise and so it is affected by a further dephasing mechanism. The flux noise has a 1/f dependency and contributes quadratically to the dephasing rate [51, 52].

An analysis of the T_1, T_2^* and T_{Echo} versus the flux is shown in fig.6.11. The x-axis has been chosen such that at 0 flux the central qubit is in the high sweet spot (maximum frequency), and at $0.5\,\Phi_0$ it is in the low sweet spot. Plots **b** and **c** show how the qubit coherence is higher in the two sweet spots, where the qubit is almost unaffected by the flux noise.

The plots **d** and **e** give an indication of the amount of dephasing in the system. The high sweet spot has a better coherence, but only because it is limited by its short lifetime. This happens when, looking at the formula 2.14, the first term $\frac{1}{2T_1}$ is much larger than Γ_φ.

The last plot **f** shows the improvement given by the T_{Echo} filtering compared to a Ramsey experiment. It shows that the improvement is maximum between the sweet spots (slopes), where the qubit is more sensitive to magnetic flux.

As mentioned previously, the dispersive shift can cause dephasing. If I assume that the cavity is relatively warm, residual thermal photon can dephase the qubits. This kind of noise is high-frequency, so the dephasing measured

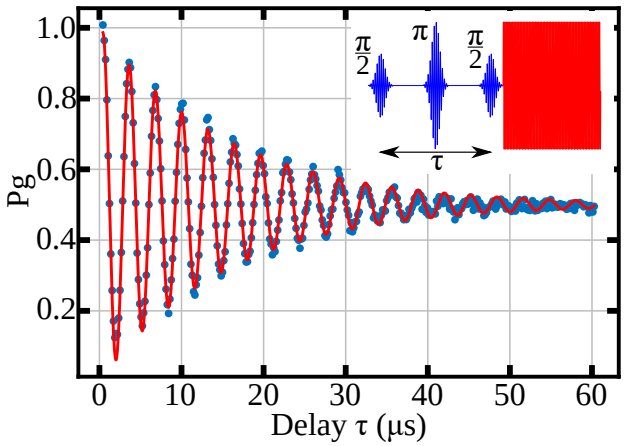

Figure 6.10: TEcho sequence. A Ramsey experiment is constituted only by two $\frac{\pi}{2}$-pulses, while a TEcho experiment has an additional π-pulse in the middle (upper-right in the plot), to overcome slow fluctuations due to pink noise. In this plot an oscillation of $3.2\,\mu$s has been forced by changing the phase of the last pulse. The delay τ is the distance between the first and last pulse.

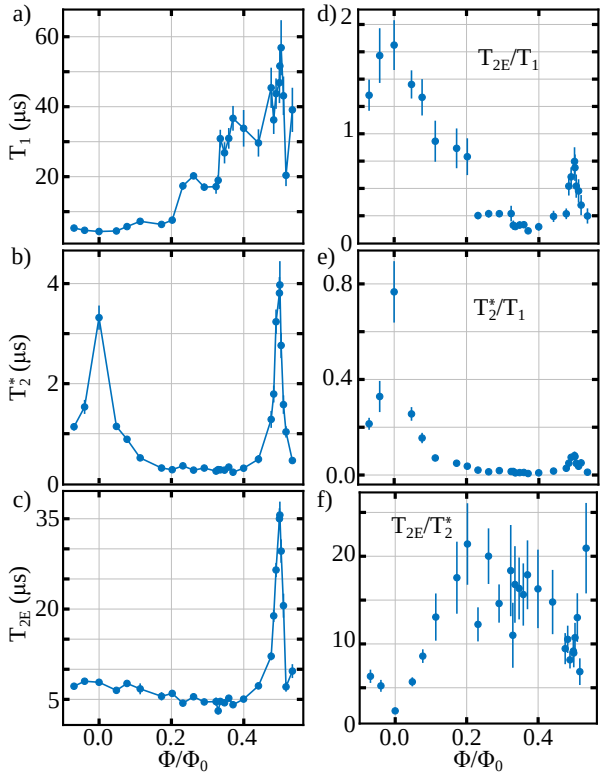

Figure 6.11: Decay and coherence times of the central qubit. **a - c)** T_1, T_2^* and T_{2E} as function of the flux. **d - f)** ratio of T_{2E}/T_1, T_2^*/T_1 and T_{2E}/T_2^*.

by a T_{Echo} experiment is ideal to characterize this noise. After evaluating the Echo dephasing Γ_E at the sweet spot, obtained by reverting the formula 2.14, it is possible to use the formula 2.68 to get an estimation of the residual photon n_{th}. This evaluation results in $n_{th} = 0.033 \pm 0.004$, compatible with a cavity temperature around 130 mK. This number is in good agreement with the temperature evaluation in chapter 5.1.2.

6.9 Flux noise analysis

To measure the actual flux noise that is affecting the qubit, first we need to take the derivative of the flux map (fig.6.4) to get the qubit flux sensitivity as a function of the applied flux or frequency of the qubit. Then the dephasing Γ_φ^R must be extracted by inverting the formula 2.14 and inserting the values for T_2^* and T_1. The same is done with T_{Echo} and T_1, to get Γ_φ^E. According to ref. [52], the dephasing is proportional to the sensitivity, through the formula

$$\Gamma_\Phi^{E/R}(\Phi_b) = (A_\Phi \eta_{E/R})^{(1/2)} \left| \frac{\partial \omega_{01}}{\partial \Phi} \right|. \tag{6.11}$$

Where A_Φ is the flux noise that influence the qubit dephasing and $\eta_{E/R}$ is a coefficient, called efficiency, that is different for the Ramsey and the Echo sequences.

In figure 6.12a, the dephasing from a Ramsey experiment is compared to the qubit sensitivity. The plot shows that the rate follows the sensitivity to the flux noise. Then the two curves are divided to see if the flux noise varies across the flux map. The area around the sweet spots, not sensitive to magnetic flux at the first order, is not considered. The result is roughly constant and is shown in figure 6.12b. The same is done for the Echo sequence, resulting in the plots 6.12c and d.

According to the theory, the efficiency coefficient for the Ramsey is a function of two values that depends on the experiments repetition rates and the total length of the sequence (pulses length and delay). The efficiency of the Echo sequence is constant and equal to $\eta_E = ln(2)$.

Finally, from the average of plot 6.12d and the constant efficiency, I extract the flux noise amplitude:

$$A_\Phi = ((7 \pm 3)\mu\Phi_0)^2 \tag{6.12}$$

This value is slightly larger than the typically observed flux noise of $\approx 1\,\mu\Phi_0$ [52, 51] most likely due to the larger than typical flux loop size of 50x50 μm^2.

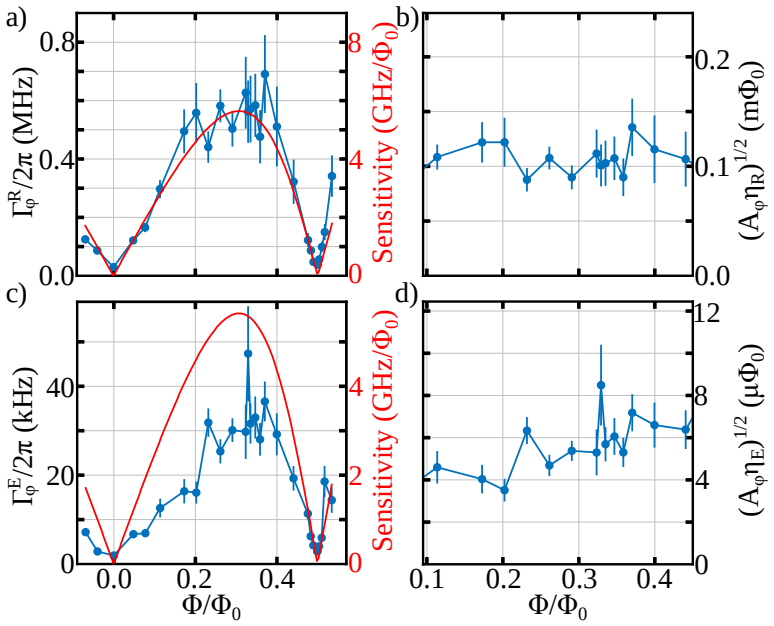

Figure 6.12: Flux sensitivity and dephasing rates: **a)** Dephasing rate measured through Ramsey experiments for different points of the flux map (blue). The sensitivity of the qubit to flux computed from the flux map is shown in red. **b)** Ratio of the Ramsey dephasing rate and the qubit flux sensitivity shown in plot a). We only plot the values between 0.1 and 0.45 Φ_0 to avoid problems with the vanishing flux sensitivity at the sweetspot. **c)** Same plot as a), but the dephasing rate is obtained from an Echo measurement. **d)** Ratio between the Echo dephasing rate and the flux noise sensitivity shown in plot c)

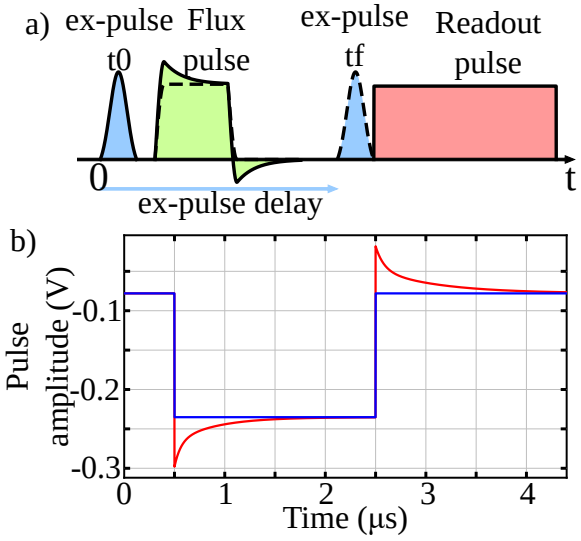

Figure 6.13: **a)** Pulses sequence. The flux pulse and the readout are fixed on the time axis. The excitation pulse (guassian AM pulse) starts at the origin and then it is delayed until it is close to the readout pulse, passing through the flux pulse. The frequency of the excitation pulse is also changed for each time step. **b)** Flux pulse shape. In a fist experiment a square flux pulse (in blue) is used. The pulse starts at 500 ns and stops at 2.5 μs. In a second experiment, a more complicated shape (in red) is used to speed up the qubit frequency response to the flux variation.

6.10 Fast-flux measurement

In order to assess the fast flux capabilities of the system, I perform another experiment with the aim to measure the qubit frequency when it is changing on short time scales. The flux pulse I use in this experiment is provided by an AWG channel, connected to the coil through the coil input line. The AWG channel excites the coil with a voltage

$$V(t) = V_{\mathrm{AC}} * f(t) + V_{\mathrm{DC}} \tag{6.13}$$

where V_{DC} is an offset, used to set the initial qubit frequency, V_{AC} represents the pulse amplitude and $f(t)$ is a function normalized in the range [0 - 1] that provides the pulse shape. Practically the V_{AC} sets how much the qubit frequency will change (how high the "jump" is) and $f(t)$ sets the way it will change.

A simple case is a square flux pulse, that is equal to 1 in a range $[t_0, t_1]$ and zero elsewhere. In a first experiment I choose a square pulse with $t_0 = 500$ ns

and $t_1 = 2500\,\text{ns}$. The pulse is depicted in figure 6.13b, in blue, and as a dotted line in figure 6.13a, together with the full sequence. The idea behind the sequence used is to perform a qubit spectroscopy 6.3, but this time with a gaussian AM pulse. After each frequency sweep for the spectroscopy the pulse is delayed, getting closer to the readout one, that is fixed on the time axis at $4.1\,\mu\text{s}$. After increasing the delay, the spectroscopy is repeated. In this way the excitation pulse can be used to find the qubit frequency in areas where the flux is stable (constant) and where it is changing (slopes).

The excitation pulse length is a trade-off between a fast rotation and a good frequency resolution (they are inversely proportional). It is a 100 ns long gaussian pulse, with a sigma that is one sixth of the total length. The result of a qubit spectroscopy with such a pulse results in a gaussian distribution centered at the qubit frequency and with a linewidth given by the Fourier transform. This result is shown in figure 6.14a, where it has been executed in an area where the flux was stable, so when the delay is less than 500 ns. In 6.14b, instead, the delay is equal to 500 ns, a critical point, on the slope of the flux pulse. Here the qubit resonance frequency is still visible, but the linewidth is now larger due to the qubit changing its frequency during the experiment.

After repeating the experiment for several delay steps and frequency steps, the qubit frequency as a function of the applied flux is obtained. The data is first represented on a map, with the delay of the excitation pulse on the x-axis and the excitation frequency on the y-axis. At each point of the map, the transmitted amplitude is recorded. The full map is shown figure 6.15a. As in the previous experiments, when the transmitted signal amplitude is high (in orange in the figure), the qubit is in the ground state, otherwise (dark colours) it is excited.

The measurement is divided in 5 sections, following the flux pulse. In each section the amplitude of the excitation is adjusted to be sure that the qubit is mostly in the excited state when the drive frequency is close to the qubit resonance frequency. Also the point density of the excitation frequency and delay sweeps is adjusted where the qubit frequency variation is fast.

The qubit frequency is extracted and represented in figure 6.15b. The qubit frequency variation to a square flux pulse (6.13b, in blue) is represented by the blue dots.

Following reference [53], the qubit frequency response can be approximated with a double exponential function of the form:

$$y(t) = A(e^{-\frac{t}{\tau_1}} + e^{-\frac{t}{\tau_2}}) \tag{6.14}$$

By fitting $y(t)$ to the data in blue, I get the following decay times: $\tau_1 = (25\pm2)\,\text{ns}$ and $\tau_2 = (231\pm10)\,\text{ns}$.

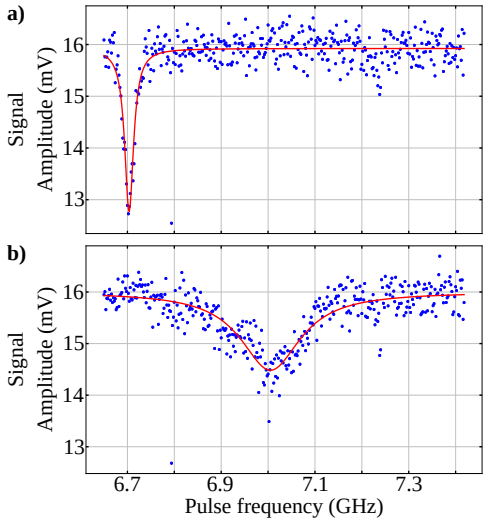

Figure 6.14: Two results examples of the sequence shown in fig.6.13. **a)** Region where the magnetic flux is constant shows a Gaussian distribution of the data points, with the width equal to the Fourier width of the excitation pulse. **b)** Region where the magnetic flux is changing, the Gaussian is wider and has less amplitude as the frequency of the qubit is changing during the excitation pulse.

In a second experiment I follow the second method proposed in the supplementary material of reference [53] with the aim of speeding up the qubit frequency response. The flux pulse is changed to

$$V(t) = V_{\mathrm{AC}} * f(t) + V_{\mathrm{DC}} + OS * g(t) \tag{6.15}$$

where OS is an overshoot value and g(t) is a reverted double exponential function. This pulse is shown in figure 6.13a (in red). The qubit frequency response is represented in 6.15b, also in red. The change in the qubit resonance frequency now occurs with an initial rise time τ_1 of (14.1 ± 0.3) ns and a slower tail τ_2 of (100 ± 2) ns. The frequency of the qubit remains stable 500 ns after the jump, with frequency fluctuation of less than 600 kHz.

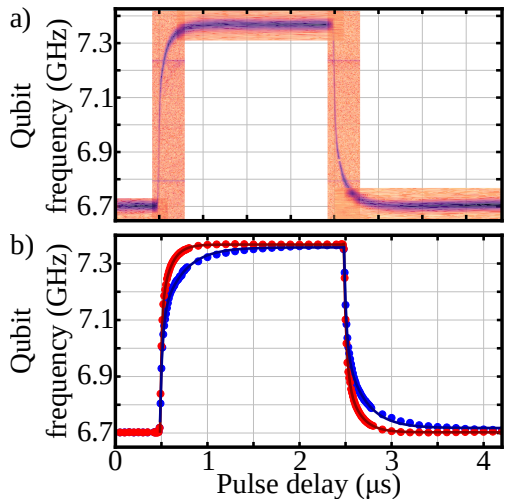

Figure 6.15: Measurements of the qubit frequency tunability with a fast varying magnetic field. **(a)** After applying the sequence shown in fig.6.13a, the qubit frequency is measured. The bright color corresponds to the qubit in the ground state and dark color to the qubit in the excited state.**(b)** This measurement shows a qubit resonance frequency variation of around 600 MHz. Dots represent the response of the qubit frequency to a 2 μs square pulse (blue) and a pulse shaped with a double exponential amplitude (red). These pulses are shown in Fig.6.13b with the same colors as the acquired data. Dark lines represent the fit to the data, executed with a double exponential function, as mentioned in the main text. Frequency fluctuations are in the order of 600 kHz.

Chapter 7

Conclusions

In this thesis I have first given the motivations for the realization of an analog quantum simulator that could simulate the behavior of several spin-systems, like a 2D spin ladder in a dimer phase. I also explained the advantage of using 3D superconducting transmons, to avoid complications like wiring and non uniformity in the qubit fabrication process.

Specifically I addressed, within this project, the readout problem of such AQS. I solved the magnetic flux injection problem in 3D structures through the use of a magnetic hose, modified to work with AC fields and SC cavities/waveguides.

The 3D waveguide cavity has been modified such that, together with the hose designed to act as a filter for high frequency microwave photons, preserves the internal quality factor up to the order of 10^6. A result better than similar experiments performed with static magnetic fields [40, 41].

The magnetic flux that reaches the central qubit is more than sufficient to change its frequency for more than a full period, but the flux noise analysis suggests that the SQUID loop could be too big. A reduction of the SQUID loop would improve the flux noise. To be able to maintain at least one full period of frequency tunability while reducing the SQUID loop, the hose and coil must improved further. Alternatively, using dedicated flux lines for the coil excitation can also be done. Avoiding the 20 dB attenuation at the second cryostat plate would allow to excite the coil with more current without destabilizing the cryostat. The AWG amplitude would be sufficient to provide the flux pulse, but probably a separated DC bias would be needed.

The flux coupling between the two qubits also need some improvement. However, it must be said that the hose and coil are hand made and they result in a relatively large hose. Building smaller hoses, together with a better qubits positioning should greatly improve the flux cross-talk. Despite 2D architectures being better in this remark, I want to emphasise that they could benefit

from applying the magnetic hose in order to circumvent complicated wiring schemes.

The final analysis about the flux injection speed has also shown pretty good results, with timings on the order of hundreds nanoseconds. A further improvement can be achieved by putting more effort in the pulse pre-shaping, like suggested in the supplementary material of reference [53].

The results of this project have been published [54] after several improvements from a first version (introduced in appendix). The magnetic hose idea would be suited to individually control qubits in superconducting circuits architectures like [26, 55, 56] without compromising coherence times. Moreover, due to the ability to apply time varying signals, one could also use the hose to drive parametric amplifiers [57, 58] or tunable couplers [50].

Appendix A

Qubit frequency stability over time

In this chapter I want to share the results of a test performed on a system constituted by a single JJ based qubit and a copper cavity (without hose and coils). The test consists in monitoring the T_1 and T_2^* times over a large time span.

As explained in chapter 6 for a decay time and a Ramsey measurement, a delay τ is used in the sequence. For a T_1 measurement, the delay is inserted between the end of the π-pulse and the begin of the readout. For a T_2^*, the delay is instead placed between the end of the first $\frac{\pi}{2}$-pulse and the begin of the second one[1].

For the measurement, a N-points array of delays $\tau_i^{(1)}$ is prepared for a decay measurement and another N-points array of delays $\tau_i^{(2*)}$ for a Ramsey experiment. For each index value $i = 1, 2, ..., N$, first a decay measurement sequence with delay $\tau_i^{(1)}$ is sent to the system, and repeated several times in order to perform averages on the readout signal. After averaging, the amplitude of the transmitted signal is recorded. Then, a Ramsey sequence with delay $\tau_i^{(2*)}$ is performed and repeated several times for averaging. After this Ramsey data point, the index is increased and everything is repeated for the new delay values. In summary I am recording the results of two intertwined decay and Ramsey experiments with the same number of points N.

The number of averages and the number of delay points N are chosen as a trade-off between measurement speed and quality (that determines the T_1 and T_2^* values precision). I repeated these measurements every 10 minutes (each measurement requires 5 min) for over 30 hours during the weekend. The result

[1]The delay definitions used are only for the algorithm and instruments. In literature the delay it is often defined between the $\frac{\pi}{2}$-pulses centers.

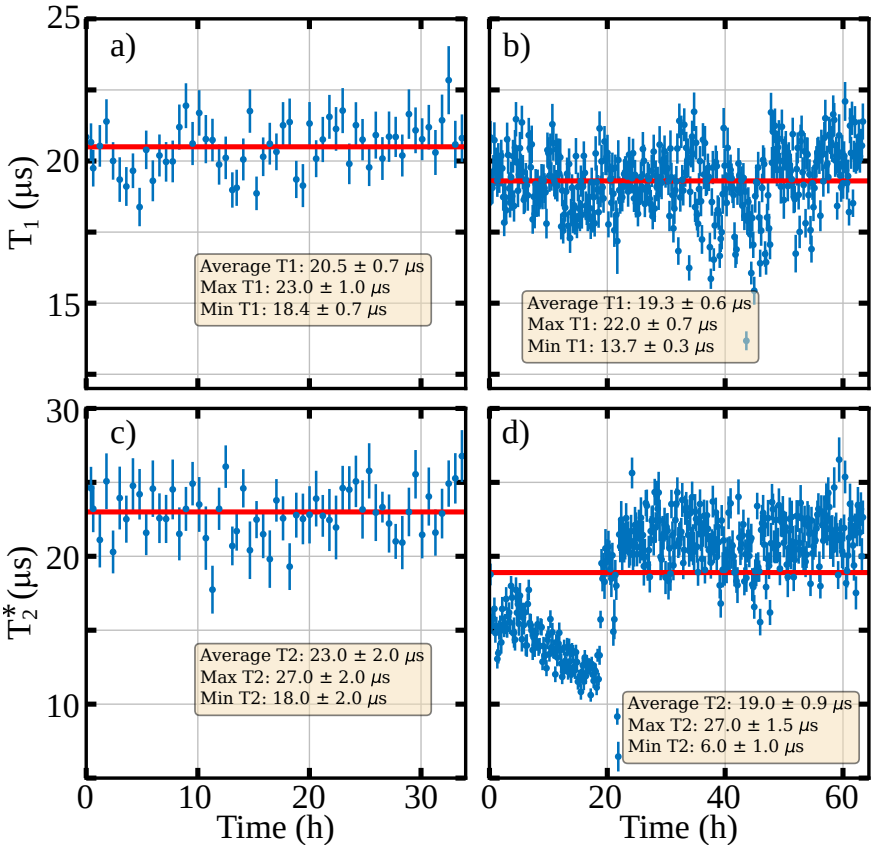

Figure A.1: **a)** T_1 measurement over a time span of 33 hours, during the weekend. **b)** T_1 measurement over a time span of 63 hours, during the week. **c)** T_2^* measured with a Ramsey experiment at the same time as plot a. **d)** T_2^* measured at the same time as plot b. The red line in each plot is the average value of all the measurements in the same plot.

for T_1 and T_2^* are respectively shown in fig.A.1a and c. And then for over 60 hours during the week, shown in fig.A.1b and d.

Unfortunately the output coupling between the cavity and the environment was relatively strong and as a consequence the qubit in the experiment was Purcell limited at around 25 μs. The T_1 measurements results are quite constant overtime around this value. The measurment of T_2^* instead has shown a worsening during the week that lasted around 20 hours. Most likely something in the surroundings influenced the cryostat or instrumental ground. Successively, some improvement in the grounding has been made in the laboratory. In particular the cryostat ground has been isolated as it was discovered that the temperature controller ground was connected to the cryostat ground. Also

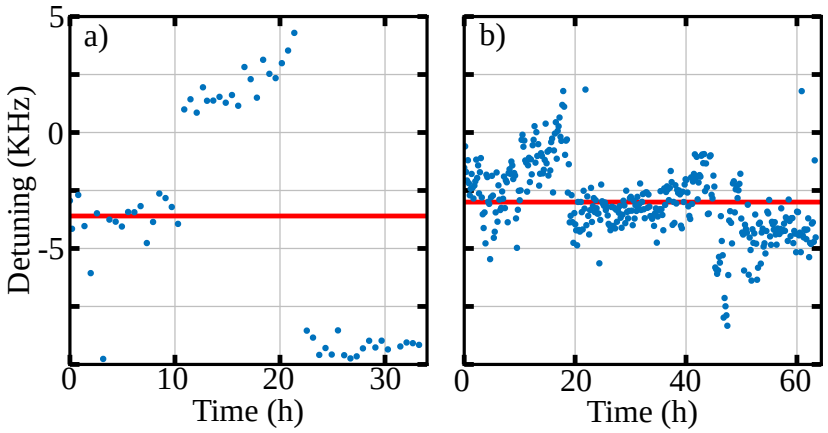

Figure A.2: **a)** Detuning between the qubit frequency and the drive frequency, extracted from the T_2^* measurement shown in plot A.1c. **b)** Detuning extracted from the T_2^* measurement shown in plot A.1d.

all the instruments connected to the same cryostat have been set to the same ground, different from the cryostat one. Unfortunately, another T_1 and T_2^* monitoring like the one presented has not been performed after the improvements. But several experiments, including the hose experiment presented in chapter 5 have shown good stability over time.

From the Ramsey experiment it is also possible to extract the effective oscillation period and compare it to the ideal one. In this way one can get the frequency difference between the qubit and the drive. This difference is shown in fig.A.2 respectively for the 30 hours measurement and the 60 hours one. The frequency detuning is stable in the range of a few KHz, with a non-zero average value due to a mistake in the initial drive frequency setting.

Appendix B

Eccosorb fabrication

The conventional coaxial filters I used in the experiments have a working range up to around 20 GHz. At higher frequencies the attenuation starts to decrease and the radiation can pass through without a noise attenuation sufficient for the experiments. In order to filter high frequency noise, like infrared, I fabricated custom coaxial filters based on an absorbing material, named Eccosorb. Absorbing materials are typically characterized by an irregular density, due to the presence of dense grains. E.m. waves with wavelengths shorter than the grains will scatter inside the material and their power will be dissipated.

The properties of this material[1] are shown in fig. B.1. The K' value is equivalent to the dielectric constant of the material, that changes as a function of the frequency. This value is averaged in the working range of [3 - 10]GHz and it is then used to evaluate the filter impedance as a function of the ratio between the external and internal cylinder diameters. The inner conductor

E-M PROPERTIES OF ECCOSORB MF													
		Frequency Hz							Frequency GHz				
		10^2	10^3	10^4	10^5	10^6	10^7	10^8	1,0	3,0	8,6	10,0	18,0
MF-110	K'	18	16	15	13	11	9,0	7,0	5,0	3,2	3,0	2,9	2,8
	Tan D	0,01	0,01	0,02	0,02	0,03	0,03	0,04	0,04	0,05	0,05	0,04	0,04
	K''	0,18	0,16	0,30	0,26	0,33	0,27	0,28	0,20	0,16	0,15	0,12	0,11
	M'	1,2	1,2	1,2	1,2	1,2	1,2	1,1	1,1	1,1	1,0	1,0	1,0
	Tan M	0	0	0	0	0	0	0	0	0	0,10	0,10	0,20
	M''	0	0	0	0	0	0	0	0	0	0,10	0,10	0,20
	dB/cm	0	0	0	0	0	0	0,01	0,09	0,26	2,0	2,2	6,6
	$\lvert Z\rvert/Z_0$	0,26	0,27	0,28	0,30	0,33	0,37	0,40	0,47	0,59	0,59	0,59	0,60

Figure B.1: Eccosorb properties table. Relevant properties in the table are K', that corresponds to the relative dielectric constant of the material and dB/cm that corresponds to the attenuation per cm. The first value is used to evaluate the filter impedance, the second to estimate the attenuation of the desired frequencies.

[1] I used the CR-110 type, that is cast-able, whereas the MF-110 is mold-able. They have the same properties.

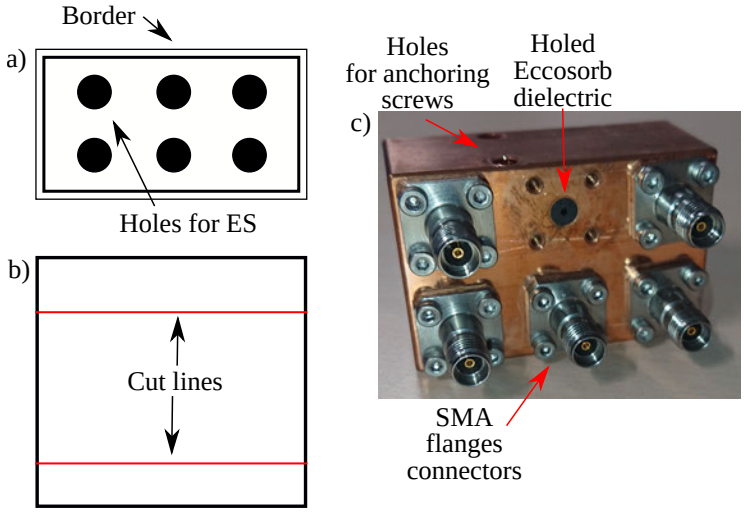

Figure B.2: **a)** Schematic, Top view. Holes with the right diameter are drilled in the body, but the bottom is closed. A border is present on the top part to allow casting the absorber in the holes when it is in a fluid state. **b)** Schematic, side view. After the absorber is cured (hardened), the block is cut in the middle, removing the bottom and exposing the filters. The top part is also removed. **c)** After the cut, holes with the right diameter are drilled in the absorber. The inner conductor is inserted in this last hole and it is terminated with SMA flange connectors on both sides. Some space between the filters is used to drill holes for screws, used to connect the filter pack to the cryostat base.

of the filter is a copper wire with a diameter of 1 mm. In order to obtain an impedance Z = 50 Ω with a dielectric constant of around 3.03, the external conductor diameter must be 4.27 mm. This value can be obtained by reverting the formula [59]:

$$Z = \frac{1}{2\pi\sqrt{\epsilon_r}}\sqrt{\frac{\mu_0}{\epsilon_0}}\log\left(\frac{D}{d}\right) \approx \frac{138.1\log_{10}\left(\frac{D}{d}\right)}{\sqrt{\epsilon_r}} \tag{B.1}$$

where D is the outer cylinder diameter and d is the inner one.

The dB/cm value in the table B.1 instead shows how much the filter will attenuate as a function of the frequency and of the filter length. A 2 cm filter will attenuate 4 dB at 8 GHz and 13 dB at 18 GHz. Unfortunately, the frequency range in the table is not very useful to understand how much the filter will attenuate at very high frequencies (i.e. >100 GHz).

I decided to build a 2x3 filter-pack made out of copper. The copper block schematic is shown in fig. B.2. Holes with a 4.27 mm are drilled from the top

of the block, leaving the bottom closed. The Eccosorb material is constituted of two components, material and hardener, that must be mixed together according to the instructions. At the end of this mixing procedure the material will be fluid. On the top of the copper block, a 5 mm high border (as shown in fig. B.2a) is placed on the perimeter to avoid spilling the material, that is cast in the holes until they are filled. The block is then placed under vacuum for a few seconds with the aim of removing big air bubbles that could be stuck in the material after the casting procedure. This procedure is repeated a few times

The body is left to cure on a hot plate overnight, after which the Eccosorb material will be solid. The copper body is then cut at the ends, as shown in fig. B.2b, exposing the bottom part of the filters, covered before by the copper. Also the top part is cut, to remove the border and the material spilled outside the holes. The total filter length after the cut is 2 cm.

When the material finally hardened, it is possible to drill a hole into it. So a hole of 1.1 mm is made in the cured Eccosorb center. The additional 0.1 mm is necessary to insert the inner 1 mm copper wire in the hole. The extremities of the wire are cut and the tip is shaped as a cone. The filter is finalized by adding SMA flanges to the extremities. These flanges have two clamps with an opening of 0.95 mm, such that the inner conductor can be fixed tightly in the SMA connector. The final result is shown in fig.B.2c.

The filter have been tested at room temperature with a VNA, the results are presented in fig. B.3. The reflected power below 20 dB (top row in the picture) is an indication of a good 50 Ω impedance match up to 20 GHz. The transmission (fig. B.3c) behaves as expected following the table B.1 for a 2 cm long filter. I attempted to fit the insertion loss with a second order polynomial. The fit is shown in the last plot, as a red line. If the filter behavior would effectively be a second order polynomial, the filter attenuation would be larger than 100 dB for frequencies higher than 100 GHz.

The new versions of the filter packs have T-shaped SMA flanges, that allow a reduction of the volume. Also Aluminium has been tested as an alternative to copper. Copper offers a better thermalization than aluminium, but it is also heavier. So a block made out of aluminium can be used to avoid mechanical stress to the cryostat.

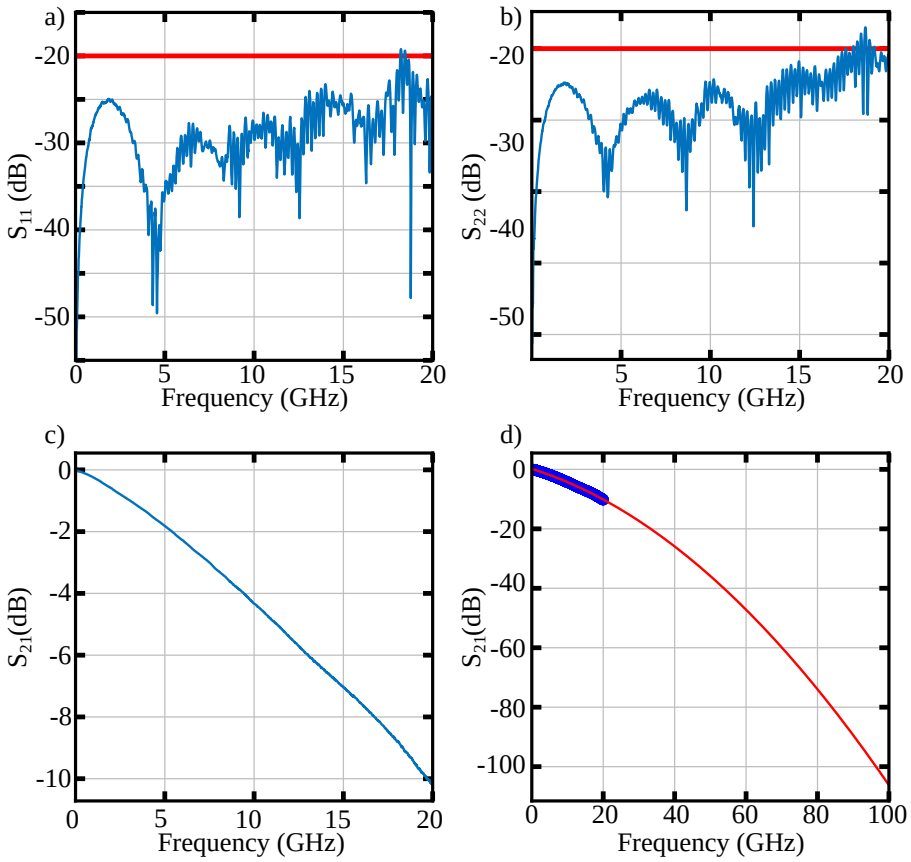

Figure B.3: Eccosorb filters S-parameters. **a)** Reflected power from one of the two sides of the filter. **b)** Reflected power from the other side of the filter. Having a reflection below -20 dB means that a good impedance match has been achieved. **c)** Transmission through the filter. The insertion loss at 18 GHz is compatible with the table for a 2 cm long filter. **d)** Polinomial fit to the data in **c)**, if the behavior of the filter is assumed polynomial, the attenuation at high frequencies would be over 100 dB.

Appendix C

First hose version: mistakes and improvements.

In this chapter I am going to talk about the first version of the experiment that has been shown in this thesis.

The first version of the system can be seen in fig. C.1, where two qubits are placed on different sapphires chips. The chips are separated by a distance of 3 mm along the y-direction. They are inserted in two separated slits placed on the bottom of the cavity. The chips are held in place by screws, inserted in screw holes placed in the cavity seam, as shown at the top of the picture.

The hose has roughly the same diameter as of the second version, but it has only 3 layers of μ-metal and 3 of aluminium. The outer shell is not made out of the same block of aluminium as the cavity. In a first experiment the slit between the hose outer shell and the cavity was not closed and it resulted in a cavity Q_{int} of around $30 \cdot 10^3$. Successively the slit has been closed with indium, improving the quality factor to raound $300 \cdot 10^3$.

The design of the aSQUID qubit is shown in fig. C.1c, with a SQUID loop of 200x200 μm^2 and closed by the pads. This very large SQUID area has been used because of the expected low field at the center qubit. The simulation performed on this first hose and coil version suggested a magnetic field at the central qubit of around 0.35 nT when a current of 1 mA excites the coil.

The cryostat input line used for the coil excitation has a similar setup compared to the second version, but the commercial low pass filter used has a resistance of a few Ohms. As in chapter 6.3, the DC flux map is measured and it is shown in fig.C.2. The 3 V supplied by the AWG are sufficient to tune the qubit frequency for only half quantum flux. Exciting the coil with more power was causing overheating at the cryostat second plate, where 20 dB of attenuation are used and also at the base, because of the resistance of the LPF filter. The red dots in the plots correspond to the central qubit frequency,

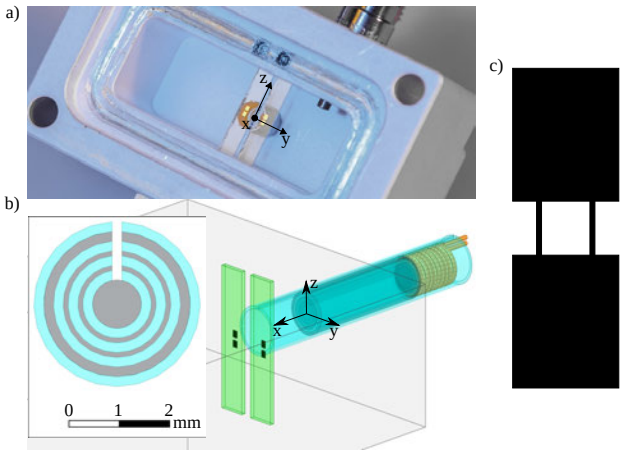

Figure C.1: **a)** First version of the system. Two sapphires pieces are inserted in the cavity, with 3 mm distance between each other along the y-direction. The qubits are inserted through two slits on the bottom of the cavity and held in place with screws. **b** The hose has a diameter of 2.5 mm and it has 5 alternating layers of ferromagnet and aluminium. The outer aluminium shell is separated by the cavity in this first hose version. The coil is solenoidal, with 10 windings, a diameter of 3 mm and a length of 4 mm, resulting in a self inductance of 126 nH in free space. **c)** Design used for the qubit. The pads dimensions are 500x400 μm^2, separated by a distance of 200 μm. The distance between the two junction is also 200 μm.

while the green one to the side qubit. A 20 % cross-talk between the qubit frequencies is observed.

The red and green lines in the figure are fit to the data. The calibration factor suggests that the field at the central qubit is on the order of 3.88 nT when the coil is excited with 1 mA of current. This shows that there is a factor of 10 of discrepancy with the simulation, just as explained for the second version of the experiment.

Comparing the simulations results of both versions, one can notice that the field improvement at the central qubit is equal to $\frac{22.4}{0.35} = 64$. Thanks to this improvement, the SQUID loop in the second version has been reduced by a factor of 16. So in the end, assuming the simulations have only an offset, an improvement of a factor of 4 in the qubit frequency tunability range is expected for the second version. Indeed, the qubit flux map presented in chapter 6.3 shows a period close to $2\,\Phi_0$ as expected. The maximum tunability range I measured in similar test experiments has been $2.3\,\Phi_0$.

A fast flux measurement has been done with the fist version of the hose and coil. The results are shown in fig.C.3. The pulses sequence and the flux

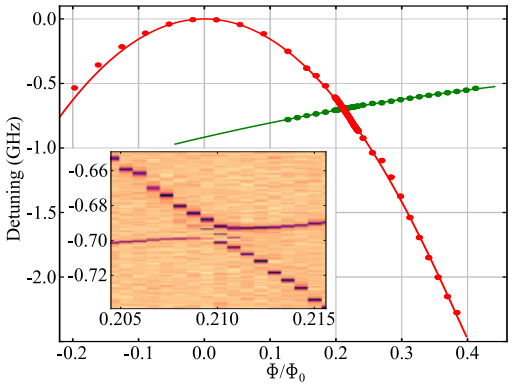

Figure C.2: Qubits flux map. The x-axis has been centered in the high sweet spot of the central qubit. The y-axis shows the detuning from the high sweet spot frequency (around 6.5 GHz). The central qubit tunability is less than one full period for the AWG voltage range of $3\,V_{PP}$. The inset shows the avoided crossing between the qubits, resulting in a coupling factor $J \approx 5$ MHz.

pulse shapes are the same as the second versions, as shown on top of the figure. The frequency jump is around 750 MHz for a square shaped flux pulse (fig.C.3b). For the experiment with the compensated flux pulse a shorter frequency range must be used since a portion of the AWG voltage range must be used to overshoot the flux. The compensated pulse system response is shown in fig.C.3c.

The result is slightly asymmetric, but the right slope is faster than 15 ns. Probably, due to the relatively small frequency change, a second exponential component is not showing in the frequency change.

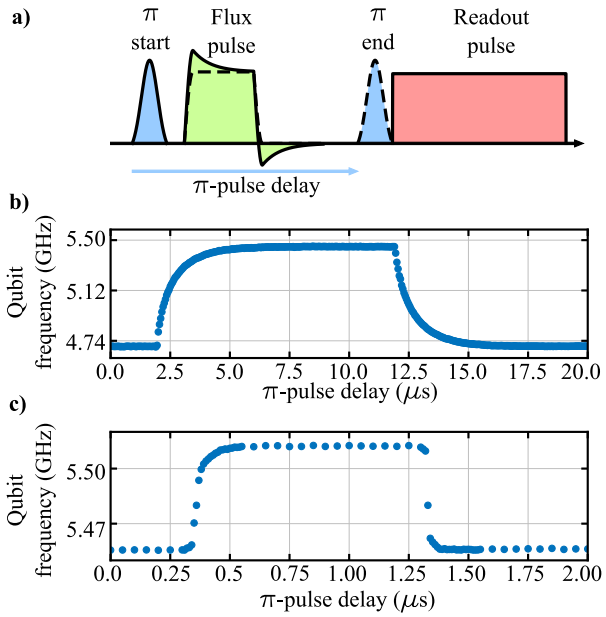

Figure C.3: **a)** Pulse sequence used for the measurement. This sequence is identical to the one presented in chapter 6.10. **b)** System response to the pulse sequence a), when a squared flux pulse is applied to the coil. **c)** System response to the pulse sequence a), when a compensated flux pulse with an amplitude overshoot is applied to the coil.

Bibliography

[1] Iulia Buluta and Franco Nori. Quantum simulators. *Science*, 326(5949), 2009.

[2] I. M. Georgescu, S. Ashhab, and Franco Nori. Quantum simulation. *Rev. Mod. Phys.*, 86:153, 2014.

[3] Raimond J.M. Haroche S. *Explore the Quantum*. Oxford University Press, 2006.

[4] Claudine Lacroix, Philippe Mendels, and Frédéric Mila. *Introduction to Frustrated Magnetism: Materials, Experiments, Theory*. Springer Science & Business Media, 2011.

[5] M. Dalmonte, et al. Realizing dipolar spin models with arrays of superconducting qubits. *Physical Review B*, 92(17), 2015.

[6] P. Jurcevic, et al. Quasiparticle engineering and entanglement propagation in a quantum many-body system. *Nature*, 511(7508):202, 2014.

[7] Philip Richerme, et al. Non-local propagation of correlations in quantum systems with long-range interactions. *Nature*, 511(7508):198, 2014.

[8] Jonathan Simon, et al. Quantum simulation of antiferromagnetic spin chains in an optical lattice. *Nature*, 472(7343):307, 2011.

[9] Alexander O. Gogolin, Alexander A. Nersesyan, and Alexei M. Tsvelik. *Bosonization and Strongly Correlated Systems*. Cambridge University Press, 2004.

[10] Andrew A. Houck, Hakan E. Türeci, and Jens Koch. On-chip quantum simulation with superconducting circuits. *Nature Physics*, 8(4), 2012.

[11] Jens Koch, et al. Charge-insensitive qubit design derived from the Cooper pair box. *Physical Review A*, 76(4):042319, 2007.

[12] Hanhee Paik, et al. Observation of High Coherence in Josephson Junction Qubits Measured in a Three-Dimensional Circuit QED Architecture. *Physical Review Letters*, 107(24):240501, 2011.

[13] J.D. Jackson. *Classical Electrodynamics, 3rd Ed.* Wiley India Pvt. Limited, 2007.

[14] M. Tinkham. *Introduction to superconductivity.* Mc Graw Hill, 1996.

[15] C. Navau, et al. Long-distance transfer and routing of static magnetic fields. *Physical Review Letters*, 112(25):253901, 2014.

[16] Richard P. Feynman. Simulating physics with computers. *International Journal of Theoretical Physics*, 21(6):467, 1982.

[17] S. Blundell. *Magnetism in Condensed Matter.* Oxford Master Series in Condensed Matter Physics. Oxford press, 2001.

[18] Chanchal K. Majumdar and Dipan K. Ghosh. On Next-Nearest-Neighbor Interaction in Linear Chain. I. *Journal of Mathematical Physics*, 10(8):1388, 1969.

[19] Hans A Bethe. *Selected Works of Hans A Bethe: (With Commentary)*, volume 18. WORLD SCIENTIFIC, 1997.

[20] Thierry Giamarchi. *Quantum Physics in One Dimension.* Clarendon Press, 2004.

[21] Tapan Mishra, et al. Quantum phases and phase transitions of frustrated hard-core bosons on a triangular ladder. *Physical Review B*, 87(17):174504, 2013.

[22] Philip Richerme, et al. Non-local propagation of correlations in quantum systems with long-range interactions. *Nature*, 511:198, 2014.

[23] Leon Balents. Spin liquids in frustrated magnets. *Nature*, 464(7286):199, 2010.

[24] Jonathan Simon, et al. Quantum simulation of antiferromagnetic spin chains in an optical lattice. *Nature*, 472(7343), 2011.

[25] Steven R. White. Density-matrix algorithms for quantum renormalization groups. *Physical Review B*, 48(14):10345, 1993.

[26] D. Zoepfl, et al. Characterization of low loss microstrip resonators as a building block for circuit QED in a 3D waveguide. *AIP Advances*, 7(8):085118, 2017.

[27] Deanna M. Abrams, et al. Methods for Measuring Magnetic Flux Crosstalk between Tunable Transmons. *Physical Review Applied*, 12(6):064022, 2019.

[28] P. Krantz, et al. A quantum engineer's guide to superconducting qubits. *Applied Physics Reviews*, 6(2):021318, 2019.

[29] Grègoire Ithier. *Manipulation, readout and analysis of the decoherence ofa superconducting quantum bit*. Ph.D. thesis, Université Pierre et Marie Curie - Paris VI, https://tel.archives-ouvertes.fr/tel-00130589/document, 2005.

[30] Uri Vool and Michel H. Devoret. Introduction to quantum electromagnetic circuits. 45(7):897, 2017.

[31] David M. Pozar. *Microwave engineering*. Wiley, 2011.

[32] Agustin Palacios-Laloy. *Superconducting qubit in a resonator: test of the Legget-Garg inequality andsingle-shot readout*. Ph.D. thesis, Université Pierre et Marie Curie - Paris VI, https://tel.archives-ouvertes.fr/tel-00815078/document, 2010.

[33] V. V. Schmidt. *The physics of superconductors*. Springer, 1997.

[34] Eyob A. Sete, Jay M. Gambetta, and Alexander N. Korotkov. Purcell effect with microwave drive: Suppression of qubit relaxation rate. *Physical Review B*, 89(10):104516, 2014.

[35] Eyob A. Sete, John M. Martinis, and Alexander N. Korotkov. Quantum theory of a bandpass purcell filter for qubit readout. *Phys. Rev. A*, 92, 2015.

[36] Z. Wang, et al. Cavity attenuators for superconducting qubits. *Phys. Rev. Applied*, 11:10, 2019.

[37] Lev S. Bishop, Eran Ginossar, and S. M. Girvin. Response of the Strongly Driven Jaynes-Cummings Oscillator. *Physical Review Letters*, 105(10):100505, 2010.

[38] Matthew David Reed. *Entanglement and Quantum Error Correction with Superconducting Qubits*. Ph.D. thesis, Yale University, https://rsl.yale.edu/sites/default/files/files/RSL_Theses/reed.pdf, 2013.

[39] M. Stammeier, S. Garcia, and A. Wallraff. Applying electric and magnetic field bias in a 3D superconducting waveguide cavity with high quality factor. *Quantum Science and Technology*, 3(4):045007, 2018.

[40] Yarema Reshitnyk, Markus Jerger, and Arkady Fedorov. 3D microwave cavity with magnetic flux control and enhanced quality factor. *EPJ Quantum Technology*, 3(1):1, 2016.

[41] Wei-Cheng Kong, et al. Introduction of DC line structures into a superconducting microwave 3D cavity. *Review of Scientific Instruments*, 86(2):023108, 2015.

[42] J. B. Pendry, D. Schurig, and D. R. Smith. Controlling electromagnetic fields. *Science*, 312(5781):1780, 2006.

[43] Simon E. Nigg, et al. Black-box superconducting circuit quantization. *Physical Review Letters*, 108(24):240502, 2012.

[44] Florent Lecocq, et al. Junction fabrication by shadow evaporation without a suspended bridge. *Nanotechnology*, 22(31):315302, 2011.

[45] A. Potts, et al. Cmos compatible fabrication methods for submicron josephson junction qubits. *IEE Proceedings - Science, Measurement and Technology*, 148(5):225, 2001.

[46] Yukihiro Ota. Ambegaokar-Baratoff relations for Josephson critical current in heterojunctions with multigap superconductors. *Physical Review B*, 81(21), 2010.

[47] S. Probst, et al. Efficient and robust analysis of complex scattering data under noise in microwave resonators. *Review of Scientific Instruments*, 86:024706, 2015.

[48] Loudon R. *Quantum theory of light*. Oxford science publications, 2000.

[49] Deanna M. Abrams, et al. Methods for measuring magnetic flux crosstalk between tunable transmons. *Physical Review Applied*, 12(6):064022, 2019.

[50] Yu Chen, et al. Qubit Architecture with High Coherence and Fast Tunable Coupling. *Physical Review Letters*, 113(22):220502, 2014.

[51] F. Yoshihara, et al. Decoherence of Flux Qubits due to 1/f Flux Noise. *Physical Review Letters*, 97(16):167001, 2006.

[52] Jonas Bylander, et al. Noise spectroscopy through dynamical decoupling with a superconducting flux qubit. *Nature Physics*, 7(7):565, 2011.

[53] N. K. Langford, et al. Experimentally simulating the dynamics of quantum light and matter at deep-strong coupling. *Nature Communications*, 8(1):1, 2017.

[54] O. Gargiulo, et al. Fast flux control of 3D transmon qubits using a magnetic hose. *Applied Physics Letters*, 118(1):012601, 2021.

[55] J. Rahamim, et al. Double-sided coaxial circuit QED with out-of-plane wiring. *Applied Physics Letters*, 110(22):222602, 2017.

[56] C. Axline, et al. An architecture for integrating planar and 3D cQED devices. *Applied Physics Letters*, 109(4):042601, 2016.

[57] J. Y. Mutus, et al. Design and characterization of a lumped element single-ended superconducting microwave parametric amplifier with on-chip flux bias line. *Applied Physics Letters*, 103(12):122602, 2013.

[58] J. Y. Mutus, et al. Strong environmental coupling in a Josephson parametric amplifier. *Applied Physics Letters*, 104(26):263513, 2014.

[59] F.E. Terman. *Radio engineers handbook*. McGraw-Hill, 1945.